Study of Arborescent Poly(L-Glutamic Acid) by Pyrene Excimer Formation

by

Timothy Hall

A thesis
presented to the University of Waterloo
in fulfillment of the
thesis requirement for the degree of
Master of Science
in
Chemistry

Waterloo, Ontario, Canada, 2012

I hereby declare that I am the sole author of this thesis. This is a true copy of the thesis, including any required final revisions, as accepted by my examiners.

I understand that my thesis may be made electronically available to the public.

Abstract

The biological function of a protein is determined by its amino acid sequence, structure, and internal dynamics. In turn the prediction of a protein structure from its folding pathway involves the characterization of the dynamics of the polypeptide backbone. This study addresses how the internal dynamics of arborescent polypeptides are affected by increased crowding of the interior of these branched polymer molecules.

Linear, comb-branched, and arborescent poly(L-glutamic acid) (PGA) samples were analyzed by ^{1}H NMR spectroscopy to determine their chain conformation. The PGA chains of these constructs were shown to adopt α-helical and random coil conformations in *N*,*N*-dimethylformamide (DMF) and in dimethyl sulfoxide (DMSO), respectively. The hydrodynamic diameter (D_h) of the arborescent PGAs, determined using dynamic light scattering measurements, increased with increasing generation number and when the side-chains adopted random coil instead of α-helical conformations.

The PGA samples were labelled with 1-pyrenemethylamine to determine how their structure affected the internal dynamics of the arborescent polymers in solution, from the analysis of their fluorescence spectra and decays. For each pyrene-labelled polymeric construct excimer formation increased with increasing pyrene content, and the efficiency of excimer formation increased with the generation number due to the increased density of the macromolecules. Comparison of the time-resolved fluorescence results acquired in DMF and in DMSO demonstrated that the helical conformation led to slower chain dynamics in DMF and that despite the higher viscosity of DMSO, the polypeptide side-chains were more mobile as a consequence of the random coil conformation of the linear PGA segments. These results suggest that the formation of structural motives inside a polypeptide slows down its internal dynamics.

Acknowledgements

I would like to thank my supervisors, Professor Mario Gauthier and Professor Jean Duhamel, along with the members of my committee, Prof. Thorsten Dieckmann, and Prof. Michael K.C. Tam for their help and allowing me to develop my own ideas. I am grateful to the $(GWC)^2$ and the University of Waterloo's Faculty of Science for accepting me as a graduate student and for their financial support. In addition, I am grateful for the financial support of NSERC for this project. I am indebted to Greg Whitton for supplying me with the arborescent polypeptide samples and for the guidance that he provided. I would like to thank all of the graduate students with whom I have shared many joyful events. Lastly, I would like to thank everybody in my personal life for their support and motivation.

Table of Contents

Author`s Declaration ii
Abstract iii
Acknowledgements iv
Table of Contents v
List of Figures vii
List of Tables xi
List of Schemes xv
List of Abbreviations and Symbols xvi
1. Introduction 1
1.1. Protein Folding 1
1.2. Arborescent Polymers 2
1.3. Pyrene Fluorescence Studies of Polymers 3
1.4. Research Objectives 5
1.5. Outline of the Thesis 6
2. Characterization of Poly(L–glutamic acid) 7
2.1. Introduction 7
2.2. Background Information 8
2.2.1. Dendrimers and Arborescent Structures 8
2.2.2. Synthesis 9
2.2.3. Polymer Conformation 11
2.2.4. Hydrodynamic Size 11
2.3. Experimental Procedures 14
2.4. Results and Discussion 18
2.4.1. Nuclear Magnetic Resonance Spectroscopy 18
2.4.2. Dynamic Light Scattering 22
2.5. Conclusions 27
3. Fluorescence 28
3.1. Introduction 28
3.2. Background Information 28

3.2.1. Fluorescence 28
3.2.2. Fluorescence Emission 30
3.2.3. Excimer Formation 32
3.2.1. Birks' Scheme 33
3.3. Experimental Procedures 35
3.4. Results and Discussion 37
3.5. Conclusions 40
4. Internal Dynamics of Arborescent PGA Probed by Excimer Formation 42
4.1. Introduction 42
4.2. Experimental Procedures 43
4.2.1. Synthesis 43
4.2.2. Instruments 46
4.3. Analysis Methods 46
4.3.1. Absorption Spectroscopy 46
4.3.2. Emission Spectroscopy 47
4.3.3. Fluorescence Blob Model 49
4.4. Results and Discussion 57
4.4.1. Pyrene-labelled Poly(L-glutamic acid) 57
4.4.2. Steady State Fluorescence 60
4.4.3. Time-resolved Fluorescence 64
4.4.4. Fluorescence Blob Model Results 67
4.5. Conclusions 75
5. Conclusions and Suggestions for Future Work 77
5.1. Conclusions 77
5.2. Future Work 78
References 80
Appendix A: Nuclear Magnetic Resonance Spectroscopy Results 86
Appendix B: Dynamic Light Scattering Results 88
Appendix C: Birks' Scheme Parameters 93
Appendix D: Gel Permeation Chromatography Traces 94
Appendix E: Fluorescence Blob Model Parameters 99

Appendix F: Sum of Exponentials Analysis Parameters 111

List of Figures

Figure 2.1: NMR spectra (500 MHz, in DMSO-d6) for G2 arborescent poly(γ–benzyl L–glutamate) (top), and G2 poly(L-glutamic acid) (bottom). 18
Figure 2.2: NMR spectra (300 MHz) for G1 arborescent PGA in D_2O/H_2O at pH 8 (top), and with HCl added, pH 5 (bottom). 20
Figure 2.3: NMR spectra for G1 arborescent PGA in DMSO-d6 (top), and DMF-d7 (bottom). 21
Figure 2.4: NMR spectra for the G3 (left) and G2 (right) arborescent PGA samples in DMF-d7 corresponding to the α-proton signal. 22
Figure 2.5: Distribution functions for the time decay rate of scattered light intensity by G3 PGA in DMSO, measured at 150^o, 135^o, 120^o, 105^o, 90^o, 75^o, and 60^o (top to bottom). 23
Figure 2.6: The q^2 dependence of the relaxation rate of scattered light intensity for the diffusion coefficients of G3 PGA in DMSO. 24

Figure 3.1: Jablonski diagram depicting the energy changes associated with absorption, internal conversion, and fluorescence. 29
Figure 3.2: Chemical structures of pyrene, 1-pyrenemethylamine, and 1-pyrenemethylacetamide (left to right). 30
Figure 3.3: Steady-state fluorescence spectrum for 1-pyrenemethylacetamide in DMF (11 mM). λ_{ex}= 344 nm. 31
Figure 3.4: Steady-state fluorescence spectra for 1-pyrenemethylacetamide in DMF (left) and in DMSO (right). The concentrations are 13, 11, 9, 7, and 5 mM from top to bottom; λ_{ex}= 344 nm. 38
Figure 3.5: Excimer formation in concentrated solutions of 1-pyrenemethylacetamide in DMF (◆) and DMSO (□). 38
Figure 3.6: Rate constant for excimer formation, retrieved from Birks' Scheme analysis of 1-pyrenemethylacetamide solutions in DMF (◆) and in DMSO (□). 40

Figure 4.1: UV-Vis absorption spectrum for 6.6-G3 arborescent PGA in DMF, with P_A= 2.61 47

Figure 4.2: Time-resolved fluorescence decays for 6.6-G3 arborescent PGA in DMF [*Py*] = 2.5 × 10^{-6} M. Monomer emission (left; λ_{ex}= 344 nm, λ_{em}= 375 nm, time per channel = 2.04 ns, χ^2=1.07). Excimer emission (right; λ_{ex}= 344 nm, λ_{em}= 510 nm, time per channel = 1.02 ns, χ^2=1.10). 48

Figure 4.3: Monomer (λ_{em}= 375 nm, left) and excimer (λ_{em}= 510 nm, right) decays for 6.6-G3 arborescent PGA in DMF analyzed by the Fluorescence Blob Model; χ^2=1.14, λ_{ex} = 344 nm, [*Py*]= 2.5 × 10^{-6} M. 55

Figure 4.4: GPC traces monitored with a fluorescence detector (λ_{ex}= 344 nm, λ_{em}= 375 nm). From top to bottom: pure 15% Py-Lin PGA, [*Py*] = 2.5 × 10^{-6} M; 11.7% Py-Lin PGA with impurities, [*Py*] = 2.5 × 10^{-6} M; and 1-pyrenemethylamine [*Py*] = 5.0 × 10^{-7} M. 60

Figure 4.5: Steady-state fluorescence spectra for Py-G3 arborescent PGA in DMF (left) and in DMSO (right). The pyrene contents are 12.6, 11.4, 10.9, 9.4, 8.1, 6.6, 5.4, and 4.0 mol % (top to bottom). 61

Figure 4.6: Plots of $\eta \times \tau_M^{-1} \times I_E/I_M$ versus pyrene content for linear (◆,◇), Py-G0 (■,□), Py-G1 (▲,△), Py-G2 (●,○), and Py-G3 (✕,) PGA constructs in DMF (filled symbols) and DMSO (hollow symbols). 63

Figure 4.7: Time-resolved fluorescence decays for the pyrene monomer (left, λ_{em}= 375 nm) and excimer (right, λ_{em}= 510 nm) for Py-G3 arborescent PGA in DMF with pyrene contents of 2.5, 5.4, 9.4, and 11 mol% (top to bottom); λ_{ex}= 344 nm, [*Py*] = 2.5 ×10^{-6} M. Inset: Rise time for the samples with pyrene contents of 2.5 and 11 mol %. 65

Figure 4.8: Plot of $(\eta/\tau_M) \times [(\tau_M / <\tau>_N) - 1]$ as a function of pyrene content for Py-Lin PGA (diamonds) and Py-G3 PGA (circles) in DMF (filled) and in DMSO (hollow). 66

Figure 4.9: Plots of k_2 versus corrected pyrene content for Py-G0 (■,□), Py-G1 (▲,△), Py-G2 (●,○), and Py-G3 (✕,) arborescent PGA constructs in DMF (top) and in DMSO (bottom). 68

Figure 4.10: Plots of N_{blob} versus corrected pyrene content for Py-linear (◆,◇), Py-G0 (■,□), Py-G1 (▲,△), Py-G2 (●,○), and Py-G3 (✕,) PGA arborescent constructs in DMF (filled symbols) and in DMSO (hollow symbols). 70

Figure 4.11: Plots of $k_{blob} \times N_{blob} \times \eta$ versus corrected pyrene content for Py-linear (◆,◇), Py-G0 (■,□), Py-G1 (▲,△), Py-G2 (●,○), and Py-G3 (✕,) PGA arborescent constructs in DMF (filled symbols) and in DMSO (hollow symbols). 71

Figure 4.12: Plot of N_{blob} (left) and $k_{blob} \times N_{blob} \times \eta$ (right) versus the number of peripheral branches for linear and arborescent PGA constructs in DMF (filled symbols) and DMSO (hollow symbols). 72

Figure 4.13: Plot of the ratios $(k_{blob} \times N_{blob} \times \eta)^{DMSO} / (k_{blob} \times N_{blob} \times \eta)^{DMF}$ (◆) and $N_{blob}^{DMSO} / N_{blob}^{DMF}$ (◇) versus the number of peripheral branches for the linear and arborescent PGA constructs. 74

Figure A1: ^{1}H NMR (500 MHz) spectra for linear PGA in DMSO-d6 and for linear, G0, G1, G2, G3 PGA samples in DMF-d7 (top to bottom). 86

Figure A2: ^{1}H NMR (500 MHz) spectra for linear PGA in DMF-d7 and for linear, G0, G1, G2, G3 PGA samples in DMSO-d6 (top to bottom)..... 87

Figure B1: The q^2 dependence of the relaxation rate of scattered light intensity for the diffusion coefficient of G2 (○) and G1 (△) PGA in DMSO. 88

Figure B2: The q^2 dependence of the relaxation rate of scattered light intensity for the diffusion coefficient of G1 (▲), G2 (●), and G3 (✕) PGA in DMF. 88

Figure B3: Distribution functions for the time decay rate of scattered light intensity by G2 PGA in DMSO measured at 150°, 135°, 120°, 105°, 90°, 75°, and 60° (top to bottom). 89

Figure B4: Distribution functions for the time decay rate of scattered light intensity by G1 PGA in DMSO measured at 150°, 135°, 120°, 105°, 90°, 75°, and 60° (top to bottom). 89

Figure B5: Distribution functions for the time decay rate of scattered light intensity by G3 PGA in DMF measured at 150°, 135°, 120°, 105°, 90°, 75°, and 60° (top to bottom). 90

Figure B6: Distribution functions for the time decay rate of scattered light intensity by G2 PGA in DMF measured at 150°, 135°, 120°, 105°, 90°, 75°, and 60° (top to bottom). 90

Figure B7: Distribution functions for the time decay rate of scattered light intensity by G1 PGA in DMF measured at 150°, 135°, 120°, 105°, 90°, 75°, and 60° (top to bottom). 91

Figure B8: Hydrodynamic radius distributions for G1 PGA in DMF obtained by non-negative linear least squares analysis of the correlation functions measured at 60^{o} with signal weightings by intensity (top) and by the number of particles (bottom). 92

Figure D1: GPC traces monitored with a fluorescence detector (λ_{ex}= 344 nm, λ_{em}= 375 nm) for Py-Linear PGA with pyrene contents of 10, 8.1, 7.5, 6.6, 6.6, 5.0, 2.4 mol % and 1-pyrenemethylamine (top to bottom)..... 94

Figure D2: GPC traces monitored with a fluorescence detector (λ_{ex}= 344 nm, λ_{em}= 375 nm) for Py-G0 PGA with pyrene contents of 22, 17, 13, 11, 6.6, 4.1 mol % and 1-pyrenemethylamine (top to bottom). 95

Figure D3: GPC traces monitored with a fluorescence detector (λ_{ex}= 344 nm, λ_{em}= 375 nm) for Py-G1 PGA with pyrene contents of 17, 13, 12, 7.2, 5.9, 1.3 mol % and 1-pyrenemethylamine (top to bottom). 96

Figure D4: GPC traces monitored with a fluorescence detector (λ_{ex}= 344 nm, λ_{em}= 375 nm) for Py-G2 PGA with pyrene contents of 10, 8.7, 6.6, 4.3, 1.1 mol % and 1-pyrenemethylamine (top to bottom)..... 97

Figure D5: GPC traces monitored with a fluorescence detector (λ_{ex}= 344 nm, λ_{em}= 375 nm) for Py-G3 PGA with pyrene contents of 11, 9.4, 8.1, 6.6, 6, 5.4, 4, 2.5 mol % and 1-pyrenemethylamine (top to bottom)..... 98

List of Tables

Table 2.1: Hydrodynamic diameter of arborescent poly(γ–benzyl L–glutamate) in DMF and in DMSO with 0.05% LiCl.[41] 12

Table 2.2: Hydrodynamic diameter of isolated comb-branched and arborescent poly(L-glutamate) molecules in water.[51] 13

Table 2.3: Characteristics of arborescent PBG samples of successive generations.[41] 14

Table 2.4: Hydrodynamic diameter of arborescent PGA in DMF and in DMSO, with 0.05% LiBr added. 26

Table 4.1: Pyrene content, P_A, A_{E-} / A_{E+} and f_{agg} for Py-linear and Py-G0 poly(L-glutamic acid). 57

Table 4.2: Pyrene content, P_A, A_{E-} / A_{E+} and f_{agg} for Py-G1, Py-G2 and Py-G3 arborescent PGA. 58

Table C1: Parameters retrieved from Birks' scheme analysis of the monomer and excimer decays acquired at various concentrations of PyMeAA in DMF. 93

Table C2: Parameters retrieved from Birks' scheme analysis of the monomer and excimer decays acquired at various concentrations of PyMeAA in DMSO..... 93

Table E1: Parameters retrieved from FBM analysis of the monomer decays for Py-Linear PGA in DMF..... 99

Table E2: Parameters retrieved from FBM analysis of the excimer decays for Py-Linear PGA in DMF..... 99

Table E3: Fractions of the different pyrene species retrieved from FBM analysis of Py-Linear PGA in DMF..... 100

Table E4: Parameters retrieved from FBM analysis of the monomer decays for Py-Linear PGA in DMSO..... 100

Table E5: Parameters retrieved from FBM analysis of the excimer decays for Py-Linear PGA in DMSO..... 101

Table E6: Fractions of the different pyrene species retrieved from FBM analysis of Py-Linear PGA in DMSO. 101
Table E7: Parameters retrieved from FBM analysis of the monomer decays for Py-G0 PGA in DMF. 102
Table E8: Parameters retrieved from FBM analysis of the excimer decays for Py-G0 PGA in DMF. 102
Table E9: Fractions of the different pyrene species retrieved from FBM analysis of Py-G0 PGA in DMF. 102
Table E10: Parameters retrieved from FBM analysis of the monomer decays for Py-G0 PGA in DMSO. 103
Table E11: Parameters retrieved from FBM analysis of the excimer decays for Py-G0 PGA in DMSO. 103
Table E12: Fractions of the different pyrene species retrieved from FBM analysis of Py-G0 PGA in DMSO. 103
Table E13: Parameters retrieved from FBM analysis of the monomer decays for Py-G1 PGA in DMF. 104
Table E14: Parameters retrieved from FBM analysis of the excimer decays for Py-G1 PGA in DMF. 104
Table E15: Fractions of the different pyrene species retrieved from FBM analysis of Py-G1 PGA in DMF. 104
Table E16: Parameters retrieved from FBM analysis of the monomer decays for Py-G1 PGA in DMSO. 105
Table E17: Parameters retrieved from FBM analysis of the excimer decays for Py-G1 PGA in DMSO. 105
Table E18: Fractions of the different pyrene species retrieved from FBM analysis of Py-G1 PGA in DMSO. 105
Table E19: Parameters retrieved from FBM analysis of the monomer decays for Py-G2 PGA in DMF. 106
Table E20: Parameters retrieved from FBM analysis of the excimer decays for Py-G2 PGA in DMF. 106

Table E21: Fractions of the different pyrene species retrieved from FBM analysis of Py-G2 PGA in DMF. 106
Table E22: Parameters retrieved from FBM analysis of the monomer decays for Py-G2 PGA in DMSO. 107
Table E23: Parameters retrieved from FBM analysis of the excimer decays for Py-G2 PGA in DMSO. 107
Table E24: Fractions of the different pyrene species retrieved from FBM analysis of Py-G2 PGA in DMSO. 107
Table E25: Parameters retrieved from FBM analysis of the monomer decays for Py-G3 PGA in DMF. 108
Table E26: Parameters retrieved from FBM analysis of the excimer decays for Py-G3 PGA in DMF. 108
Table E27: Fractions of the different pyrene species retrieved from FBM analysis of Py-G3 PGA in DMF. 109
Table E28: Parameters retrieved from FBM analysis of the monomer decays for Py-G3 PGA in DMSO. 109
Table E29: Parameters retrieved from FBM analysis of the excimer decays for Py-G3 PGA in DMSO. 110
Table E30: Fractions of the different pyrene species retrieved from FBM analysis of Py-G3 PGA in DMSO. 110

Table F1: Parameters retrieved by fitting the monomer decays for Py-Linear PGA samples in DMF to a sum of exponentials equation. 111
Table F2: Parameters retrieved by fitting the excimer decays for Py-Linear PGA samples in DMF to a sum of exponentials equation. 111
Table F3: Parameters retrieved by fitting the monomer decays for Py-Linear PGA samples in DMSO to a sum of exponentials equation. 112
Table F4: Parameters retrieved by fitting the excimer decays for Py-Linear PGA samples in DMSO to a sum of exponentials equation. 112
Table F5: Parameters retrieved by fitting the monomer decays for Py-G0 PGA samples in DMF to a sum of exponentials equation. 113

Table F6: Parameters retrieved by fitting the excimer decays for Py-G0 PGA samples in DMF to a sum of exponentials equation. 113
Table F7: Parameters retrieved by fitting the monomer decays for Py-G0 PGA samples in DMSO to a sum of exponentials equation. 113
Table F8: Parameters retrieved by fitting the excimer decays for Py-G0 PGA samples in DMSO to a sum of exponentials equation. 114
Table F9: Parameters retrieved by fitting the monomer decays for Py-G1 PGA samples in DMF to a sum of exponentials equation. 114
Table F10: Parameters retrieved by fitting the excimer decays for Py-G1 PGA samples in DMF to a sum of exponentials equation. 114
Table F11: Parameters retrieved by fitting the monomer decays for Py-G1 PGA samples in DMSO to a sum of exponentials equation. 115
Table F12: Parameters retrieved by fitting the excimer decays for Py-G1 PGA samples in DMSO to a sum of exponentials equation. 115
Table F13: Parameters retrieved by fitting the monomer decays for Py-G2 PGA samples in DMF to a sum of exponentials equation. 115
Table F14: Parameters retrieved by fitting the excimer decays for Py-G2 PGA samples in DMF to a sum of exponentials equation. 116
Table F15: Parameters retrieved by fitting the monomer decays for Py-G2 PGA samples in DMSO to a sum of exponentials equation. 116
Table F16: Parameters retrieved by fitting the excimer decays for Py-G2 PGA samples in DMSO to a sum of exponentials equation. 116
Table F17: Parameters retrieved by fitting the monomer decays for Py-G3 PGA samples in DMF to a sum of exponentials equation. 117
Table F18: Parameters retrieved by fitting the excimer decays for Py-G3 PGA samples in DMF to a sum of exponentials equation. 117
Table F19: Parameters retrieved by fitting the monomer decays for Py-G3 PGA samples in DMSO to a sum of exponentials equation. 118
Table F20: Parameters retrieved by fitting the excimer decays for Py-G3 PGA samples in DMSO to a sum of exponentials equation. 118

List of Schemes

Scheme 1.1: Synthesis of arborescent polymers. 3

Scheme 1.2: Pyrene excimer formation..... 4

Scheme 2.1: Synthesis of a G0 arborescent PBG, with a comb-branched structure. G1–G3 arborescent structures are obtained by repetition of the partial acidolysis and grafting steps.[35] .. 10

Scheme 2.2: Acidolysis of poly(γ–benzyl L–glutamate) to produce the sodium salt form of poly(L–glutamic acid). 10

Scheme 3.1: Birks' scheme describing excimer formation for molecular pyrene. 34

Scheme 4.1: Labelling reaction of poly(L–glutamic acid) sodium salt with PMA. 43

Scheme 4.2: Photophysical pathways for the formation of excimer by pyrene labels randomly attached to a polymer. 50

List of Abbreviations and Symbols

A	Absorbance
A_{E-}/A_{E+}	Ratio of pre-exponential factors
D	Diffusion coefficient for particles in solution
D_h	Hydrodynamic diameter
DLS	Dynamic light scattering
DMF	*N*,*N*-Dimethylformamide
DMSO	Dimethyl sulfoxide
DP_n	Number-average degree of polymerization
D^*	Long-lived excimer species
$[E^*]$	Excimer concentration within a sample
$E0^*$	Short-lived excimer species
EDC	1-[3-(Dimethylamino)propyl]-3-ethylcarbodiimide hydrochloride
FBM	Fluorescence blob model
f_{agg}	Fraction of aggregated pyrene in a sample
f_{Mfree}	Fraction of pyrene in a sample that do not form excimer
$f(t)$	Rate constant for excimer formation
$g(t)$	Sum of exponentials equation
G0	Generation zero (comb-branched) polymer
G1	Generation one arborescent polymer
G2	Generation two arborescent polymer
G3	Generation three arborescent polymer
GPC	Gel permeation chromatography
I_E/I_M	Ratio of excimer intensity to monomer intensity
k_B	Boltzmann constant
k_{blob}	Rate constant for excimer formation inside a *blob*
k_e	Rate constant for the transfer of ground-state pyrene between blobs
k_1	Rate constant for excimer formation
k_{-1}	Rate constant for excimer dissociation
k_2	Rate constant for rapid excimer formation

M_n	Number-average molecular weight
M_n^{NMR}	Number-average molecular weight determined by NMR
N_{blob}	Number of polymer units contained in a blob
n_o	Refractive index
NMR	Nuclear magnetic resonance spectroscopy
P_A	Peak-to-valley absorbance ratio
PBG	Poly(γ-benzyl L-glutamate)
PDI	Polydispersity index
PGA	Poly[L-glutamic acid]
PGNa	Poly[L-glutamic acid] sodium salt
PMA	1-Pyrenemethylamine
Py	Pyrene
Py*	Excited state pyrene
[*Py*]	Pyrene concentration within a sample
Py^*_{diff}	Excited state pyrene that forms excimer by diffusion
Py^*_{free}	Excited state pyrene that does not forms excimer
$Py^*_{k_2}$	Excited state pyrene that forms excimer by rapid rearrangement
$[Py]_{local}$	Pyrene labels on a polymer capable of forming excimer
PyMeAA	1-Pyrenemethylacetamide
p-value	Probability that two pyrene labels will form an excimer
q^2	Angle parameter
R_h	Hydrodynamic radius
T	Temperature
t	Time
TFA	Trifluoroacetic acid

UV-Vis	Ultraviolet and visible
WHMIS	Workplace hazardous material information system
x	Molar fraction of pyrene-labelled units in the polymer sample
χ^2	Describes the deviation between the measured and expected value
Γ	Relaxation rate of scattered light intensity
λ_{Py}	Pyrene concentration within a polymer in moles pyrene/gram polymer
λ_{em}	Emission wavelength of light
λ_{ex}	Excitation wavelength of light
η	Solvent viscosity
θ	Angle
τ	Correlation time for scattered light
τ_D	Lifetime of pyrene excimer species, long-lived
τ_{E0}	Lifetime of pyrene excimer species, short-lived
τ_M	Pyrene monomer lifetime without excimer formation
$<\tau>_N$	Number-average lifetime

1. Introduction

1.1. Protein Folding

Protein folding is the process whereby a polypeptide in a coiled conformation undergoes a series of conformational rearrangements to form a structured 3-dimensional molecular object referred to as a protein, whose activity is necessary for many biological processes. Protein folding studies fall into two main categories, depending on whether one attempts to characterize the chain dynamics or the structure of the polypeptide. While X-ray diffraction analysis is well-established to investigate the structure of proteins, the internal chain dynamics controlling how globular proteins fold from one state to another are the object of a large number of studies, as more research indicates that numerous degenerative diseases such as cystic fibrosis and Alzheimer's disease are associated with the unfolding or failure to fold of a protein.[1,2]

Protein folding was first examined on the basis that each residue of a polypeptide sequence can adopt a fixed set of conformations. When considering that a protein is constituted by a large number of repeating units that can all adopt a set number of conformations, the number of pathways by which a protein can fold from one conformation to another becomes staggering. Levinthal's paradox leads to the notion that folding occurs along a pathway that involves intermediate conformations aligned along an energy funnel. Some small proteins, such as chymotrypsin inhibitor 2, have been shown to alternate between folded and unfolded states via simple two-state kinetics.[3,4] For larger proteins such as hen lysozyme the folding pathway is more complex however, as they fold through a mechanism involving intermediate states.[5]

An important element in predicting how proteins fold involves the characterization of the internal dynamics of polypeptide chains. Simulations can be carried out to probe the nature of

internal dynamics. While theoretical, these results produce native protein conformations from completely denatured states that are in close agreement with data obtained by X-ray diffraction.[6] Nuclear magnetic resonance (NMR) spectroscopy is another method used to characterize the internal dynamics of proteins in solution. Protein samples with amino acid isotopomers are generated by overexpression in bacterial cells, and heteronuclei relaxation studies yield parameters that describe their side-chain dynamics.[7] The NMR analysis of protein mutants can identify the influence that specific residues have on the overall folding of the wild type protein.[8] Fluorescence techniques have also been instrumental in studying chain dynamics. For instance, fluorescence anisotropy can measure the rotational diffusion of fluorescent probes.[9] Stopped-flow fluorescence experiments have been used to induce changes in the conformation of proteins and determine the kinetics of protein folding, by monitoring changes in the emission spectrum of a fluorescent probe on the microsecond timescale.[10] Fluorescence dynamic quenching experiments conducted on a fluorescent probe attached to a macromolecule yields information on its internal dynamics, whether the macromolecule is flexible or rigid, present as a single unit or aggregated.[11] Together theses different techniques have been instrumental in providing comprehensive understanding of how some specific proteins fold.[12–14]

1.2. Arborescent Polymers

Arborescent polymers are a unique class of dendritic macromolecules derived from successive grafting reactions of linear side-chains onto a polymer substrate. Their generation-based synthesis is outlined in Scheme 1.1. These polymer constructs have numerous appealing properties which make them interesting candidates as additives to enhance the rheological properties of commercial polymers, or for the microencapsulation of therapeutic drugs.[15,16]

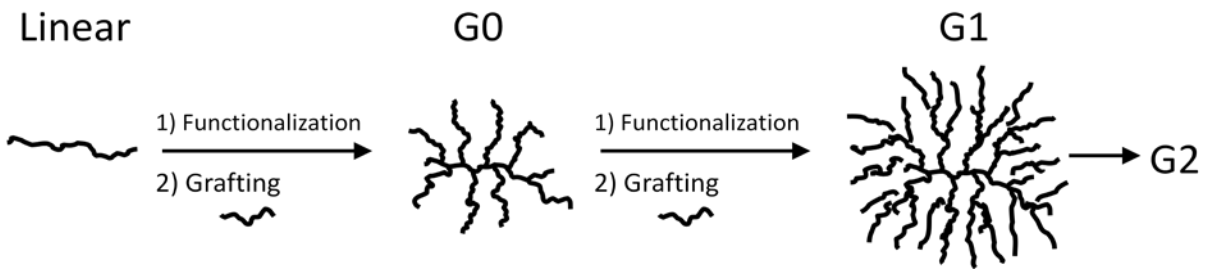

Scheme 1.1: Synthesis of arborescent polymers.

Arborescent polymers comprised of poly(L-glutamic acid) (PGA) side-chains, that can adopt an α-helical conformation under certain conditions, can be utilized as protein analogues since like proteins, they can contain a large number of α-helical structural motives concentrated within a small volume. In aqueous solutions PGA exists in its sodium glutamate form, a negatively charged polyelectrolyte adopting a random coil conformation. When the pH of the aqueous solution is lowered, however, the acidified PGA adopts an α-helical conformation. With further pH reduction, PGA eventually becomes insoluble in aqueous media due to unfavourable hydrophobic interactions.

Poly(γ-benzyl L-glutamate) (PBG) is a synthetic precursor to PGA that adopts a similar secondary structure. While PGA undergoes conformational changes in aqueous solution with pH variations, PBG has been shown to adopt α-helical and random coil conformations when dissolved in *N*,*N*-dimethylformamide (DMF) and in dimethyl sulfoxide (DMSO), respectively.[17]

1.3. Pyrene Fluorescence Studies of Polymers

Pyrene (Py) is a fluorescent label often used to characterize polymer chain dynamics in organic solvents.[18] Upon absorption of light (λ_{ex}) at 344 nm, an excited pyrene can either relax to the ground-state through fluorescence or form an excimer upon encounter with a ground-state

pyrene. The excimer emits light at longer wavelengths and with a natural lifetime that is, in the case of pyrene, shorter than for the monomer ($\tau_E < \tau_M$). The internal dynamics of macromolecules such as arborescent polymers can be investigated by observing the rate at which two pyrene chromophores, covalently attached to a polymer, encounter and form excimer as shown in Scheme 1.2.[19]

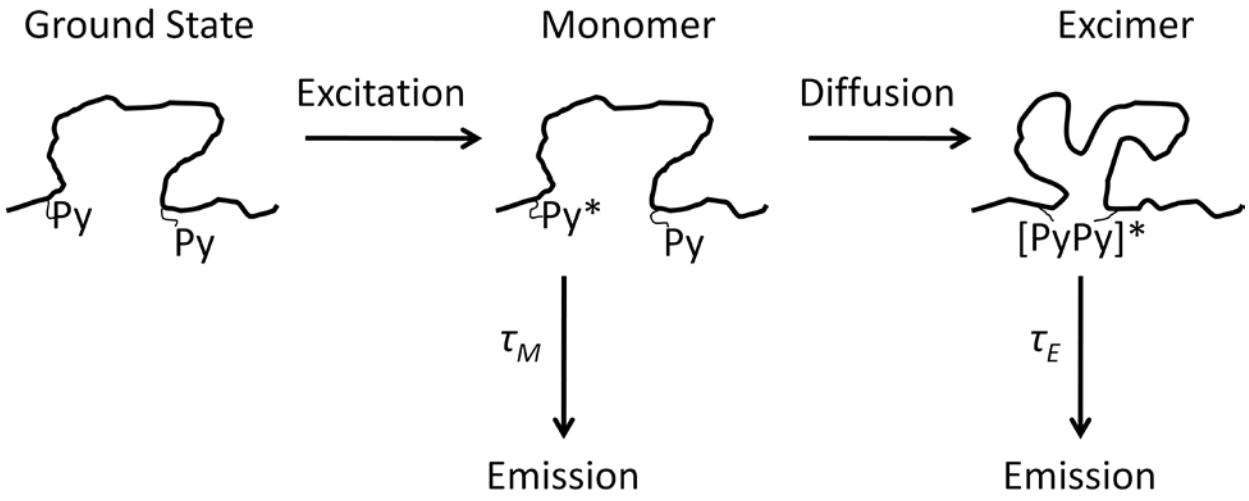

Scheme 1.2: Pyrene excimer formation.

The first instance where pyrene excimer formation was used to characterize polymer chain mobility was reported in 1976 by Zachariasse, to probe the ring closure of short alkyl chains end-labelled with pyrene.[20] This concept was further developed to study the end-to-end cyclization of various pyrene end-labelled polymers, and expanded to characterize the self-assembly of macromolecules.[18,21] But among the many studies dealing with pyrene-labelled polymers, three are particularly relevant for this work. In the first study, pyrene-labelled arborescent polystyrene samples were prepared to characterize their chain segmental density, using time-resolved

fluorescence to quantify the quenching of pyrene bound to the polymer by nitrobenzene as a function of generation number. The study showed that as the level of branching increased over successive generations, increased polymer density hindered the diffusion of nitrobenzene. This trend was most distinct for G2 and G3 arborescent polystyrene, where the level of branching increased from 2 800 to 18 000 side-chains in the last grafting reaction.[16]

The two other studies investigated the side-group dynamics of pyrene-labelled linear α-helical PGA by applying the Fluorescence Blob Model (FBM) to analyse their fluorescence decays. These studies demonstrated that excimer formation occurred between two pyrene labels bound to the backbone separated by approximately 20 glutamic acid units, indicating that the compact environment of the rigid α-helix backbone allowed for movement of the side-groups, and that the internal dynamics were affected by the side-group length.[22,23]

Together these three studies suggest that crowding in the interior of an arborescent polymer affects the dynamics, and that the FBM should provide an appealing analytical tool to probe these dynamics for arborescent polymers constituted of PGA branches.

1.4. Research Objectives

The research presented in this Thesis focuses on the characterization of the internal dynamics of a series of arborescent polymers derived from poly(L-glutamic acid) (PGA). Comparison of the solution properties of linear PGA with those of comb-branched and arborescent PGAs is expected to provide information about the interactions taking place between the PGA side-chains, similar to those occurring in proteins. The investigation presented herein includes the synthesis and the characterization of PGA samples by means of NMR, DLS, and steady-state and time-resolved fluorescence of pyrene labels attached to the PGA constructs.

1.5. Outline of the Thesis

This thesis is organized in the following manner. Chapter 2 reviews the synthesis and some of the properties of dendrimers and arborescent poly(L-glutamic acid) (PGA). In particular, it describes NMR and DLS experiments that were conducted on a series of PGA constructs to characterize their chain conformation in *N*,*N*-dimethylformamide (DMF) and in dimethyl sulfoxide (DMSO). Chapter 3 provides an introduction to fluorescence, some background information on pyrene, a description of the Birks scheme, and its application to the study of pyrene excimer formation in DMF and in DMSO. Chapter 4 extends the applicability of the Birks scheme to probe excimer formation between pyrene labels covalently attached to a macromolecule, provides an explanation of Fluorescence Blob Model (FBM) analysis, and describes the synthetic procedure used to label with 1-pyrenemethylamine the different PGA constructs investigated in this thesis. Analysis of the fluorescence behaviour exhibited by the pyrene-labelled PGA samples shows that differences between the internal dynamics in DMF and in DMSO result from their α-helical and random coil chain conformations, respectively. The last chapter presents the general conclusions resulting from this study and suggests ideas for future work.

2. Characterization of Poly(L-glutamic acid)

2.1. Introduction

In 1951 Linus Pauling characterized the α-helical conformation of polypeptides using X-ray diffraction.[24] Five years later, research on poly(γ-benzyl L-glutamate) (PBG) in solution led to the conclusion that PBG adopts conformations that include α-helix and random coil, depending on the solvent.[25] Further investigation concluded that a minimum of 10 repeat units are required to generate enough intramolecular hydrogen bonding along the PBG backbone to induce an α-helical conformation in *N*,*N*-dimethylformamide (DMF).[26] Recent studies used high resolution nuclear magnetic resonance (NMR) spectroscopy to probe the conformation of complex proteins of biological importance in solution.[27,28] Concurrently, synthetic chemists have focused on producing polypeptides with much higher molecular weights and lower polydispersity indices (PDI) for biomedical applications.[29–32] Arborescent polymers derived from linear PBG and poly(L-glutamic acid) (PGA) can be synthesized with low PDI values and molecular weights higher than the minimum number of repeat units required to form α-helices. Being globular and harboring a large number of α-helix forming side-chains, these PBG- and PGA-based macromolecules can be viewed as representative protein analogues.

This chapter provides background information on dendrimers and arborescent macromolecules, and the conversion of PBG to PGA. It describes the coil-to-helix transition of PGA in aqueous solution, and presents experimental evidence that PGA adopts α-helical and random coil conformations in DMF and in DMSO, respectively.

2.2. Background Information

2.2.1. Dendrimers and Arborescent Structures

Dendrimers are synthesized by sequential reaction cycles where branching monomer units are covalently attached to a multifunctional core. The dendrimer mass, *m*, increases according to the scaling law $m \propto f^G$, where *f* is the branching multiplicity and *G* is the generation number. The dendrimer volume, *V*, has been shown to increase as a function of the dendron size, *r*, according to the scaling law $V \propto (Gr)^a$ where the exponent *a* takes a value between 1.5 and 3.3.[33] These scaling laws imply that the dendrimer volume *V* increases more slowly than the overall dendrimer mass *m*, so that a dendrimer generation exists where the density of the dendrimer becomes so large that some of the end groups can no longer be located on their outer periphery and must fold back into the core. Whether the end-groups partition themselves into the core or at the periphery of the dendrimer is described theoretically by the core-dense[34,35] and shell-dense[36] models, respectively.

The structure of arborescent polymers has not been the subject of research to the same extent as dendrimers, however a limited number of reports indicate that they adopt similar topologies. A G0 comb-branched macromolecule is expected to adopt a prolate spheroid topology, where the chain segments are partly extended. Successive grafting cycles result in an increase in the generation number (G1, G2, etc.) and a more spherical topology.[37] The density of the spherical polymer changes as a function of the radius: The radial chain segment density of the G0 molecules is relatively constant, but with further grafting reactions the density of the shell increases according to the sequence G0 < G1 < G2 < G3, providing the justification that the shell-dense model is also applicable to arborescent structures.[38] Studies on arborescent

polystyrene with poly(ethylene oxide) side-chains indicated that the spherical topology is a consequence of the molecular weight of the side-chains used in their synthesis. The sphere size increases with an increase in the side-chain molecular weight and is consistent with observations that the side-chains essentially adopt a random coil conformation.[39] As compared to arborescent polystyrenes, arborescent polymers based on PBG and PGA exhibit the unique feature of having side-chains that can adopt different conformations. These conformations may in turn lead to novel topologies for this new family of arborescent polymers.

2.2.2. Synthesis

Low dispersity poly(γ-benzyl L-glutamate) (PBG) is synthesized by ring opening polymerization of the corresponding *N*-carboxyanhydride derivative using a primary amine initiator.[26,40] These side-chains can be grafted onto a linear PBG substrate using carbodiimide coupling, to create a comb-branched (or arborescent generation G0) polymer with a narrow molecular weight distribution. Further grafting reactions yield arborescent polymers of generations G1, G2, and G3 according to the procedure outlined in Scheme 2.1.

The benzyl side-groups of PBG are removed through acidolysis and conversion between poly(L-glutamic acid) and its poly(L-glutamate) sodium salt (PGNa) is achieved simply by adjusting the solution pH, as shown in Scheme 2.2. PGNa is more stable than PGA and is typically stored at a temperature of –20 ^{o}C.

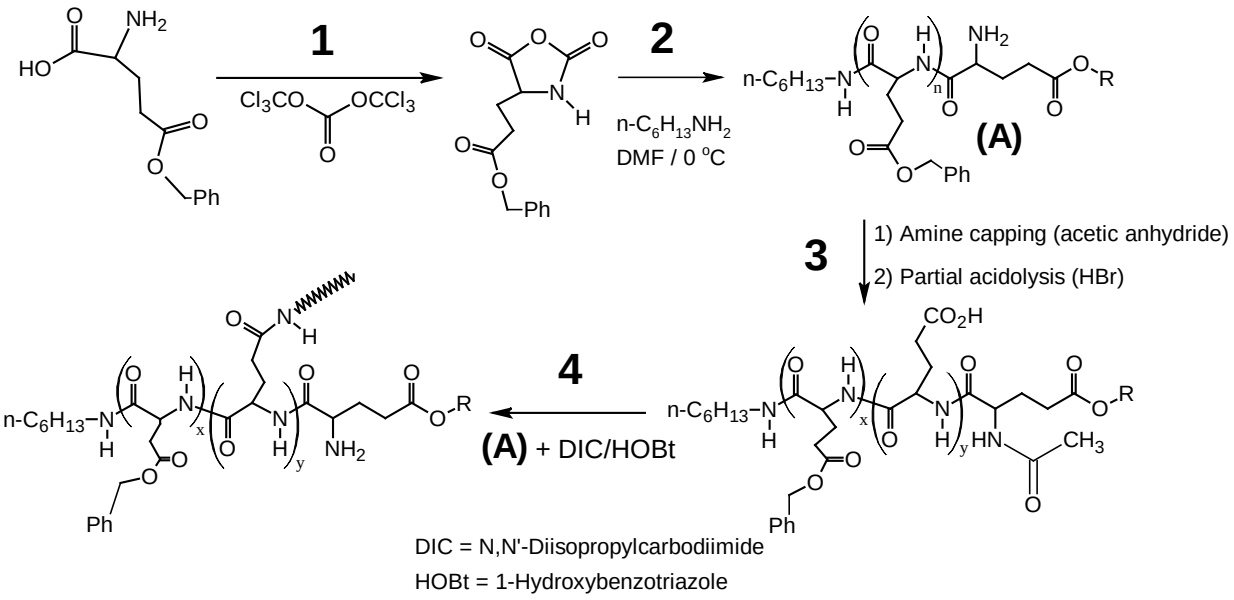

Scheme 2.1: Synthesis of a G0 arborescent PBG, with a comb-branched structure. G1–G3 arborescent structures are obtained by repetition of the partial acidolysis and grafting steps.[41]

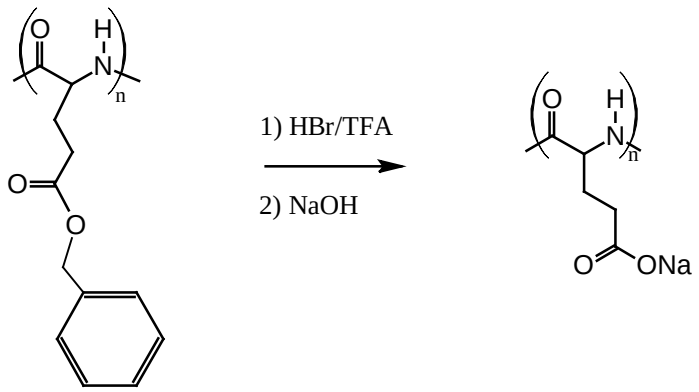

Scheme 2.2: Acidolysis of poly(γ-benzyl L-glutamate) to produce the sodium salt form of poly(L-glutamic acid).

2.2.3. Polymer Conformation

Our laboratory has shown by ^{1}H NMR analysis that the side-chains of arborescent PBG adopt different conformations in DMF and in DMSO. The α-proton signal was found to resonate at a lower frequency when enclosed in the rigid confines of an α-helix than when experiencing the diffuse and flexible environment of a random coil. This shift in frequency experienced by the α-proton signal as a function of polypeptide conformation has been established earlier for PBG in DMF and in DMSO, as well as in other studies of polypeptides undergoing a helix-to-coil transition in aqueous and organic solvents.[17,42–45]

Similarly, poly(L-glutamic acid) undergoes a coil-to-helix transition in water when the solution pH is changed from 6 to 4.[46,47] This transition can be detected using ^{1}H NMR spectroscopy, by monitoring the chemical shift of the signals for the protons in the backbone and side-groups. The coil-to-helix transition is also associated with characteristic peak broadening reflecting the lower mobility of the polymer in the helical conformation.[43,48,49]

2.2.4. Hydrodynamic Size

The chain conformation of polypeptides can also be probed using quasi-elastic scattering measurements. Ptitsyn *et al.* thus reported that X-ray scattering curves exhibit a maximum occurring at angles below 10^{o} for linear poly(L-glutamic acid) that is not present in the scattering curves for poly(L-glutamate), an observation that is consistent with conformational differences also established for other helical polypeptides.[50] Arborescent polymers, that have large dimensions in solution, can be studied using dynamic light scattering (DLS) by probing differences in the hydrodynamic volume of the macromolecules which can be attributed to distinct conformational states.

The hydrodynamic diameters (D_h) obtained by DLS for arborescent PBG in DMF and in DMSO are presented in Table 2.1.[41] The similar first- and second-order D_h values retrieved for all arborescent PBGs indicate that these macromolecules have a uniform molecular size distribution. The close to 50% increase in D_h going from DMF to DMSO is attributed to a conformation change of the arborescent polymers, where the side-chains adopt an extended random coil conformation in DMSO and a compact α-helical conformation in DMF.

Table 2.1: Hydrodynamic diameter of arborescent poly(γ-benzyl L-glutamate) in DMF and in DMSO with 0.05% LiCl.[41]

	DMF		DMSO	
Generation	1st order	2nd order	1st order	2nd order
G1	10.7	8.4	15.7	14.1
G2	13.1	12.1	21.3	20.1
G3	24.5	23.5	34.5	32.5

DLS measurements conducted on PGA in pH 10 aqueous buffer, where most glutamic acids are negatively charged, indicated that the PGNa constructs are present as two distinct species. Since the comb-branched and arborescent polymers are synthesised from polymer chains initiated by *n*-hexylamine (see Scheme 2.1), in aqueous solutions these hydrophobic initiator segments located at the surface of the arborescent polymers provide the driving force for the self-assembly of the negatively charged arborescent PGAs. The larger and smaller species detected

by DLS correspond to polymeric aggregates, and isolated macromolecules, respectively. The hydrodynamic diameters of the isolated arborescent polymers are listed in Table 2.2.[51]

Table 2.2: Hydrodynamic diameter of isolated comb-branched and arborescent poly(L-glutamate) molecules in water.[51]

Generation	Diameter
G0	12.4
G1	17.0
G2	25.0
G3	30.2

Comparison of the hydrodynamic diameter of arborescent PBGs in DMSO with those of PGA in aqueous solution (pH 10) provides further indication that DMSO is a non-helicogenic solvent for PBG, since their D_h values are only slightly lower than those of poly(L-glutamate).

2.3. Experimental Procedures

The characteristics of the PBG samples used in the current investigation are provided in Table 2.3.[41] The number-average degree of polymerization, DP_n, and molecular weight, M_n^{NMR}, were determined from analysis of the ^{1}H NMR spectra. The M_n and the polydispersity index, M_w/M_n, of all the PBG constructs were determined by gel permeation chromatography (GPC) analysis with a multi-angle laser light scattering detector, except for the linear PBG sample which was analysed by ^{1}H NMR spectroscopy. The branching functionality corresponds to the average number of side-chains that were added in the last grafting cycle. It was also determined by GPC analysis.

Table 2.3: Characteristics of arborescent PBG samples of successive generations.[41]

Generation	Graft polymer		Side-chains		Branching functionality
	M_n (g·mol^{-1})	M_w/M_n	M_n^{NMR} (g·mol^{-1})	DP_n	
Linear†	3.60×10^3	1.09	-	-	-
G0	5.30×10^4	1.04	6600	30	6.6
G1	1.33×10^5	1.06	4000	18	28
G2	4.86×10^5	1.03	3900	17	124
G3	1.06×10^6	1.03	3900	17	289

†M_n calculated using a DP_n of 16 determined from ^{1}H NMR spectroscopy.

Solvent and Reagent Purification: All reagents were purchased from Sigma-Aldrich and used as received unless otherwise stated. DMF used for the synthesis was dried over calcium

hydride overnight before distillation under reduced pressure. Doubly distilled deionized water obtained from a Millipore Milli Q UF Plus (Bedford, MA) system was used.

Synthesis of Poly(L-glutamic acid) Sodium Salt (PGNa): In a 25 mL round bottom flask, G3 PBG (0.5 g, 2.3×10^{-3} mol benzyl glutamate units) was dissolved in 5 mL of trifluoroacetic acid and 0.5 mL of HBr solution in acetic acid (33% HBr by weight; 8.7×10^{-3} mol HBr) was added with stirring. After 3 hours, 5 mL of anhydrous diethyl ether were added to induce precipitation, and 5 mL of acetone were added to partially solubilise the product. The slurry was then added drop-wise to 150 mL of diethyl ether with stirring. The polymer was recovered by suction filtration and washed three times with 10 mL portions of acetone. The polymer was further purified by suspension in 10 mL of acetone, sonication for 5 min, and suction filtration. The resulting chalky white solid was dissolved in 3 mL of DMF and 3 mL of 1 N aqueous NaOH, and placed in a regenerated cellulose bag with a 1000 MW cut-off to be dialyzed against H_2O for 6 hours. The solid (0.2 g) was recovered by lyophilisation of the solution collected from the dialysis bag. ^{1}H NMR analysis confirmed the absence of benzylic resonances at 5.0 and 7.3 ppm.

Nuclear Magnetic Resonance Spectroscopy: Conformation analysis of poly(L-glutamic acid) was carried out on a Bruker 500 MHz spectrometer at a concentration of 5 mg/mL in DMF-d7 or in DMSO-d6. The spectra were calibrated using characteristic solvent peaks at 8.0 ppm and 2.5 ppm in DMF-d7 and in DMSO-d6, respectively. A 300 MHz Bruker instrument was used to acquire the NMR spectra for PGA in D_2O at a concentration of 10 mg/mL, the spectrum was calibrated to the chemical shift of water at 4.8 ppm. The pD of the aqueous PGA solutions were approximated by measuring the pH of PGA in H_2O solution using a pH meter with a calomel glass combination pH electrode.

Laser Light Scattering: A Brookhaven BI-200SM laser light scattering goniometer was used for the dynamic light scattering experiments. A BI-9000AT digital autocorrelator with a HeNe laser was used and the detector was set to 636 nm. The sample concentration equalled 10 mg/mL, with 0.5 mg/mL LiBr (0.05% w/v) added to suppress aggregation. The experiments were carried out at 25 ^{o}C, and measurements were recorded at seven angles between 60^{o} and 150^{o}. The GENDIST software used for data analysis relied on the regularized positive exponential sum (REPES) algorithm to perform a regularized inverse Laplace transform on the intensity correlation functions of the dynamic light scattering data according to Equations 2.1-2.3, where $g^{(2)}(t)$ is the normalized intensity correlation function, $I(t)$ is the intensity of light scattered at time t, $I(t+\tau)$ is the intensity of scattered light at a correlation time τ, $g^{(1)}(t)$ is the normalized electric field correlation function, β is an instrument parameter that accounts for non-ideal correlation, and $A(\tau)$ is the amplitude intensity as a function of the specific correlation times.[52–55]

$$g^{(2)}(t) = \frac{\langle I(t)\, I(t+\tau)\rangle}{\langle I(t)^2\rangle} \tag{2.1}$$

$$g^{(2)}(t) - 1 = \beta \left| g^{(1)}(t) \right|^2 \tag{2.2}$$

$$g^{(1)}(t) = \int_0^\infty \tau A(\tau) \exp(-t/\tau) d \ln \tau \tag{2.3}$$

The REPES method establishes a grid of possible correlation times and determines values for the amplitude by least-squares analysis. The grid density was 12 correlation times per abscissa decade for all samples, such that the resulting distribution functions were smooth. This analysis method allows for a second smoothing parameter, the *probability to reject*. It was set to

0.5 for the G3 samples, as it has been shown to adequately represent the distribution functions for arborescent poly(L-glutamate) in water.[51] For the G2 and G1 samples the probability to reject was set to 0.01, to allow separation of the average correlation time for the macromolecules from the average correlation time for the larger polymeric aggregates.

According to Equation 2.4 the diffusion coefficient, *D*, was calculated from the slope of the line obtained by plotting the inverse of the correlation times τ, Γ, as a function of q^2. The parameter τ was obtained by fitting the autocorrelation function acquired at six angles from 60° to 135° and q^2 is defined by Equation 2.5, where θ is the angle between the detection axis and the direction of the transmitted beam, λ is the wavelength of light (636 nm), and n_o is the refractive index of the solvent equal to 1.429 and 1.475 for DMF and DMSO, respectively. The measurements obtained at the largest angle (150°) were discarded from the calculation of *D*, since these results are least reliable when a spread in size distribution induces an artificial increase in scattering intensity.[56] The hydrodynamic diameter, D_h, was calculated from *D* according to Equation 2.6 by assuming a spherical geometry for the molecules studied. In Equation 2.6, k_B is the Boltzmann constant, *T* is the absolute temperature (298 K), and η is the solvent viscosity, equal to 0.79 mPa·s and 2.0 mPa·s for DMF and DMSO, respectively. The absolute error associated with D_h was approximated by linear regression analysis of the Γ vs q^2 plot.

$$\frac{1}{\tau} = \Gamma = Dq^2 \tag{2.4}$$

$$q^2 = \frac{4\pi n_o \sin\left(\theta/2\right)}{\lambda} \tag{2.5}$$

$$D_h = \frac{k_B T}{3\pi\eta D} \tag{2.6}$$

2.4. Results and Discussion

2.4.1. Nuclear Magnetic Resonance Spectroscopy

The ^{1}H NMR spectra obtained for the G2 arborescent PBG sample and its corresponding PGA derivative are compared in Figure 2.1. The peaks at 7.3 and 5.0 ppm, representing the benzylic protons of the side-groups in the top spectrum are essentially absent in the bottom spectrum, indicating a successful acidolysis reaction.

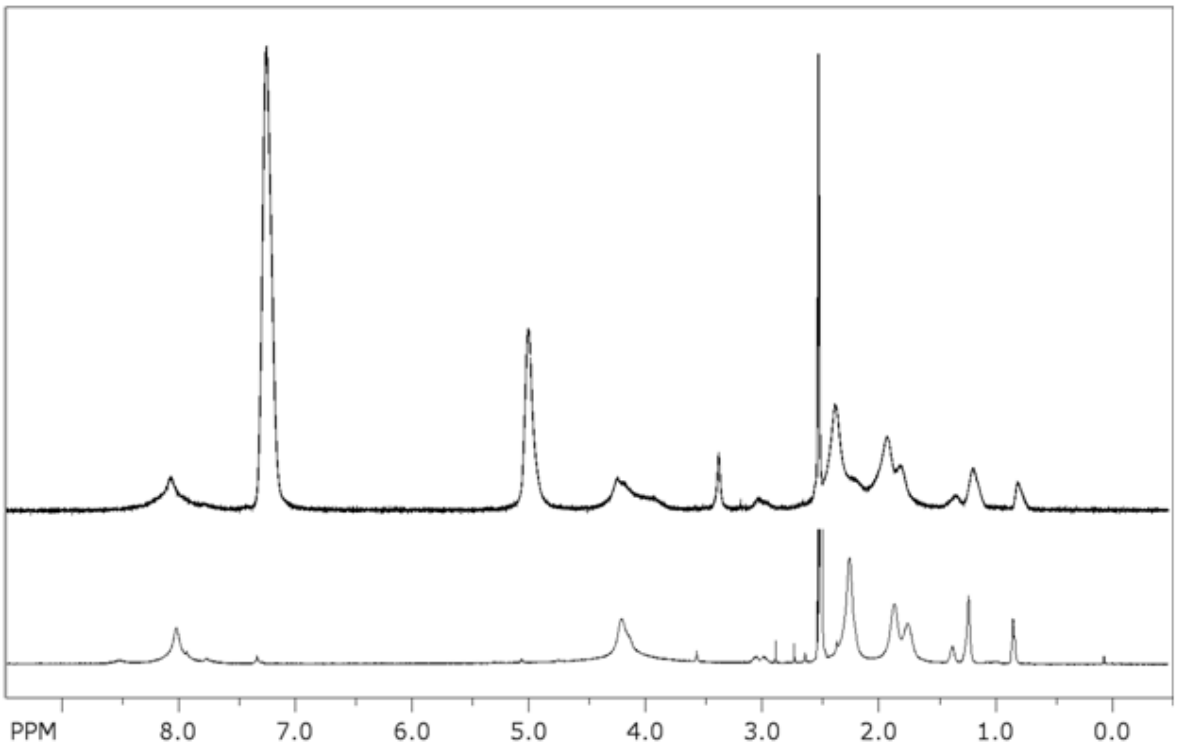

Figure 2.1: NMR spectra (500 MHz, in DMSO-d6) for G2 arborescent poly(γ–benzyl L–glutamate) (top), and G2 poly(L-glutamic acid) (bottom).

The ^{1}H NMR spectra of G1 PGA in aqueous solution under basic (pD 8) and acidic (pD 5) conditions are shown in Figure 2.2. Their spectral features are consistent with those observed in similar studies where PGA was shown to undergo a coil-to-helix transition.[43,48,49] The signals for the γ- and β-protons in the side-group shift downfield from 2.1 to 2.3 ppm and from 1.9 to 2.0 ppm, respectively. This shift is due to disruption of the backbone-side-group interactions and side-group-side-group interactions as the chain conformation changes from a diffuse random coil to an α-helix.[57] The α-proton signal is also expected to change based on literature reports for PBG and high molecular weight linear PGA in water.[17,43,48] However, for arborescent PGA synthesized from shorter polymer segments, the observed shift from 4.20 at high pH to 4.16 at low pH is too subtle to draw any conclusions. The peak still broadens at lower pH, due to lower mobility of the α-proton when the backbone is locked in the α-helical conformation. This reduction in mobility is also observed for the γ- and β-protons in the side-group. The other signals at 0.8 (3H), 1.2 (6H), 1.4 (2H) and 3.1 (2H) ppm in Figure 2.2 are attributed to protons in the *n*-hexylamine initiator fragment. Their position does not change in DMF or in DMSO, because they are located at the polymer chain ends and are unaffected by the coil-to-helix transition. Lastly, a signal at 8.2 ppm appears in the spectrum acquired at pH 5, and is attributed to the backbone amide protons. In basic D_2O solution the amide proton exchanges rapidly with deuterium, which prevents its detection. At low pH the exchange with deuterium is less significant and the amide proton appears as a broad peak consistent with the slow dynamics experienced by the α-helical backbone.

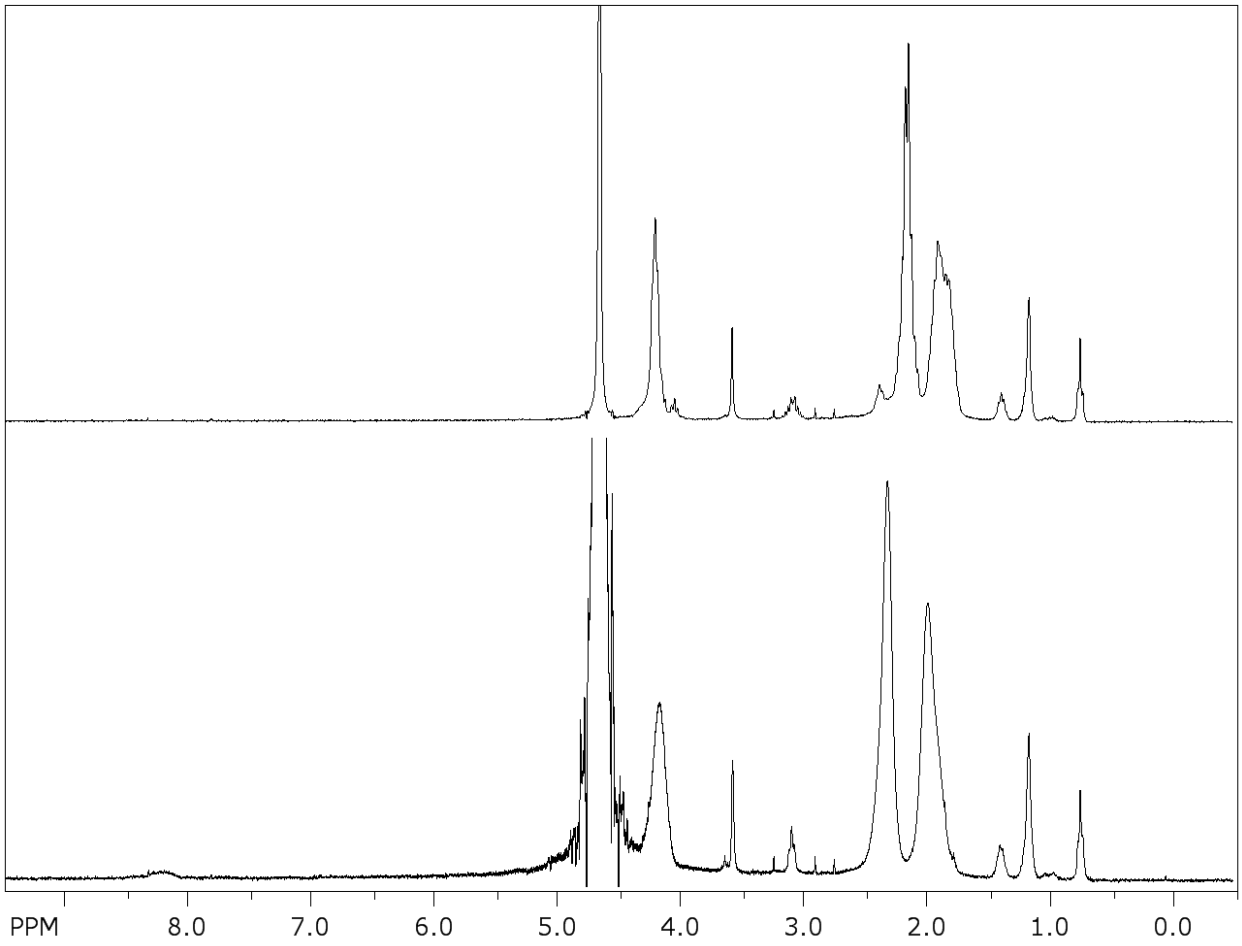

Figure 2.2: NMR spectra (300 MHz) for G1 arborescent PGA in D_2O at pD 8 (top), and with 2% v/v HCl added, pD 5 (bottom).

The NMR spectra obtained for G1 arborescent PGA in DMF-d7 and in DMSO-d6 are compared in Figure 2.3. The signals at 2.6 and 3.5 ppm in the top spectrum correspond to DMSO and water, respectively, and proton signals from DMF appear at 2.7, 2.9 and 8.0 ppm in the bottom spectrum. The spectral features suggest that the PGA chain conformations are respectively helical and coiled, as they mimic those obtained in D_2O at low and high pD. In particular, the signals from the γ- and β-protons are shifted upfield in DMSO as compared to DMF, and show much less line broadening consistent with the more mobile backbone of PGA

adopting a random coil conformation. Furthermore, the amide proton signal is much sharper in DMSO than in DMF, consistent with higher backbone mobility experienced by the PGA side-chains that adopt a random coil conformation in DMSO.

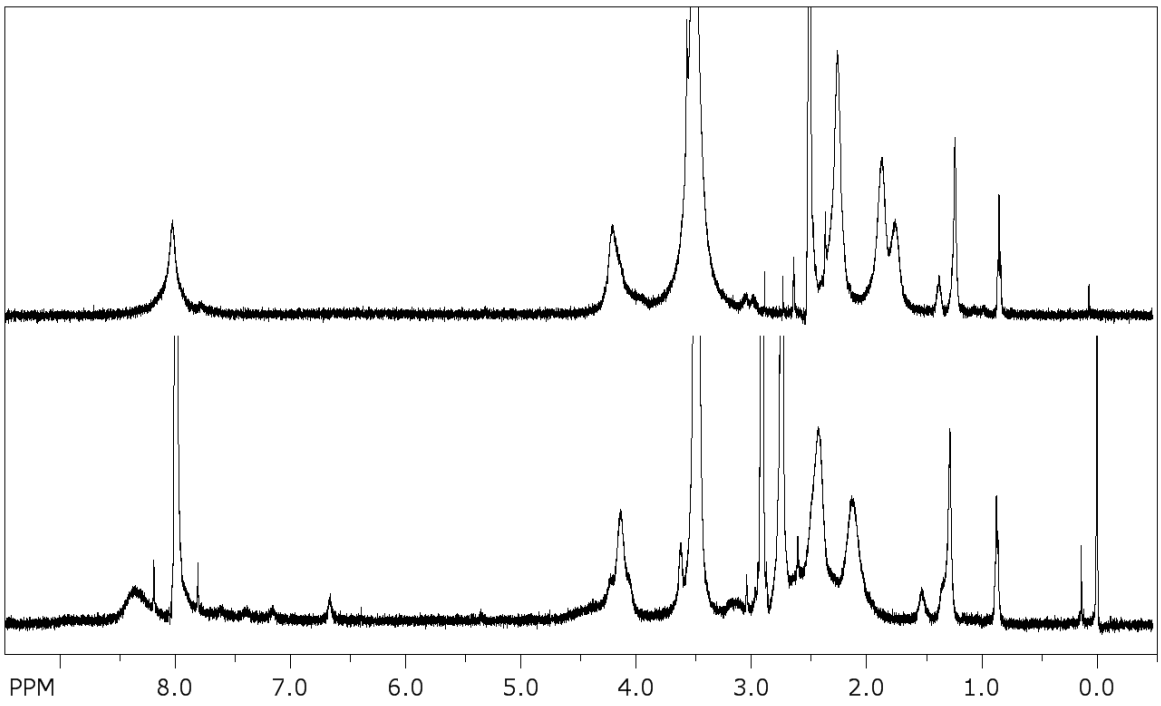

Figure 2.3: NMR spectra for G1 arborescent PGA in DMSO-d6 (top), and DMF-d7 (bottom).

Comparison of the NMR spectra in Figures A1 and A2 in the Appendix, for increasing generations of arborescent PGAs, indicates that the peaks broaden according to the sequence linear < G0 < G1 < G2 < G3, which reflects slower tumbling for the larger macromolecules. Figure 2.4 provides enlarged α-proton regions for the G2 and G3 arborescent PGA samples in DMF-d7, to illustrate changes in the peak shape due to increased branching functionality, which in turn results in conformation changes. The G3 arborescent PGA sample exhibits a dominant peak at 4.14 ppm, corresponding to an α-helical chain conformation. However, unresolved peaks

may also be observed between 4.2 and 4.5 ppm, due to parts of the macromolecule adopting a more random coil conformation. The simultaneous existence of structured α–helices and denatured random coils within the same arborescent polypeptide is reminiscent of the molten globular state taken by some polypeptides along the folding pathway toward their 3-dimensional final struture. While both random coils and α–helices are expected to exist in all arborescent polypeptides, the NMR spectra shown in Figure 2.4 indicate that the molten globule character of the arboresent PGAs is most pronounced for the G3 arborescent PGA sample since the random coil conformation is significantly dimished in the G2 arborescent PGA sample (Figure 2.4) and the G0 and G1 arborescent PGA samples (Figure A1) in DMF-d7.

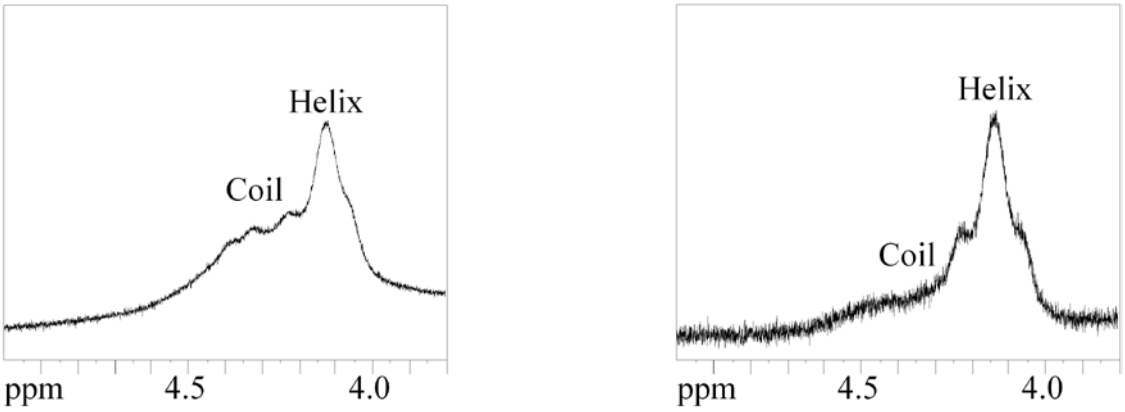

Figure 2.4: NMR spectra for the G3 (left) and G2 (right) arborescent PGA samples in DMF-d7 corresponding to the α-proton signal.

2.4.2. Dynamic Light Scattering

The angular dependence of the distribution functions depicted in Figure 2.5 for the G3 arborescent PGA sample in DMSO indicates that there is no aggregation. The position of the

peak maxima in Figure 2.5 yields the average correlation time τ, whose inverse $\Gamma=1/\tau$ is plotted in Figure 2.6 as a function of q^2, calculated according to Equation 2.5. Γ increases linearly with q^2 as predicted by Equation 2.4. The good linearity observed in Figure 2.6 demonstrates that the particles are uniform in size. This indicates that the low sample polydispersity of the PBG constructs was not affected by the acidolysis conversion of PBG to PGA.

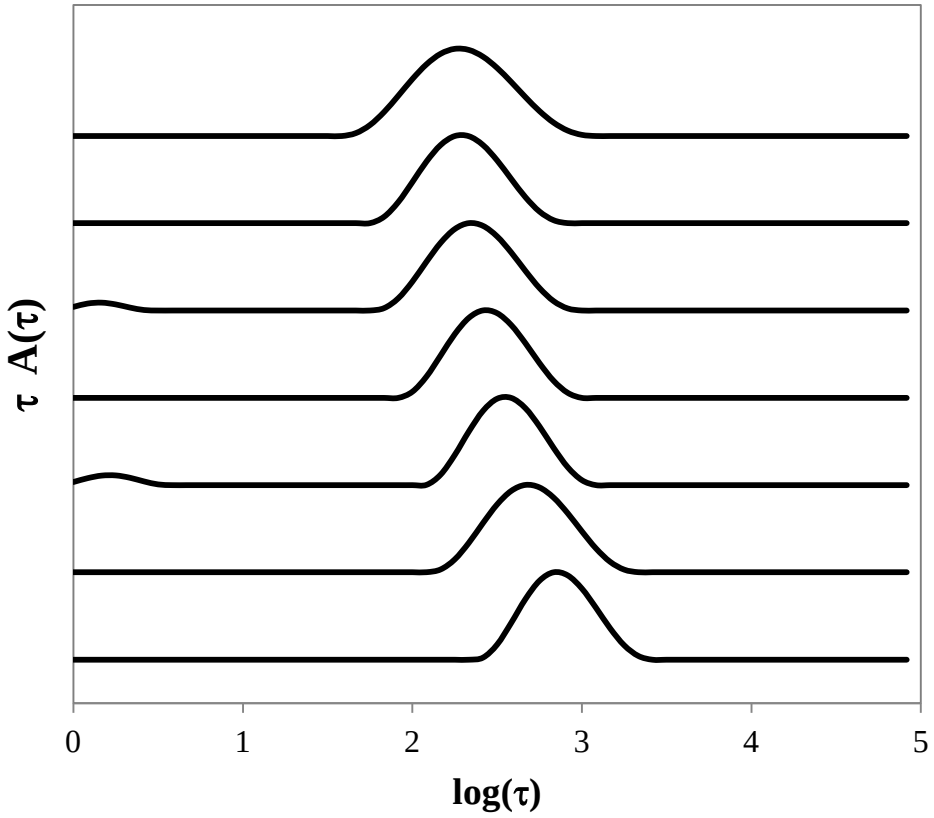

Figure 2.5: Distribution functions for the time decay rate of scattered light intensity by G3 PGA in DMSO, measured at 150°, 135°, 120°, 105°, 90°, 75°, and 60° (top to bottom).

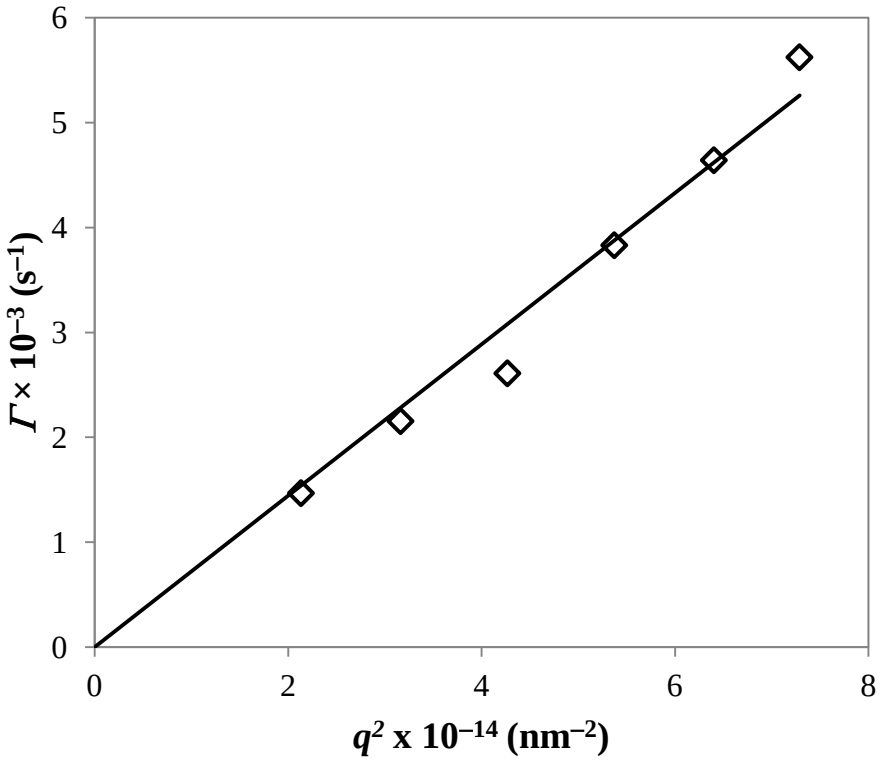

Figure 2.6: The q^2 dependence of the relaxation rate of scattered light intensity for the diffusion coefficients of G3 PGA in DMSO.

The complete results for DLS measurements of PGA in DMF and in DMSO are presented in Appendix B. Based on the correlation time histograms shown in Figures B4, B6 and B7 in the Appendix, the G1 and G2 PGA samples were found to self-assemble into large aggregates. However, the histograms shown in Figures 2.5, B3, B4, B5, B6 and B7 are the results of correlation function analysis that is based on light scattering intensity, which is extremely sensitive to the presence of large particles. Analysis of the correlation functions generated in a DLS experiment can be carried out either in terms of particle volumes or particle numbers. Analysis of the G1 PGA autocorrelation function using particle numbers instead of scattering

intensities indicates that when the signal intensity contributions are split almost equally between 44% small particles and 56% large aggregates, the population histogram in terms of number of particles is weighted strongly in favour of the smaller particles, as shown in Figure B8 in the Appendix. Thus, these aggregates represent a very small fraction of the particle population present in solution and have a negligible effect on the size measurements of the individual polymers. Variations in the salt content of the sample solutions did not eliminate these large aggregates, indicating that the formation of intermolecular aggregates is a result of high sample concentration rather than the ionic strength of the solution.

The hydrodynamic diameters obtained for arborescent PGA samples in DMF and in DMSO are summarized in Table 2.4. The size of the G1 and G2 PGA constructs in DMF is smaller than in DMSO. This result is consistent with what has been observed for arborescent PBG (Table 2.1). These trends can be rationalized based on the NMR analysis results and the understanding that in DMF the polypeptide side-chains adopt an α-helical conformation, which leads to a more compact structure for the arborescent PGA molecules. The good agreement observed between the D_h values obtained for PGA in DMSO and those reported for PGNa in aqueous buffer at pH 10 (Table 2.2) indicates that the PGA side-chains adopt similar random coil conformations in both solvents. However the D_h value for G3 PGA in DMF is larger than would be expected based on the trends observed for the G1 and G2 PGA samples, and the G3 PBG sample in DMF and in DMSO. As pointed out earlier, the NMR spectrum for G3 PGA in DMF (Figure 2.4) indicates that a substantial fraction of the PGA side-chains adopt a random coil conformation even in DMF, in contrast to the lower generation PGA samples. This may be an indication that steric crowding due to the high branching functionality of G3 PGA prevents some side-chains from adopting an α-helical conformation. As a consequence, the size of the G3 PGA molecules

in DMF is similar to the completely random coiled conformation obtained in DMSO. In contrast, the G3 PBG sample in DMF was shown to have a smaller D_h in DMF than in DMSO, suggesting that most of the side-chains of G3 PBG in DMF are α-helical. This difference in behaviour between the G3 PBG and PGA samples might be due to π-π staking of the PBG benzyl ester substituents, stabilizing the α-helical conformation within the dense interior of the G3 arborescent PBG molecules.

Table 2.4: Hydrodynamic diameter of arborescent PGA in DMF and in DMSO, with 0.05% LiBr added.

Generation	Diameter	
	DMF	DMSO
G1	11.0 ± 0.6	16.4 ± 0.3
G2	15.4 ± 0.5	20.7 ± 0.4
G3	31.2 ± 0.5	30.3 ± 0.9

2.5. Conclusions

The results presented in this chapter show that arborescent PGA molecules display different characteristics depending on the solvent used. The variations observed in peak position and shape for the α-, β-, and γ-protons in the NMR spectra of the PGA constructs in D_2O, in DMF and in DMSO are consistent with earlier studies describing coil-to-helix transitions.[43,48,49] The hydrodynamic diameter measurements show that the PGA constructs in DMSO have an expanded volume due to the random coil conformation adopted by their side-chains. In DMF, the PGA backbone is stabilized by hydrogen-bonding and the PGA side-chains adopt a predominantly α-helical conformation, with more significant amounts of random coil conformation induced by the steric constraints present in the highly branched G3 arborescent polymer molecules. The conformation changes observed in these polymer samples indicate that they are suitable to mimic globular proteins. Their intramolecular chain dynamics will be studied using pyrene excimer formation in the following chapters.

3. Fluorescence

3.1. Introduction

This chapter presents background information on fluorescence, its application to study pyrene excimer formation, and some experimental results for pyrene excimer formation in *N*,*N*-dimethylformamide (DMF) and in dimethyl sulfoxide (DMSO), as these solvents have been shown in Chapter 2 to affect the chain conformation of poly(L-glutamic acid). Fluorescence measurements carried out with 1-pyrenemethylacetamide will provide a benchmark for pyrene excimer formation in solution, against which any deviations for pyrene covalently bound to poly(L-glutamic acid) will be attributed to the polymer chain dynamics.

3.2. Background Information

3.2.1. Fluorescence

The energy states of a chromophore are described by the Jablonski diagram shown in Figure 3.1, where each electronic state (S_0, S_1, etc.) is divided into a number of vibrational levels. Upon absorption of an ultraviolet or visible photon of energy *hv*, the molecule is promoted from the ground state (S_0) to an upper vibrational excited state, $S_{2,2}$. Subsequent relaxation to the ground-state proceeds through several photophysical pathways. First the molecule relaxes its excess energy down to the $S_{1,0}$ level by a process called internal conversion. Subsequently, the molecule may release its remaining excess energy by relaxing to one of the vibrational levels of the ground-state via the emission of a photon, a process referred to as fluorescence.

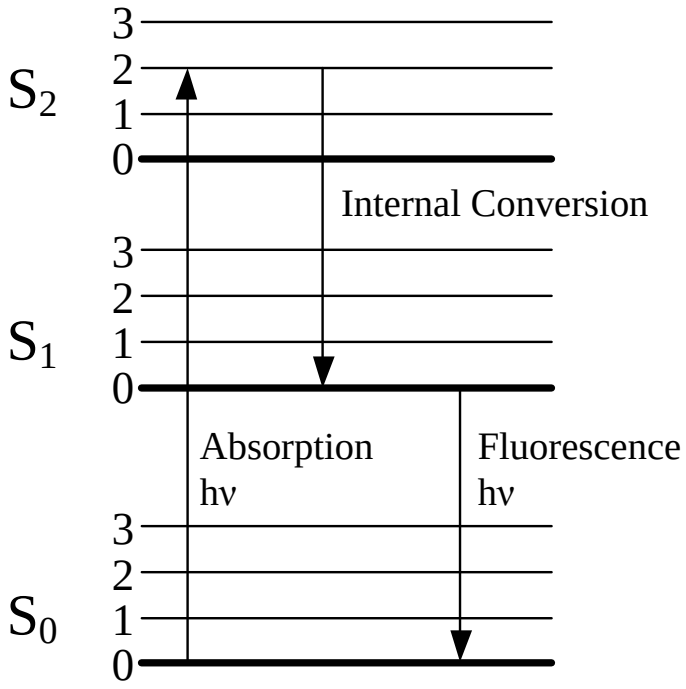

Figure 3.1: Jablonski diagram depicting the energy changes associated with absorption, internal conversion, and fluorescence.

The photophysical properties of a chromophore are described by two parameters: The molar extinction coefficient, that describes the propensity of a molecule to absorb ultraviolet and visible (UV-Vis) light at a given wavelength, and the fluorescence quantum yield, which is the efficiency of a molecule at emitting a fluorescence photon for each absorbed photon. Pyrene is an appealing chromophore because of its large extinction coefficient (on the order of 40,000 $mol^{-1} \cdot L \cdot cm^{-1}$) and high fluorescence quantum yield (0.32 in cyclohexane).[58] Its long fluorescence lifetime and ability to form excimer further contribute to making pyrene the fluorescence probe of choice to study the internal dynamics of a variety of macromolecules and their supramolecular assemblies.[18] When no specific interactions exist between pyrene and a macromolecule, the use of pyrene as a fluorescent probe requires covalent attachment to the

macromolecule through a linker containing a reactive functional group. The nature of the substituent affects the quantum yield, molar extinction coefficient, lifetime, and the allowed energy transitions of the pyrene moiety.[59–61] Figure 3.2 shows the chemical structure of pyrene and two of its derivatives.

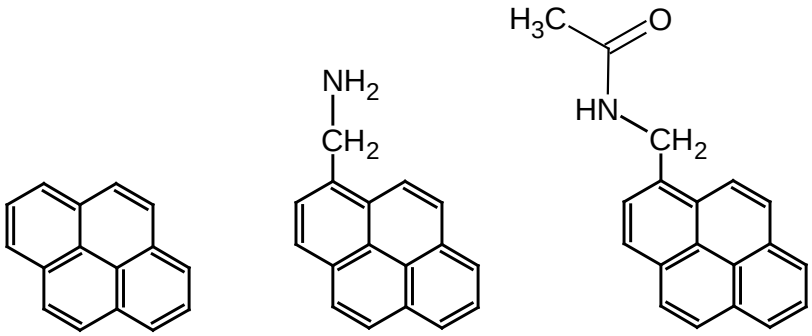

Figure 3.2: Chemical structures of pyrene, 1-pyrenemethylamine, and 1-pyrenemethylacetamide (left to right).

3.2.2. Fluorescence Emission

A steady-state emission spectrum for 1-pyrenemethylacetamide is shown in Figure 3.3, where the pyrene monomer fluoresces as sharp peaks in the 370-420 nm range and the excimer shows a broad emission centered at 480 nm. The regions of the spectrum shown in black are used to characterize the efficiency of excimer formation measured by the I_E/I_M ratio, calculated by taking the ratio of the florescence intensity of the excimer integrated from 500 to 530 nm over that of the monomer integrated from 372 to 378 nm. Although the excimer emits over a wide range, its intensity is integrated only in the specified region to avoid including any residual monomer emission tailing into the wavelength range where the excimer emits. The emission

spectrum for molecular pyrene was acquired with the so-called front-face geometry, to minimize the inner filter effect.[62] For pyrene-labelled polymer samples, intermolecular excimer formation is prevented by analyzing samples at low concentration, i.e. in solutions with an absorbance at 344 nm of 0.1 or lower, corresponding to a pyrene concentration below 2.5 μM.

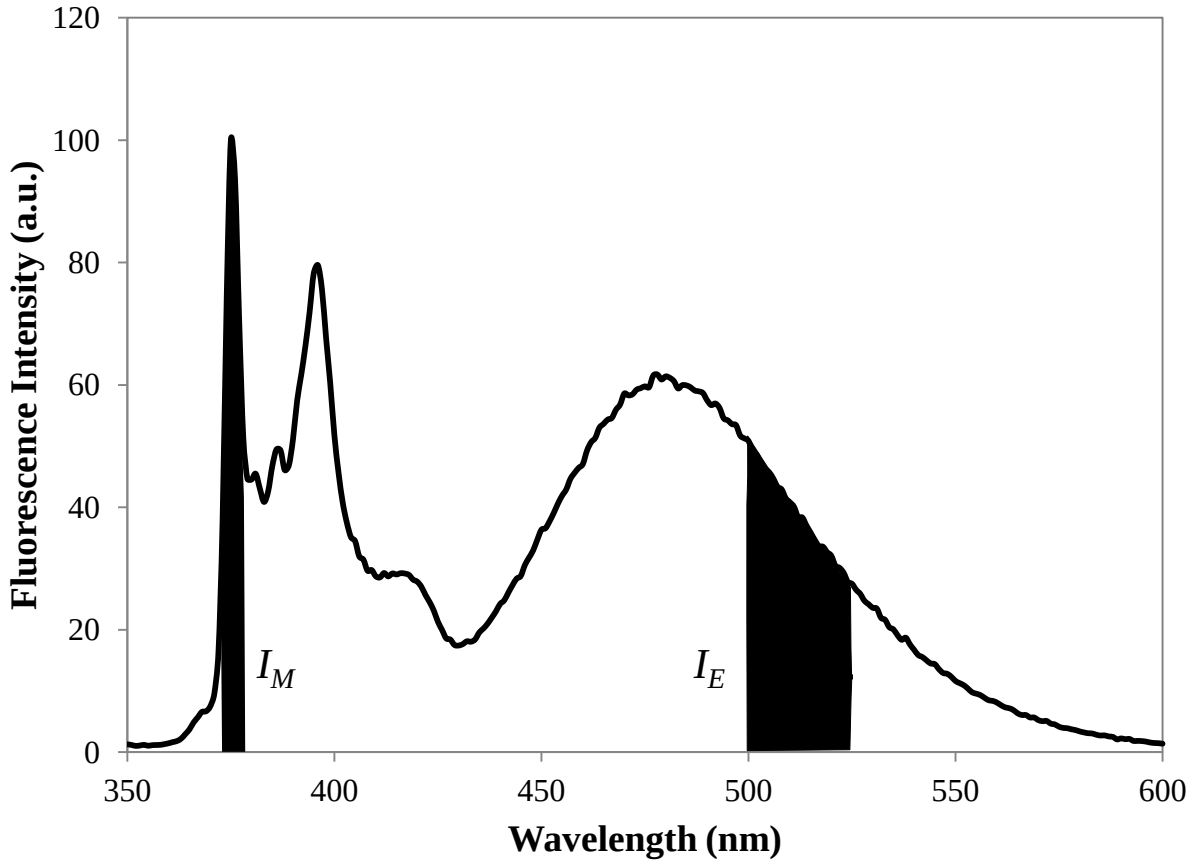

Figure 3.3: Steady-state fluorescence spectrum for 1-pyrenemethylacetamide in DMF (11 mM). λ_{ex}= 344 nm.

The I_E/I_M ratio is a measure of the efficiency of pyrene excimer formation. For dilute solutions of pyrene-labelled macromolecules at temperatures lower than 30 ^oC, where excimer

dissociation can be neglected,[18] the I_E/I_M ratio can be expressed by Equation 3.1 where κ is an instrumental constant associated with the spectrofluorometer used, τ_M is the natural lifetime of the pyrene monomer, k_1 is the bimolecular rate constant for excimer formation, [*Py*] is the concentration of ground-state pyrene, and ϕ_E^o and ϕ_M^o are the quantum yields for the excimer and monomer emissions, respectively.[19] Equation 3.1 implies that the I_E/I_M ratio increases linearly with τ_M and the pyrene concentration in a homogenous pyrene solution. A similar equation may be used for pyrene-labelled macromolecules where [*Py*] is replaced by $[Py]_{local}$, the local pyrene concentration inside the molecular volume defined by the macromolecule. In this case I_E/I_M increases with the pyrene content within the macromolecules as $[Py]_{local}$, but cannot be determined experimentally.

$$\frac{I_E}{I_M} = \kappa \frac{\phi_E^o}{\phi_M^o} \tau_M k_1 [Py] \tag{3.1}$$

3.2.3. Excimer Formation

For a homogenous pyrene solution, excimer formation can be described using a collisional quenching model and by considering the excited and ground-state pyrenes as two identical sphere-like particles.[63] The rate constant for excimer formation can be determined by applying the Einstein-Smoluchowski diffusion theory to obtain Equation 3.2[64]

$$k(t) = 4\pi N_A DpR\left(1 + \frac{pR}{\sqrt{\pi Dt}}\right) \tag{3.2}$$

where $k(t)$ is a time-dependent rate constant, N_A is Avogadro's number, p is the probability that a collision between an excited and a ground-state pyrene will result in excimer formation, R is the encounter distance, and D is the diffusion coefficient which can be expressed by Equation 3.3

$$D = \frac{k_B T}{6 \pi \eta r} \tag{3.3}$$

where k_B is the Boltzmann constant, T is the absolute temperature, η is the solvent viscosity, and r is the hydrodynamic radius of the molecule. Equations 3.1-3.3 imply that the ratio I_E/I_M should decrease with increasing solvent viscosity.

According to Equation 3.2 $k(t)$ depends on time, which complicates the analysis of fluorescence dynamic quenching measurements conducted in high viscosity solvents. Fortunately, many organic solvents have a viscosity low enough to neglect the transient effects of Equation 3.2. Under such conditions k is a constant equal to $4\pi N_A DpR$, and the Birks scheme can be applied to determine the rate constant of pyrene excimer formation from the analysis of time-correlated fluorescence decays.[64]

3.2.1. Birks' Scheme

The Birks scheme is depicted in Scheme 3.1. After absorption of a photon by pyrene, subsequent interactions between the excited pyrene, *Py**, and a ground-state pyrene, *Py*, result in the formation of excimer, *E**, k_1 and k_{-1} being the excimer formation and dissociation rate constants, respectively. The excited states *Py** and *E**, with lifetimes τ_M and τ_E, respectively, eventually emit a photon and return to the ground state.

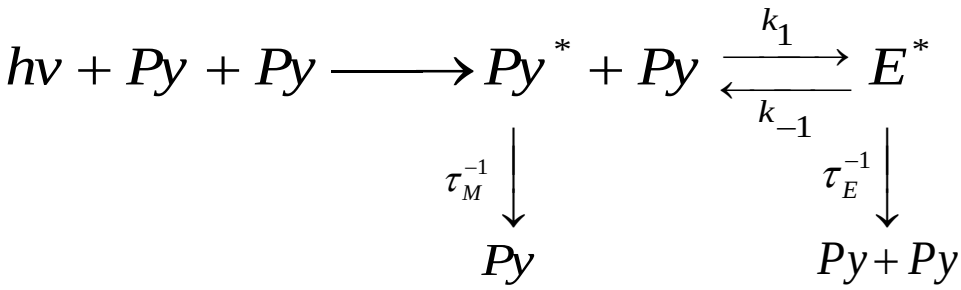

Scheme 3.1: Birks' scheme describing excimer formation for molecular pyrene.

The kinetics of pyrene excimer formation presented in Scheme 3.1 are handled by Equations 3.4 and 3.5, which are two differential equations that after integration yield Equations 3.6 and 3.7, describing the time-dependant concentration profiles [*E**] and [*Py**], respectively. In Equations 3.6 and 3.7, $X = k_1 + \tau_M^{-1}$, $Y = k_{-1} + \tau_E^{-1}$, and the species Py^*_{diff}, Py^*_{free}, and Py^*_S, represent the pyrenes that, respectively, form excimer by diffusion, do not form excimer, and form poorly stacked pyrene dimers that emit with a short lifetime τ_S. The expressions for the decay times τ_1 and τ_2 are given in Equations 3.8 and 3.9.[65]

$$\frac{d[E^*]}{dt} = k_1[Py][Py^*] - \left(k_{-1} + 1/\tau_E\right)[E^*] \tag{3.4}$$

$$\frac{d[Py^*]}{dt} = -\left(k_1[Py] + 1/\tau_M\right)[Py^*] + k_{-1}[E^*] \tag{3.5}$$

$$[E^*] = \frac{k_1[Py^*_{diff}]_o}{\sqrt{(X-Y)^2 + 4k_1k_{-1}}}\left[-\exp(-t/\tau_1) + \exp(-t/\tau_2)\right] + [Py^*_S]_o \exp(-t/\tau_S) \quad (3.6)$$

$$[Py^*] = \frac{[Py^*_{diff}]_o}{\sqrt{(X-Y)^2 + 4k_1k_{-1}}}\left[\left(X - \tau_2^{-1}\right) \times \exp(-t/\tau_1) - (X - \tau_1^{-1}) \times \exp(-t/\tau_2)\right]$$

$$+ [Py^*_{free}]_o \exp(-t/\tau_M) + [Py^*_S]_o \exp(-t/\tau_S) \quad (3.7)$$

$$\tau_1^{-1} = \frac{X + Y + \sqrt{(X-Y)^2 + 4k_1k_{-1}}}{2} \quad (3.8)$$

$$\tau_2^{-1} = \frac{X + Y - \sqrt{(X-Y)^2 + 4k_1k_{-1}}}{2} \quad (3.9)$$

The time-resolved fluorescence decays for the pyrene monomer and excimer emissions are fitted according to Equations 3.6 and 3.7, and the $k_1[Py]$, k_{-1}, and τ_E values are optimized by least-squares analysis.

3.3. Experimental Procedures

Synthesis of 1-Pyrenylmethylacetamide (PyMeAA): In a dry Schlenk flask, 1-pyrenemethylamine hydrochloride (PMA·HCl) (0.5 g, 2 mmol) was dried under high vacuum for 3 hours, and then suspended in a solution of dichloromethane (40 mL) and triethylamine (10 mL, 0.07 mol) under N_2 atmosphere. The vessel was cooled over dry ice and acetyl chloride (1.5 mL,

0.02 mol) was added drop-wise. The reaction was then removed from the dry ice and stirred at room temperature for 16 hours. The solution obtained was washed successively with 20 mL aliquots of HCl (0.05 N), $NaHCO_3$ (saturated), NaCl (saturated), and water. The organic phase was filtered by suction to remove the solid precipitate, dried over anhydrous sodium sulfate, and evaporated under vacuum. The crude product was recrystallized in dichloromethane and recovered by suction filtration (0.06 g, 0.3 mmol, 15% yield). 300 MHz ^{1}H NMR ($CDCl_3$): δ 2.0 (s, 3H), 5.1 (d, 2H), 5.8 (broad, 1H, NH), 7.3-8.2 (several peaks, 9H). UV-Vis (in DMF): characteristic pyrene peaks at 344, 328, 314 nm.

Sample Preparation: Five solutions of PyMeAA with concentrations ranging between 5 and 13 mM were prepared in DMF and in DMSO. After degassing for a minimum of 35 minutes under a gentle flow of N_2 to remove oxygen, the fluorescence spectra and the fluorescence decays for the samples were recorded with the front-face geometry.

Steady-state Fluorescence: A Photon Technology International LS-100 instrument equipped with an Ushio UXL-75Xe Xenon arc lamp and a PTI 814 photomultiplier detection system was used to record the steady-state fluorescence spectra.

Time-resolved Fluorescence Decays: The samples were excited at 344 nm in an IBH 5000F time-resolved fluorometer equipped with a NanoLED having a maximum intensity at 333 nm. The decays were acquired at 375 and 510 nm for the pyrene monomer and excimer, respectively, using the Time-Correlated Single Photon Counting (TCSPC) technique. All decays were collected over 1024 channels with at least 20 000 counts at the peak maximum. Depending on the sample, a decay acquisition time per channel of either 1.02 or 2.04 ns/channel was used with a repetition rate of 1 MHz or 500 kHz, respectively. Cut-off filters of 370 and 490 nm were

used to block potential light scattering leakage through the detection system for acquisition of the pyrene monomer and excimer fluorescence decays, respectively.

3.4. Results and Discussion

Excimer formation was much more efficient for 1-pyrenemethylacetamide (PyMeAA) in DMF than in DMSO, as implied by the normalized steady-state fluorescence spectra shown in Figure 3.4. This difference is partly due to the higher viscosity of DMSO (η = 2.0 mPa·s) than DMF (η = 0.79 mPa·s) at 25 ^{o}C, which hinders the diffusion of pyrene and reduces excimer formation. The lifetime (τ_M) for PyMeAA in DMF (200 ns) is larger than in DMSO (170 ns) and leads to a larger amount of excimer formation according to Equation 3.1. To account for the differences in viscosity and lifetime, $\eta \times \tau_M^{-1} \times (I_E/I_M)$ was plotted as a function of PyMeAA concentration in Figure 3.5. Even after this correction, the slope of the straight line for excimer formation in DMSO is still 27% greater than in DMF. This could either be due to the probability, *p* (see Equation 3.2), of forming an excimer upon collision being higher, or to the ratio ϕ_E^o / ϕ_M^o in Equation 3.1 taking different values in DMSO and DMF. Data analysis based on other rate constants is more straightforward, as it does not involve the parameters τ_M, ϕ_E^o, and ϕ_M^o. The rate constants can be determined directly from the analysis of the fluorescence decays according to the Birks scheme.

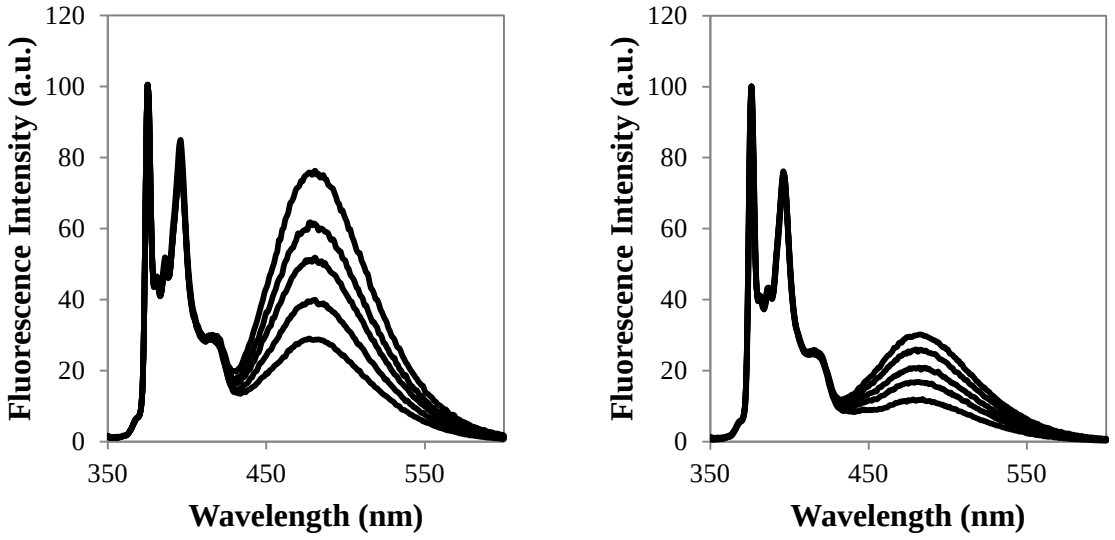

Figure 3.4: Steady-state fluorescence spectra for 1-pyrenemethylacetamide in DMF (left) and in DMSO (right). The concentrations are 13, 11, 9, 7, and 5 mM from top to bottom; λ_{ex}= 344 nm.

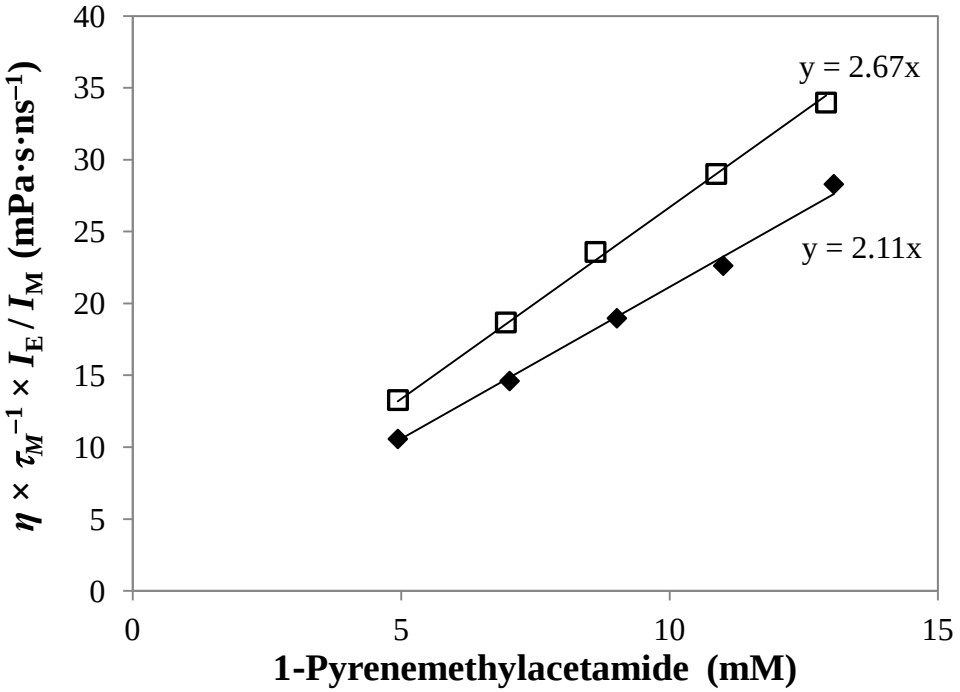

Figure 3.5: Excimer formation in concentrated solutions of 1-pyrenemethylacetamide in DMF (◆) and DMSO (□).

The fluorescence decays for the pyrene solutions, whose spectra are shown in Figure 3.4, were acquired and analyzed according to the Birks scheme to yield the $k_1[Py]$, k_{-1}, and τ_E values listed in Tables C1 and C2 in the Appendix. The data demonstrate that k_{-1} increases for decreasing pyrene concentrations, implying that the Birks scheme is capable of retrieving relevant parameters only at high pyrene concentrations, when there is sufficient excimer formation. The product $\eta \times k_1 \times [Py]$ plotted in Figure 3.6 increases linearly for increasing PyMeAA concentrations. The slopes of the lines in Figure 3.6 yield $\eta \times k_1$ values of 0.12 and 0.20 mPa·s·ns^{-1} in DMF and in DMSO, respectively. The product $\eta \times k_1$ is therefore 67% larger in DMSO than in DMF. The difference likely resides in the probability of forming an excimer, p in Equation 3.2, which must be larger in DMSO than in DMF, as inferred from the steady-state fluorescence analysis, rather than differences in the ϕ_E^o / ϕ_M^o ratio, since time-resolved fluorescence measurements used to calculate $k_1 \times [Py]$ are not affected by the quantum yield of the excimer and monomer species.

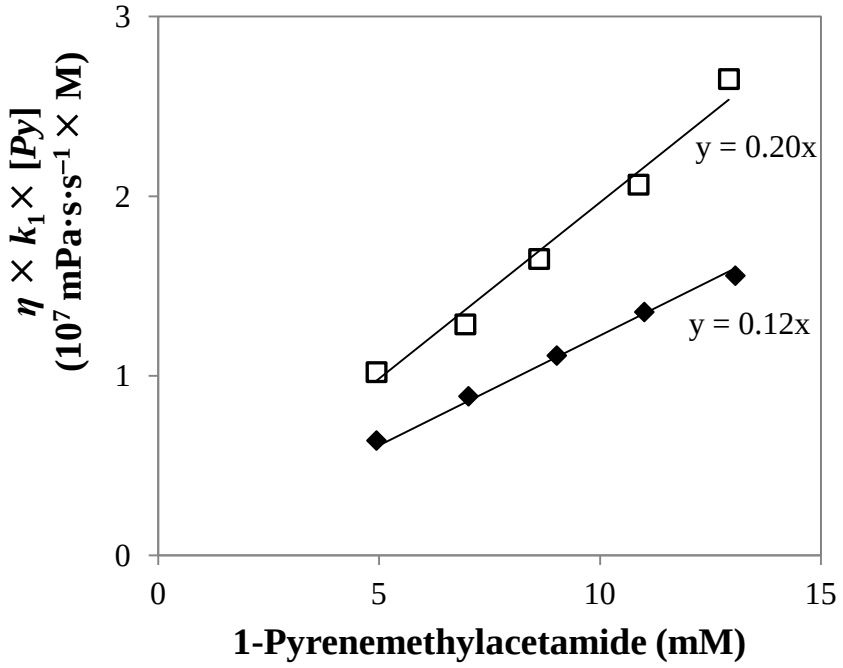

Figure 3.6: Rate constant for excimer formation, retrieved from Birks' Scheme analysis of 1-pyrenemethylacetamide solutions in DMF (◆) and in DMSO (□).

3.5. Conclusions

To determine the suitability of DMF and DMSO as solvents for fluorescence measurements, the formation of excimer by PyMeAA was characterized by monitoring the variation in I_E/I_M and $k_1 \times [Py]$ as a function of concentration. DMSO was found to hinder excimer formation to some extent, since it is more viscous than DMF and PyMeAA has a smaller τ_M in DMSO than in DMF. Accounting for variations in lifetime and viscosity with the quantities $\eta \times \tau_M^{-1} \times I_E/I_M$ and $\eta \times k_1 \times [Py]$ led to the conclusion that encounters between two pyrenes in DMSO is more likely to result in excimer formation due to a larger *p*-value, and a larger ϕ_E^o / ϕ_M^o ratio. Interestingly, the different *p*-values seem to have a much more noticeable effect when dealing with molecular

pyrene, as shown in Figures 3.5 and 3.6, than with pyrene-labelled macromolecules, since several reports indicate that the rate constant of excimer formation by diffusion for pyrene-labelled macromolecules is inversely proportional to the solvent viscosity.[66–68] The reason for this discrepancy resides in the slow internal dynamics of pyrene-labelled macromolecules. Encounters between two pyrene labels occur on such a slow timescale that they result in excimer formation with the same efficiency, regardless of differences in *p*-values. These observations ensure that the internal dynamics of PGA in DMF and in DMSO can be studied in the following chapter, by probing excimer formation between pyrene pendants covalently attached onto different PGA constructs.

4. Internal Dynamics of Arborescent PGA Probed by Excimer Formation

4.1. Introduction

There has been extensive theoretical and experimental work on dendritic polymers and the effect that their crowded interior has on the dynamics of the chain ends as a function of generation number.[33] Dendrimers are generally viewed as dense structures possessing a large number of reactive chain ends that can be modified with drugs, contrast agents for imaging, chromophores for light harvesting, or electron donating groups for electron transfer measurements. Arborescent polymers, with a branched structure generated by successive attachment of linear side chains onto a polymeric core (Scheme 1.1), constitute a unique class of macromolecules having a side-chain density in the outer periphery increasing for successive grafting cycles. While fluorescence quenching experiments have been instrumental in describing the internal dynamics of linear polymer chains, there have been a limited number of studies to date that characterize the internal dynamics of arborescent polymers. Linear, comb-branched, and arborescent polymers based on poly(L-glutamic acid) (PGA) are particularly interesting since it was shown in Chapter 2 that their side-chains adopt α-helical and random coil conformations in *N*,*N*-dimethylformamide (DMF) and in dimethyl sulfoxide (DMSO), respectively, making them representative mimics of globular proteins.

This chapter describes the synthetic protocol applied to covalently attach 1-pyrenemethylamine (PMA) to PGA, presents fluorescence results showing the time scale over which 1-pyrenemethylglutamide units encounter, and provides information about the relationship that exists between the structure and internal dynamics of these protein analogues in solution.

4.2. Experimental Procedures

4.2.1. Synthesis

Covalent attachment of 1-pyrenemethylamine (PMA) to the poly(L-glutamic acid) constructs was performed by using carbodiimide coupling as outlined in Scheme 4.1.

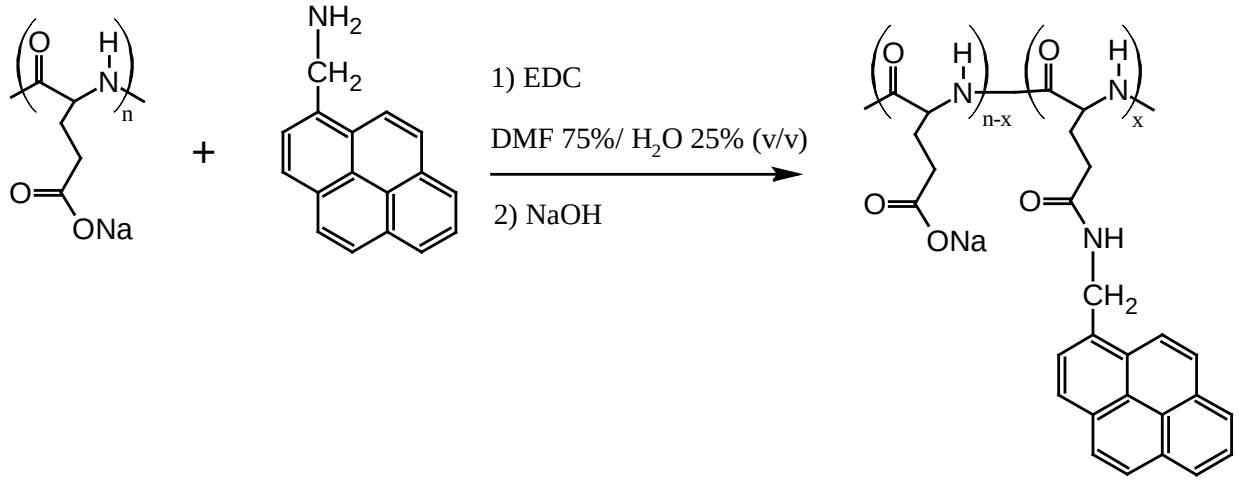

Scheme 4.1: Labelling reaction of poly(L-glutamic acid) sodium salt with PMA.

Prior to use, 1-pyrenemethylamine hydrochloride (0.5 g) was neutralized with 50 mL of 1 N NH_4OH aqueous solution. The resulting PMA was extracted into hexane (6 × 50 mL washes), dehydrated over NaOH pellets (0.5 g), and finally dried under vacuum.

Coupling of PMA with PGNa: As an example of a labelling reaction, G3 PGNa (11.3 mg, 7.5×10^{-4} mol glutamate units) was dissolved in 0.5 mL of water, followed by PMA (1.77 mg, 7.6×10^{-6} mol), and the drop-wise addition of 2.5 mL of dry DMF. After stirring for 10 min *N*-(3-dimethylaminopropyl)-*N*′-ethylcarbodiimide hydrochloride (EDC) (1.67 mg, 8.7×10^{-6} mol, or 1.2 molar equivalents with respect to PMA) was added. After 5 hours the solution was

acidified with 0.2 mL of 1 M HCl, and the solvent was evaporated under a stream of air. The residue was dissolved in 4 mL of 1 M NaOH and unreacted pyrene was removed by liquid-liquid extraction using hexane aliquots (7 × 4 mL). The aqueous solution was transferred to a 1000 MW cut-off dialysis bag which was immersed in 200 mL of methanol, to further remove any unreacted pyrene. After 15 hours the bag was transferred to 1 L of water (Milli Q doubly distilled). After changing the water bath 4 times within 8 hours, the content of the dialysis bag was emptied to a vial and the water was removed by freeze drying on a Labconco Freezone 6 apparatus. The product, Py-G3 PGNa (7.2 mg), was obtained as a white solid with 6.6% of the structural units labelled.

Acidification and Pyrene Content Determination: Determination of the pyrene content of the labelled poly(L-glutamic acid) (Py-PGA) samples was achieved using the Beer-Lambert law shown in Equation 4.1, where [*Py*] is the pyrene molar concentration, *A* is the absorption at 344 nm of a Py-PGA solution in DMF, *l* is the cell path length, and ε is the molar extinction coefficient of 1-pyrenylmethylacetamide in DMF (ε = 39,000 $mol^{-1} \cdot L \cdot cm^{-1}$). The sample was prepared by acidifying a known mass (*m*) of Py-PGNa and recovering Py-PGA by lyophilisation. The pyrene content, λ_{Py}, expressed in moles of pyrene per gram of PGA, was obtained by applying Equation 4.2 where *V* is the volume of DMF used to dissolve a sample of mass *m*. Converting the pyrene content to a mole fraction of labelled glutamate units was achieved using Equation 4.3, where M_{Py} (340 g/mol) and M_{PGNa} (151 g/mol) are the molar mass of the 1-pyrenemethylglutamide and the sodium glutamate structural units, respectively.

$$A = \varepsilon l [Py] \tag{4.1}$$

$$\lambda_{Py} = \frac{[Py]}{\frac{m}{V}} \tag{4.2}$$

$$mol\% = \frac{M_{PGNa}}{M_{PGNa} - M_{Py} + \frac{1}{\lambda_{Py}}} \tag{4.3}$$

In a specific case given as an example of the procedure applied, Py-G3 PGNa (2.31 mg) was converted to Py-G3 PGA by dissolution in 5 mL of water and the addition of HCl (0.8 mL, 1 N) drop-wise with stirring to induce the precipitation of Py-G3 PGA. The acidified solution was lyophilized to yield a coarse white powder. The residue was dissolved in DMF (3.28 g) and a portion of this solution (0.517 g) was further diluted with DMF (4.41 g) such that the resulting absorbance at 344 nm was 1.16 O.D. A pyrene content corresponding to λ_{Py}= 414 μmol·g^{-1} or 6.6 mol% was obtained, and the sample was assigned the label 6.6-G3. The Py-PGA sample nomenclature, seen in this Chapter and in the Appendix, specifies the pyrene content, in mol %, and the generation number of the PGA construct.

4.2.2. Instruments

Mass Balance: A Mettler Toledo XS Dual Range balance with 0.01 mg readability was used to measure sample masses lower than 5 mg precisely.

Gel Permeation Chromatography (GPC): The absence of free (non-bound) PMA contaminant in the pyrene-labelled samples was verified with a Waters GPC instrument consisting of a Waters 501 HPLC pump, a Jordi H2O X-stream MB (LS) 250 mm × 10 mm linear column, and an Agilent 1100 Series fluorescence detector, using DMF as eluent at a flow rate of 1 mL/min at room temperature. The Py-PGA sample solutions were prepared with a pyrene concentration of 2.5×10^{-6} M.

UV-Visible Spectrophotometry: UV-Vis absorption measurements were carried out on a Varian Cary 100 Bio spectrophotometer and were baseline-corrected. Solutions with an absorbance between 0.8 and 1.3 O.D. at 344 nm (pyrene absorption maximum) were prepared to ensure accurate absorbance measurements.

Fluorometry: The same instruments described in Chapter 3 were used with the right-angle detection geometry.

4.3. Analysis Methods

4.3.1. Absorption Spectroscopy

The peak-to-valley absorbance ratio, P_A, was obtained by taking the ratio of the absorbance for a Py-PGA solution at 344 nm over that of the adjacent trough in the UV-Vis absorption spectrum, as shown in Figure 4.1. This parameter gives a measure of peak broadening resulting from possible pre-association of the pyrene moieties along the polymer chain, due to the covalent

attachment of pyrene labels on glutamic acid units in close proximity. A P_A value of 3.0 indicates the absence of pyrene pre-association, while it decreases to lower values with increasing pyrene association.[69]

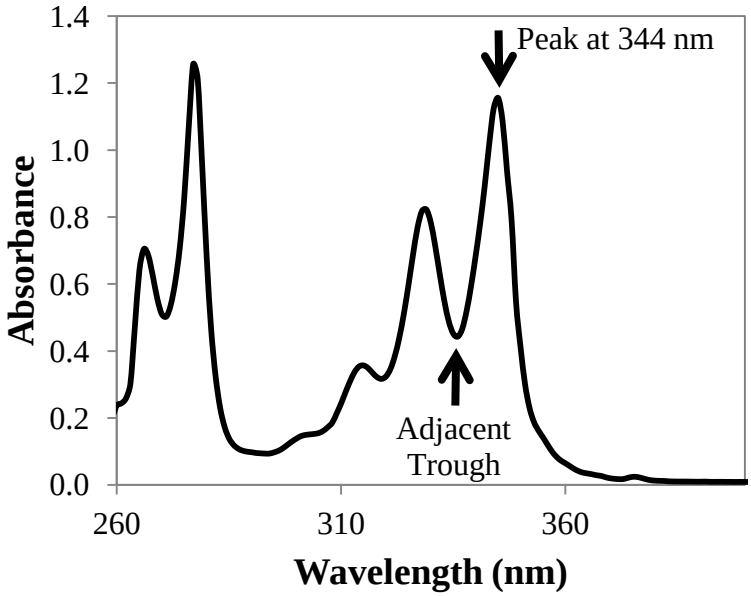

Figure 4.1: UV-Vis absorption spectrum for 6.6-G3 arborescent PGA in DMF, with P_A= 2.61

4.3.2. Emission Spectroscopy

Fluorescence decays were acquired for the Py-PGA solutions and fitted with a sum of exponentials, $g(t)$, according to Equation 4.4 with n varying between 2 and 4. In Equation 4.4, the parameters A_i represent the pre-exponential factors and τ_i are the corresponding decay times.

$$g(t) = \sum_{i=1}^{n} A_i e^{-t/\tau_i} \qquad (4.4)$$

The parameters of the function $g(t)$ were optimized by least-squares analysis and χ^2 was used to determine the appropriateness of the fit, a value of 1.00 being expected for a perfect fit. Other criteria for the goodness of the fit included a random distribution of the residuals and the autocorrelation function of the residuals around zero. Typical decay profiles along with the residuals and autocorrelation function of the residuals are shown in Figure 4.2.

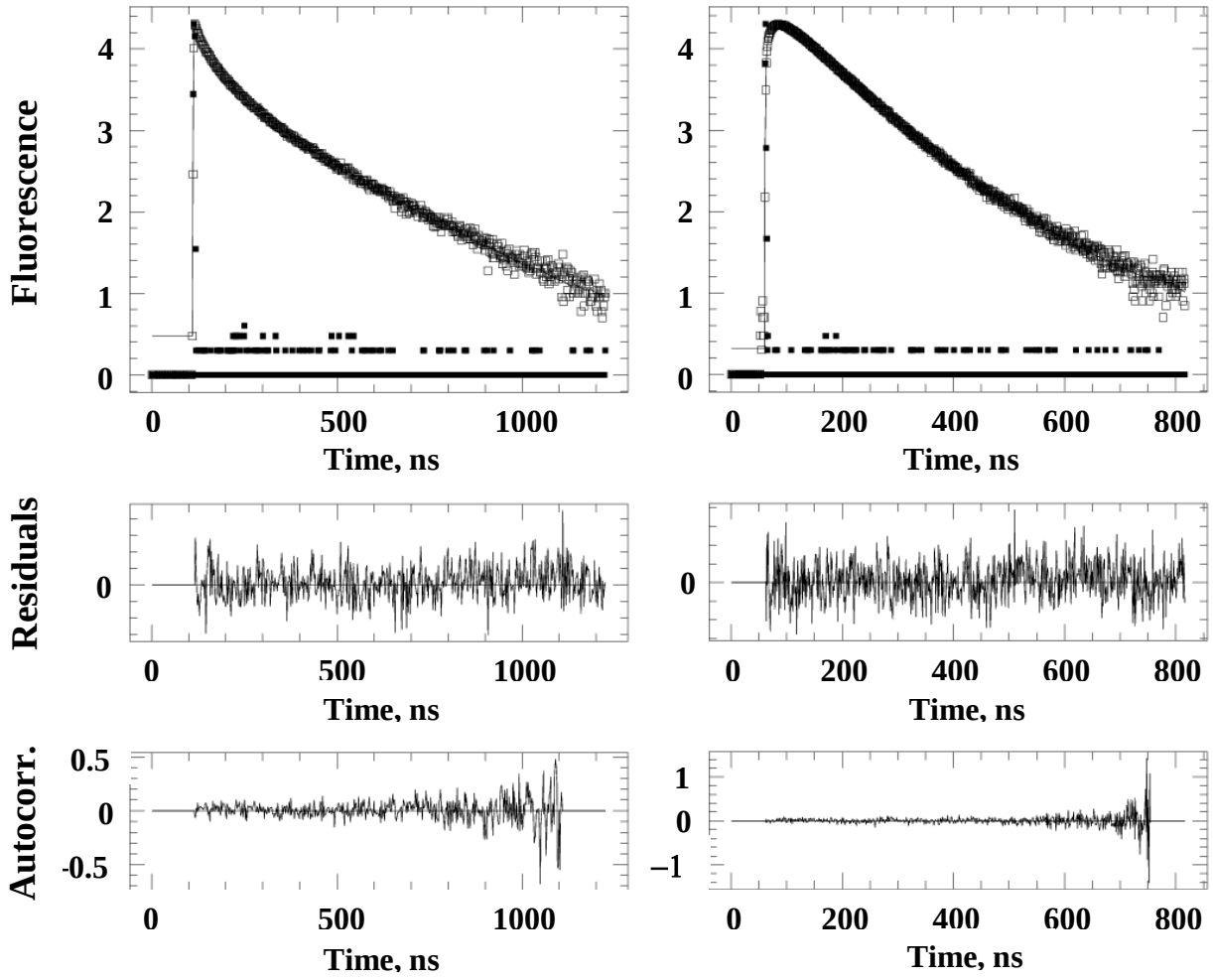

Figure 4.2: Time-resolved fluorescence decays for 6.6-G3 arborescent PGA in DMF [*Py*] = 2.5 × 10^{-6} M. Monomer emission (left; λ_{ex}= 344 nm, λ_{em}= 375 nm, time per channel = 2.04 ns, χ^2=1.07). Excimer emission (right; λ_{ex}= 344 nm, λ_{em}= 510 nm, time per channel = 1.02 ns, χ^2=1.10).

The A_{E-}/A_{E+} ratio is a measure of the degree of pyrene association along the polymer backbone. It is the ratio of the sum of the negative pre-exponential factors over the sum of the positive pre-exponential factors in Equation 4.4, obtained from the analysis of the excimer decays. An A_{E-}/A_{E+} ratio approaching −1.0 is typical of polymer samples showing no pyrene pre-association, while a value that is more positive indicates that some pre-association is present.

4.3.3. Fluorescence Blob Model

The intramolecular chain dynamics can be investigated through the analysis of time-resolved fluorescence decays for dilute solutions of polymers labelled with pyrene. The Birks scheme analysis of fluorescence decays was introduced in the late 1970's to describe the end-to-end cyclization of pyrene end-labelled monodispersed polystyrene chains of low molecular weight.[70] In 1993, the Fluorescence Blob Model (FBM) was introduced to analyze the fluorescence decays of high molecular weight polymers randomly labelled with fluorescent probes.[71,72] To date, the FBM remains the sole analytical tool in the scientific literature capable of providing quantitative information on the internal dynamics of macromolecules randomly labelled with pyrene. The terms and concepts associated with the process of excimer formation for randomly labelled polymers are slightly different from those introduced in Birks' scheme (Scheme 3.1) used for homogeneous solutions. After excitation by a photon of light ($h\nu$), an excited pyrene may proceed towards pyrene excimer formation according to Scheme 4.2. The function $f(t)$ describes the slow diffusion of internal segments of the chain that brings an excited pyrene (Py^{*}_{diff}) close to a ground-state pyrene (Py). The process of excimer formation in randomly labelled polymers is described by an infinite number of rate constants resulting from the distribution of distances

separating any two pyrenes along the chain.[72] This distribution of rate constants explains why the overall rate "constant" for excimer formation, *f(t)*, depends on time. Rapid rearrangement of the pyrene pendants to form an excimer takes place with a rate constant k_2. $Py^*_{k_2}$ represents those pyrene pendants that form excimer in this manner. The lifetimes τ_M, τ_{EO}, and τ_D are for the pyrene monomer (*M**), short- (*E0**) and long- (*D**) lived excimer species, respectively. The existence of these long- and short-lived excimers is attributed to difficulties for two pyrene pendants to adopt the proper stacking to form an excimer, due to the steric constraints of covalent attachment and molecular crowding of the interior of the macromolecule.

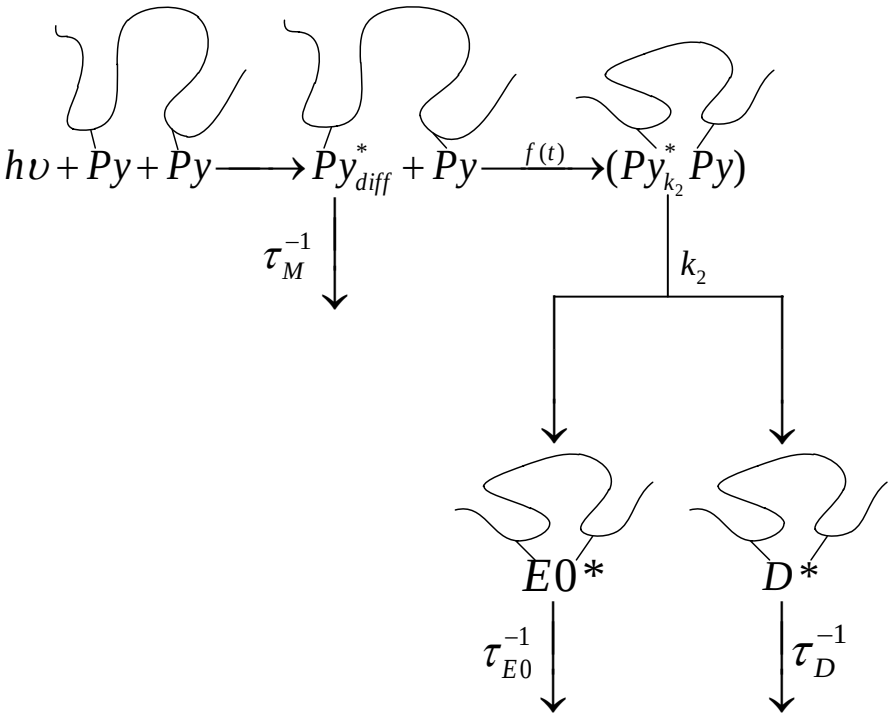

Scheme 4.2: Photophysical pathways for the formation of excimer by pyrene labels randomly attached to a polymer.

Excimer formation can also occur via direct absorption of a photon by two pre-associated pyrenes without involving a chain diffusion process. The mole fraction of aggregated pyrene pendants, f_{agg}, identifies these pre-associated ground-state pyrene moieties in a much more quantitative manner than the P_A and A_{E-}/A_{E+} values. It should also be pointed out that Scheme 4.2 does not include reverse reactions such as excimer dissociation, whose rate constant has been found to be negligibly small in several studies conducted with pyrene end-labelled polymers at room temperature.[18,65,70]

Polymers randomly labelled with pyrene may contain pyrene-poor domains, where an excited pyrene is isolated from the other pyrenes in the macromolecule and does not have the opportunity to form an excimer during its lifetime. These isolated labels emit with the unquenched lifetime τ_M of the pyrene monomer, and within the FBM are referred to as Py^*_{free}. For those pyrene labels that do form excimer, the FBM is a convenient way to account for the random distribution of pyrenes and provides a means to calculate *f(t)*. The analysis relies on the principle that a polymer chain may be subdivided into finite volumes of space known as *blobs*, defined by the volume that may be probed by an excited species, Py^*_{diff}, during its natural lifetime before fluorescence emission occurs. The size of a *blob* is defined in terms of segments having an average length N_{blob}, corresponding to the number of structural units along the polymer chain that are contained in a *blob*. The concentration of *blobs* within a polymer coil is referred to as [*blob*]. The slow internal dynamics experienced within the crowded interior of an arborescent PGA molecule should bring the 1-pyrenemethylglutamide units close to each other with a rate constant k_{blob}, with excimer formation resulting from the rapid rearrangement of the pyrene labels with a rate constant k_2.

Equation 4.5 is used to calculate the value of N_{blob}, where M_{Py} (340 g/mol) and M_{PGA} (129 g/mol) are respectively the molar masses of a 1-pyrenemethylglutamamide unit and a glutamic acid unit, f_{Mfree} is the mole fraction of pyrene labels contributing to the monomer decays (i.e. which do not form excimer), x is the mole fraction of pyrene-labelled glutamic acid units in the polymer sample, and $<n>$ represents the average number of ground-state pyrenes per *blob*, retrieved from FBM analysis of the fluorescence decays. The term $\lambda_{\text{py}} \cdot (1 - f_{\text{Mfree}})^{-1}$ is the corrected pyrene concentration and accounts for the larger λ_{py} value of the subdomains of the pyrene-labelled macromolecule that are pyrene-rich and form excimer.

$$N_{blob} = \frac{< n >}{\left[\frac{\lambda_{Py}}{1 - f_{Mfree}}\right] \times \left[M_{Py}(x) + M_{PGA}(1 - x)\right]} \tag{4.5}$$

The fluorescence decays obtained for the pyrene-labelled macromolecules are fitted according to the FBM using Equations 4.6 and 4.7, which describe the concentration of excited pyrene monomer and excimer species as a function of time. The values of the parameters describing the kinetics of pyrene excimer formation are determined by least-squares analysis of the fluorescence decays. The parameters A_2, A_3, and A_4 used in Equations 4.6 and 4.7 are defined by Equations 4.8-4.10, where $<n>$ is the number of ground-state pyrenes per *blob*, k_{blob} is the rate constant describing excimer formation within a *blob*, and k_e is the rate constant for the transfer of ground-state pyrenes between *blobs*. The diffusion of pyrene moieties in and out of a *blob* is described by the product $k_e \times [blob]$.

$$[Py^*]_{(t)} = [Py^*_{diff}]_{(t)} + [Py^*_{k2}]_{(t)} + [Py^*_{free}]_{(t)} = [Py_{diff}]_o \exp\left(-\left(A_2 + \frac{1}{\tau_M}\right)t - A_3\left(1-\exp(-A_4 t)\right)\right)$$

$$+\left([Py_{k2}]_o + [Py_{diff}]_o e^{-A_3}\sum_{i=0}^{\infty}\frac{A_3^i}{i!}\frac{A_2+iA_4}{A_2+iA_4-k_2}\right)\exp\left(-\left(k_2+\frac{1}{\tau_M}\right)t\right)$$

$$-[Py_{diff}]_o e^{-A_3}\sum_{i=0}^{\infty}\frac{A_3^i}{i!}\frac{A_2+iA_4}{A_2+iA_4-k_2}\exp\left(-\left(A_2+iA_4+\frac{1}{\tau_M}\right)t\right)$$

$$+[Py_{free}]_o \exp\left(-\frac{t}{\tau_M}\right)\Bigg] \qquad (4.6)$$

$$[E^*]_{(t)} = [E0^*]_{(t)} + [D^*]_{(t)} = k_2\Bigg(\left([Py_{k2}]_o + [Py_{diff}]_o e^{-A_3}\sum_{i=0}^{\infty}\frac{A_3^i}{i!}\frac{A_2+iA_4}{A_2+iA_4-k_2}\right)$$

$$\times\frac{\exp\left(-\frac{t}{\tau_{E0}}\right)-\exp\left(-\left(k_2+\frac{1}{\tau_M}\right)t\right)}{k_2+\frac{1}{\tau_M}-\frac{1}{\tau_{E0}}}$$

$$+[Py_{diff}]_o e^{-A_3}\sum_{i=0}^{\infty}\frac{A_3^i}{i!}\frac{A_2+iA_4}{A_2+iA_4-k_2}\frac{\exp\left(-\left(A_2+iA_4+\frac{1}{\tau_M}\right)t\right)-\exp\left(-\frac{t}{\tau_{E0}}\right)}{A_2+iA_4+\frac{1}{\tau_M}-\frac{1}{\tau_{E0}}}\Bigg)$$

$$+[E0]_o\times\exp\left(-\frac{t}{\tau_{E0}}\right)+[D]_o\times\exp\left(-\frac{t}{\tau_D}\right)\Bigg] \qquad (4.7)$$

$$A_2 = < n > \frac{k_{blob} k_e [blob]}{k_{blob} + k_e [blob]} \tag{4.8}$$

$$A_3 = < n > \frac{(k_{blob})^2}{(k_{blob} + k_e [blob])^2} \tag{4.9}$$

$$A_4 = k_{blob} + k_e [blob] \tag{4.10}$$

Within the FBM framework, k_{blob} is the product of the bimolecular rate constant for excimer formation, k_{diff}, times the inverse of the *blob* volume, V_{blob}. Consequently, the product $k_{blob} \times N_{blob}$ is the product of k_{diff} and the local *blob* density of the macromolecule, i.e. N_{blob}/V_{blob}.

Similarly to the sum of exponentials analysis discussed in Section 4.3.2, the goodness of fit according to the FBM analysis of the fluorescence decays is determined by the deviation of χ^2 from unity and the random distribution of the residuals and the autocorrelation function of the residuals as shown in Figure 4.3.

The fluorescence decays obtained for each of the pyrene-labelled PGA samples were analyzed twice with the FBM equations. In the first analysis, the rate constant for the rapid rearrangement of the pyrene labels, k_2, was optimized. In the second analysis k_2 was set to its average value, $<k_2>$, in order to reduce the variability in the remaining parameters obtained from the optimization.

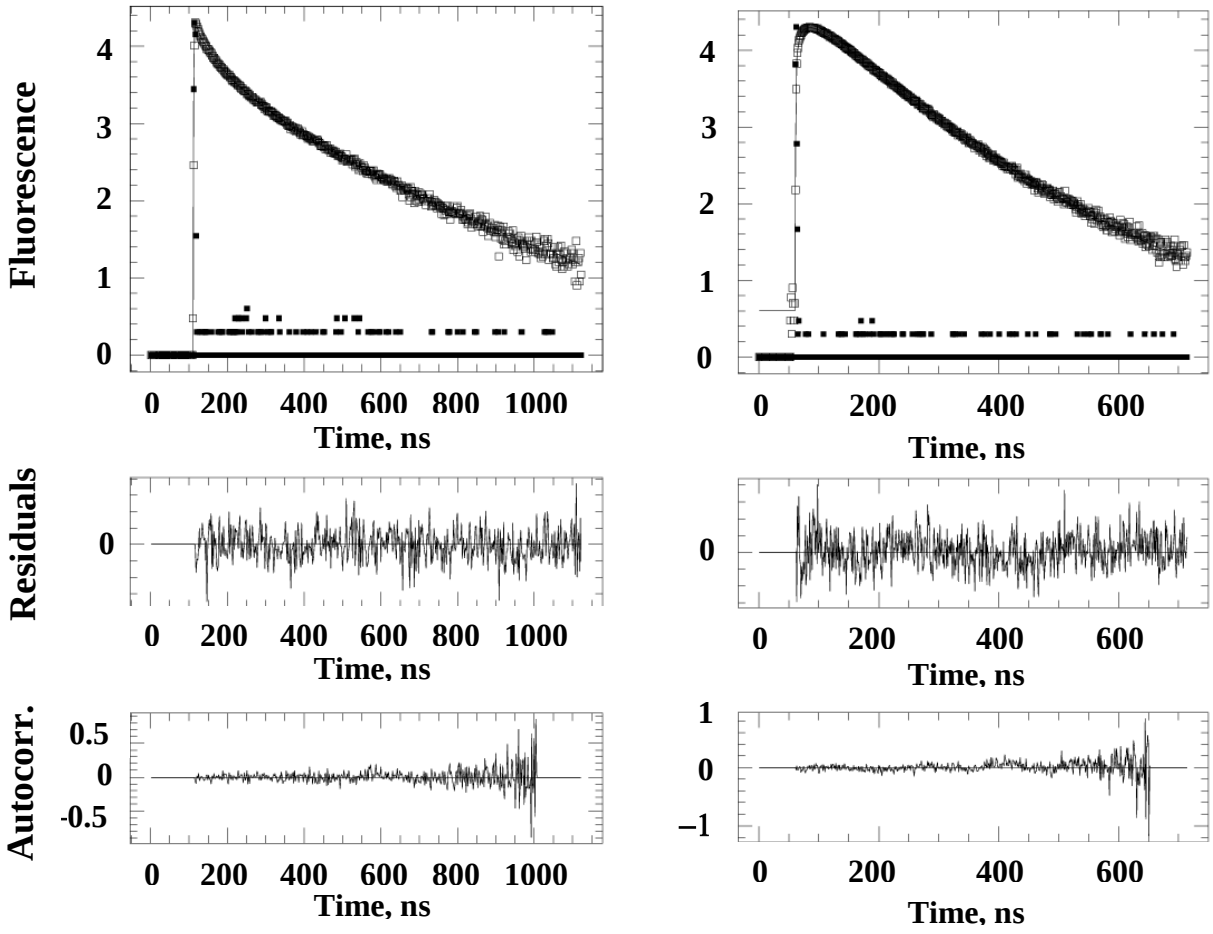

Figure 4.3: Monomer (λ_{em}= 375 nm, left) and excimer (λ_{em}= 510 nm, right) decays for 6.6-G3 arborescent PGA in DMF analyzed by the Fluorescence Blob Model; χ^2=1.14, λ_{ex} = 344 nm, $[Py]= 2.5 \times 10^{-6}$ M.

For the fitted decays, the parameters describing the fractions of pyrene species in solution, f_{diff}, f_{free}, f_{E0}, $f_{D,}$ f_{diff}^{E0}, and f_{diff}^{D} can be calculated from the fractions f_{Mdiff}, f_{Mfree}, f_{Mk_2}, f_{Ediff}^{E0}, f_{Ediff}^{D}, f_{EE0}, and f_{ED}, that were estimated from the FBM according to Equations 4.11-4.16. The indices "M", "E", "E0" and "D" serve as reminders that the fractions f_{Mdiff}, f_{Mfree}, and f_{Mk_2} describe the pyrene species that contribute to the monomer decays; the fractions f_{Ediff}^{E0}, f_{EE0}, and f_{E0} describe

the pyrene species with a lifetime τ_{E0}, that contribute to the excimer decays; and the fractions f_{Ediff}^{D}, f_{ED}, and f_{D} describe pyrene species with a lifetime τ_{D}, that contribute to the excimer decays. The molar fraction of aggregated pyrene, f_{agg}, is calculated according to Equation 4.17.

$$f_{diff}^{E0} = \frac{f_{Ediff}^{E0}}{f_{Ediff}^{E0} + f_{Ediff}^{D}} \left(1 + \frac{f_{Mfree} + f_{Mk_2}}{f_{Mdiff}} + \frac{f_{EE0} + f_{ED}}{f_{Ediff}^{E0} + f_{Ediff}^{D}} \right)^{-1} \tag{4.11}$$

$$f_{diff}^{D} = \frac{f_{Ediff}^{D}}{f_{Ediff}^{E0} + f_{Ediff}^{D}} \left(1 + \frac{f_{Mfree} + f_{Mk_2}}{f_{Mdiff}} + \frac{f_{EE0} + f_{ED}}{f_{Ediff}^{E0} + f_{Ediff}^{D}} \right)^{-1} \tag{4.12}$$

$$f_{free} = \left(f_{diff}^{E0} + f_{diff}^{D} \right) \frac{f_{Mfree}}{f_{Mdiff}} \tag{4.13}$$

$$f_{E0} = \left(f_{diff}^{E0} + f_{diff}^{D} \right) \frac{f_{EE0}}{f_{Ediff}^{E0} + f_{Ediff}^{D}} \tag{4.14}$$

$$f_{D} = \left(f_{diff}^{E0} + f_{diff}^{D} \right) \frac{f_{ED}}{f_{Ediff}^{E0} + f_{Ediff}^{D}} \tag{4.15}$$

$$f_{k_2} = \left(f_{diff}^{E0} + f_{diff}^{D} \right) \left(\frac{f_{Ek_2}}{f_{Ediff}^{E0} + f_{Ediff}^{D}} \right) \tag{4.16}$$

$$f_{agg} = f_{E0} + f_{D} \tag{4.17}$$

4.4. Results and Discussion

4.4.1. Pyrene-labelled Poly(L-glutamic acid)

A total of 41 Py-PGA samples were prepared with pyrene contents varying between 1 and 22 mol %. Tables 4.1 and 4.2 provide the pyrene content, P_A value, A_{E-} / A_{E+} ratio, and the molar fraction of aggregated pyrene (f_{agg}) for all these pyrene-labelled samples. The parameters used to calculate A_{E-} / A_{E+}, retrieved from the sum of exponential analysis, are presented in Tables F1-F20 in the Appendix.

Table 4.1: Pyrene content, P_A, A_{E-} / A_{E+} and f_{agg} for Py-linear and Py-G0 poly(L-glutamic acid).

Sample	Pyrene Content		P_A		A_{E-} / A_{E+}		f_{agg}	
	mol %	λ_{Py} (μmol·g^{-1})	DMF	DMSO	DMF	DMSO	DMF	DMSO
2.4-Lin	2.4	157	2.4	2.6	-0.83	-0.89	-	-
5.0-Lin	5.0	324	2.8	2.7	-0.90	-0.95	0.065	0.085
6.6-Lin	6.6	416	2.7	2.7	-0.91	-0.89	0.071	0.085
6.6-Lin	6.6	416	2.7	2.7	-0.90	-0.88	0.087	0.105
7.5-Lin	7.5	466	2.7	2.7	-0.92	-0.93	0.074	0.059
8.1-Lin	8.1	501	2.7	2.7	-0.91	-0.89	0.072	0.091
10-Lin	10.3	615	2.6	2.7	-0.92	-0.92	0.093	0.081
14-Lin	13.5	777	2.6	2.6	-0.92	-0.90	0.086	0.094
15-Lin	15.0	854	2.6	2.6	-0.89	-0.92	0.15	0.13
4.1-G0	4.1	265	2.7	2.7	-0.93	-0.90	0.019	0.096
6.6-G0	6.6	413	2.6	2.5	-0.90	-0.91	0.081	0.064
11-G0	11.0	653	2.6	2.6	-0.87	-0.91	0.12	0.08
13-G0	12.9	747	2.6	2.6	-0.90	-0.92	0.12	0.09
17-G0	16.7	924	2.6	2.5	-0.88	-0.92	0.21	0.10
22-G0	21.5	1127	2.4	2.5	-0.84	-0.88	0.25	0.24

Table 4.2: Pyrene content, P_A, A_{E-} / A_{E+} and f_{agg} for Py-G1, Py-G2 and Py-G3 arborescent PGA.

Label	Pyrene Content		P_A		A_{E-} / A_{E+}		f_{agg}	
	mol %	λ_{Py} ($\mu mol \cdot g^{-1}$)	DMF	DMSO	DMF	DMSO	DMF	DMSO
1.3-G1	1.3	83	2.6	2.5	-0.84	-0.77	-	-
5.9-G1	5.9	388	2.6	2.6	-0.86	-0.92	0.10	0.088
7.2-G1	7.2	474	2.5	2.6	-0.81	-0.90	0.14	0.089
12-G1	12.0	700	2.5	2.7	-0.86	-0.83	0.15	0.17
13-G1	13.4	773	2.5	2.6	-0.87	-0.89	0.14	0.14
17-G1	16.8	930	2.4	2.6	-0.86	-0.84	0.24	0.20
21-G1	21.4	1122	2.4	2.5	-0.84	-0.86	0.30	0.25
22-G1	22.3	1158	2.3	2.4	-0.83	-0.85	0.33	-
1.1-G2	1.1	72	2.5	2.5	-0.80	-0.90	-	-
4.3-G2	4.3	277	2.7	2.6	-0.87	-0.90	0.059	0.077
6.6-G2	6.6	413	2.6	2.6	-0.89	-0.90	0.093	0.083
8.7-G2	8.7	532	2.6	2.6	-0.89	-0.89	0.10	0.11
10-G2	10.2	612	2.6	2.6	-0.88	-0.87	0.13	0.13
14-G2	14.4	821	2.3	2.5	-0.83	-0.87	0.22	0.20
18-G2	18.0	984	2.2	2.4	-0.82	-0.79	0.32	0.23
2.5-G3	2.5	166	2.6	2.6	-0.95	-0.96	0.034	0.052
4.0-G3	4.0	258	2.4	2.6	-0.95	-0.95	0.036	0.054
5.4-G3	5.4	347	2.6	2.6	-0.91	-0.93	0.065	0.057
6.0-G3	6.0	377	2.6	2.6	-0.90	-0.93	0.071	0.053
6.6-G3	6.6	414	2.6	2.6	-0.90	-0.93	0.077	0.063
8.1-G3	8.1	497	2.6	2.5	-0.90	-0.93	0.092	0.072
9.4-G3	9.4	570	2.5	2.6	-0.89	-0.91	0.11	0.095
11-G3	10.9	652	2.5	2.6	-0.87	-0.88	0.16	0.15
11-G3	11.0	657	2.6	2.5	-0.90	-0.91	0.11	0.09
12-G3	11.4	674	2.4	2.4	-0.86	-0.86	0.23	0.18
13-G3	12.6	733	2.4	2.5	-0.85	-0.83	0.24	0.24

In Tables 4.1 and 4.2, the P_A ratios have an average value of 2.5 ± 0.1 regardless of the generation number, solvent-induced conformation, or pyrene content. This value is identical with that previously reported by Ingratta *et al*. for linear Py-PGA in DMF.[22] Since it is closer to 3.0 than 1.5 found for pyrene aggregates of pyrene-labelled poly(*N*,*N*-dimethylacrylamide) in water,[73] it indicates that pyrene is uniformly distributed along the polymer chains. Analysis of the excimer decays based on a sum of exponentials yielded similar A_{E-} / A_{E+} ratios in DMF and in DMSO despite the different conformations adopted by the PGA side-chains in each solvent. The A_{E-} / A_{E+} ratios were more negative than –0.80 in all but one case, again indicating little pyrene aggregation in these samples. The mole fraction of aggregated pyrenes, f_{agg}, obtained by FBM analysis of the fluorescence decays, was found to be more sensitive to the level of pyrene clustering than the P_A value and the A_{E-} / A_{E+} ratio. Although f_{agg} was low in most cases as expected for samples with little pyrene aggregation, an increase in pyrene content resulted in a significant increase in f_{agg}. For Py-G3 arborescent PGA in DMF, f_{agg} increased from 0.03 to 0.24 as λ_{py} was increased from 166 to 733 μmol/g. Since the ability of pyrene to probe polymer chain dynamics is diminished at such high levels of aggregation, samples with f_{agg} greater than 0.20 have been excluded from the analysis. In many cases, these samples have pyrene contents greater than 800 μmol/g or 14 mol %.

Gel permeation chromatography (GPC) analysis was used to verify the absence of unreacted (free) pyrene labels in the Py-PGA samples. Representative GPC traces acquired with the fluorescence detector are shown in Figure 4.4. In the bottom trace, 1-pyrenemethylamine was found to elute at 23 mL as expected for small molecules, and exhibited peak broadening due to adsorption on the column packing material. The top trace for a Py-PGA sample demonstrates that all unreacted pyrene labels were removed from the sample. In some instances the labelling

procedure and subsequent purification steps resulted in a mixture of products, possibly due to a degradation of the arborescent PGA molecules, with impurities eluting at different volumes, shown in the middle trace of Figure 4.4. These impure samples were discarded from this study. GPC traces for the purified Py-PGA samples are presented in Figures D1-D5 in the Appendix.

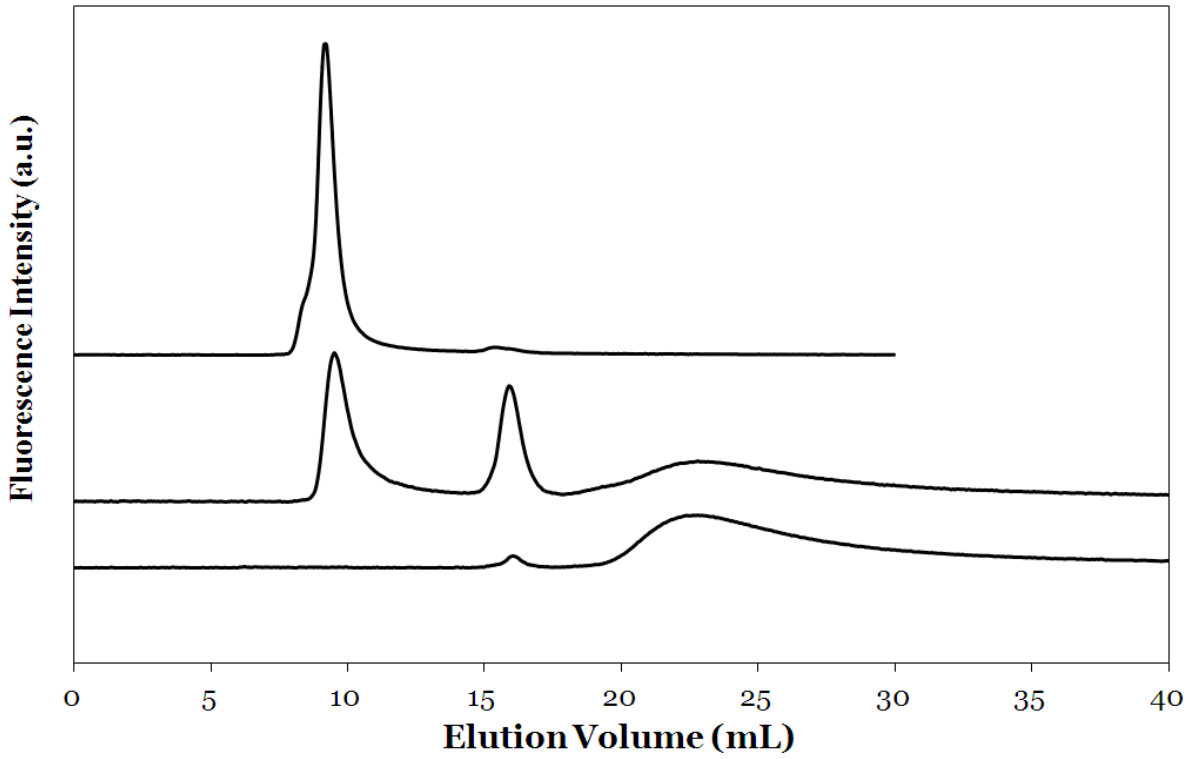

Figure 4.4: GPC traces monitored with a fluorescence detector (λ_{ex}= 344 nm, λ_{em}= 375 nm). From top to bottom: pure 15% Py-Lin PGA, [*Py*] = 2.5 × 10^{-6} M; 11.7% Py-Lin PGA with impurities, [*Py*] = 2.5 × 10^{-6} M; and 1-pyrenemethylamine [*Py*] = 5.0 × 10^{-7} M.

4.4.2. Steady State Fluorescence

Fluorescence spectra for the pyrene-labelled G3 arborescent poly(L-glutamic acid) (Py-G3 PGA) samples acquired in DMF and in DMSO are compared in Figure 4.5 after normalization to

the monomer peak at 375 nm. The excimer emission intensity centered at 480 nm increases as the pyrene content increases. Less excimer is formed in DMSO than in DMF. These differences are influenced by the internal dynamics of the macromolecules, the solvent viscosity, and the lifetime of the pyrene monomer, τ_M.

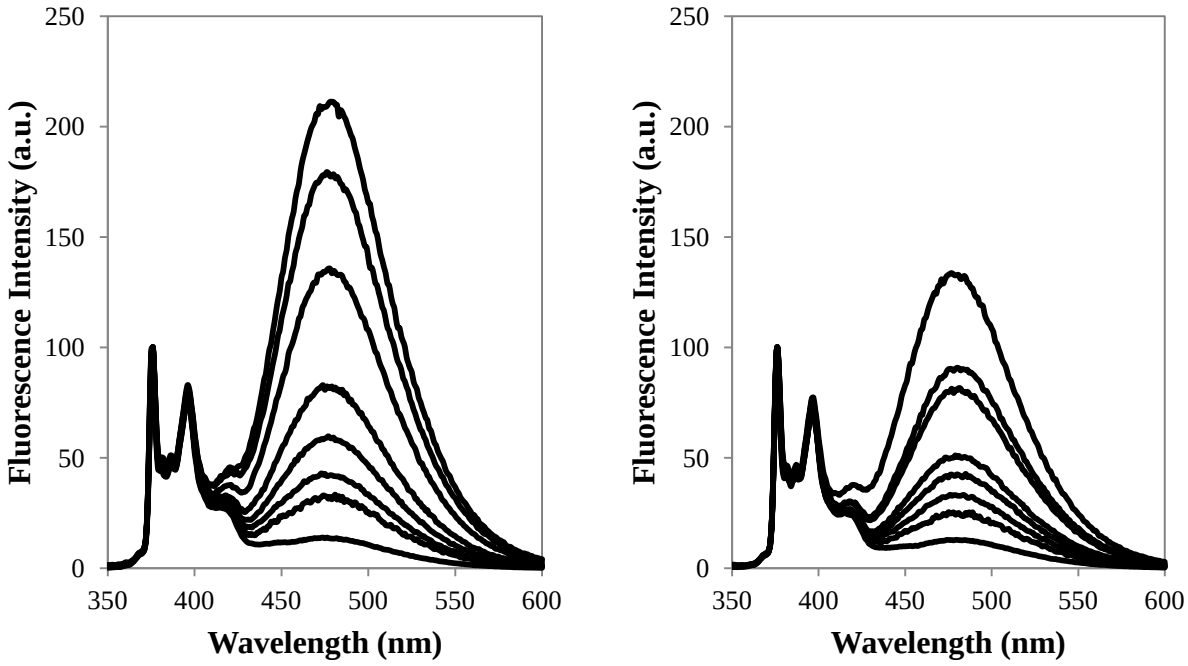

Figure 4.5: Steady-state fluorescence spectra for Py-G3 arborescent PGA in DMF (left) and in DMSO (right). The pyrene contents are 12.6, 11.4, 10.9, 9.4, 8.1, 6.6, 5.4, and 4.0 mol % (top to bottom).

The lifetime τ_M for pyrene-labelled PGA was determined to equal 208 ± 2 ns in DMF and 169 ± 1 ns in DMSO, using two linear polymer samples with pyrene contents below 1 mol%. These lifetimes are similar to the ones found for 1-pyrenemethylacetamide in DMF (200 ns) and in DMSO (170 ns). To account for the different lifetimes and the different solvent viscosities of

DMF (0.79 mPa·s) and DMSO (2.0 mPa·s) at 25 ^{o}C, the I_E/I_M ratios obtained from the fluorescence spectra were multiplied by the solvent viscosity and divided by τ_M. Figure 4.6 shows the product $\eta \times \tau_M^{-1} \times I_E/I_M$ for linear, G0, G1, G2, and G3 arborescent PGAs. For each PGA construct, $\eta \times \tau_M^{-1} \times I_E/I_M$ increases with increasing pyrene content, reflecting more efficient excimer formation with increased local pyrene concentration ($[Py]_{local}$). Furthermore, $\eta \times \tau_M^{-1} \times I_E/I_M$ for a given pyrene content increases according to the sequence linear < G0, G1 < G2 < G3, in agreement with the increased density and $[Py]_{local}$ of the polymer. This trend is more pronounced in DMSO than in DMF. Finally, $\eta \times \tau_M^{-1} \times I_E/I_M$ for a given construct is larger in DMSO than in DMF. Interestingly, the difference is more noticeable when dealing with pyrene-labelled PGA than with molecular pyrene, as shown in Figure 3.5, suggesting that the PGA constructs undergo faster dynamics in DMSO. This may be due to the change in conformation undergone by the PGA side-chains from α-helices in DMF to random coils in DMSO. It also indicates that the slow internal dynamics of pyrene-labelled macromolecules may have an effect on the likelihood of excimer formation, similarly to differences between the quantum yield and the probability of excimer formation discussed for PyMeAA in Chapter 3.

The $\eta \times \tau_M^{-1} \times I_E/I_M$ data shown for Py-G3 arborescent PGA in Figure 4.6 exclude the samples with λ_{Py} greater than 800 μmol/g, that had large I_E/I_M ratios. While the same trends applied to all the samples, the samples with pyrene contents above 800 μmol/g had high pyrene aggregation levels and resulted in highly efficient excimer formation. This interpretation is consistent with the f_{agg} values shown in Tables 4.1 and 4.2, and provides further evidence that samples with high pyrene labelling levels should be discarded from the analysis.

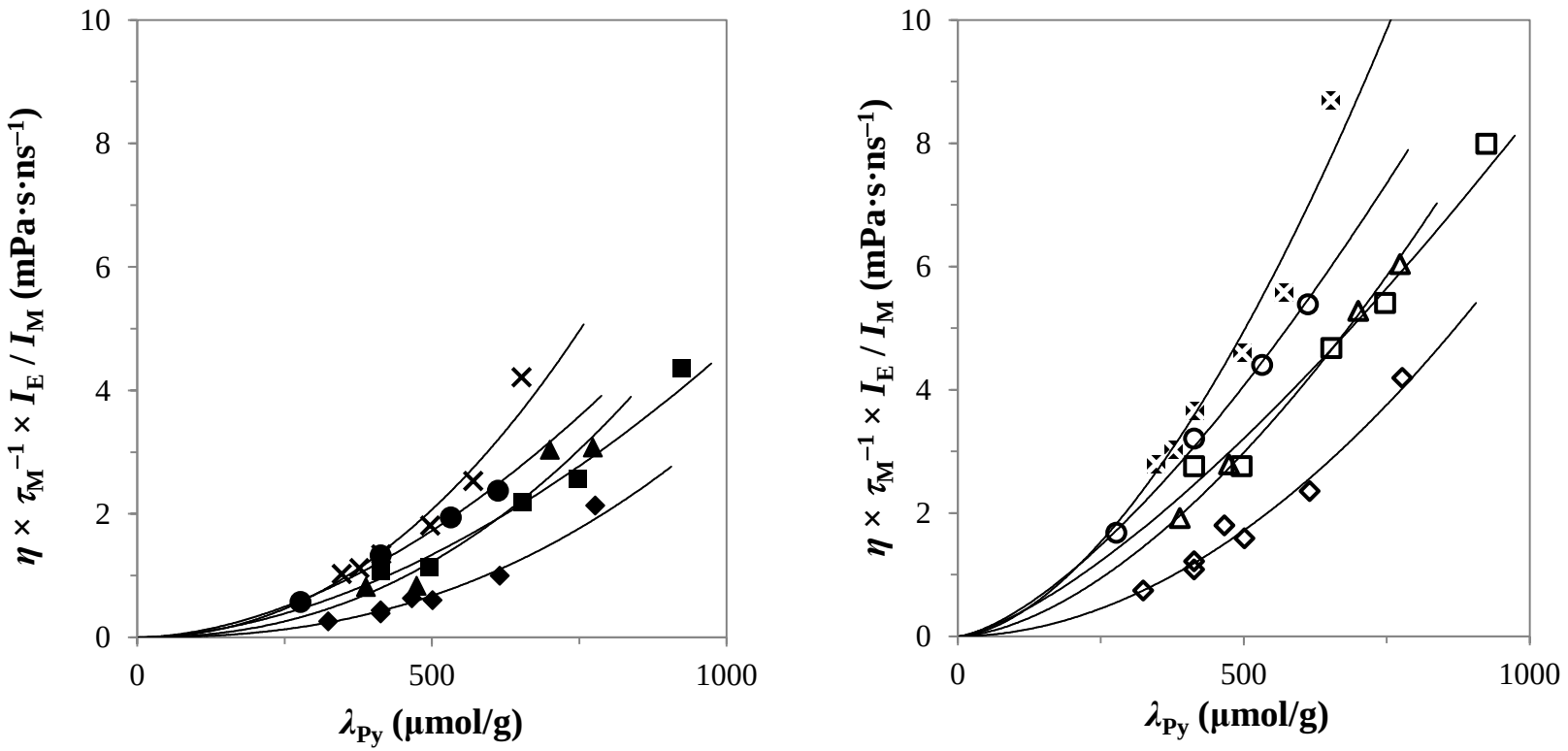

Figure 4.6: Plots of $\eta \times \tau_M^{-1} \times I_E/I_M$ versus pyrene content for linear (◆,◇), Py-G0 (■,□), Py-G1 (▲,△), Py-G2 (●,○), and Py-G3 (✕, ☒) PGA constructs in DMF (filled symbols) and DMSO (hollow symbols).

4.4.3. Time-resolved Fluorescence

The monomer and excimer emission decays for four Py-G3 arborescent PGA samples are provided in Figure 4.7. In the monomer decays, curvature at the early times is caused by quenching of the pyrene monomer through pyrene excimer formation. For 11-G3, the large pyrene content results in efficient excimer formation associated with a rapid decrease in the pyrene monomer concentration, followed by a mono-exponential decay at later times due to the emission of the longer-lived Py^{*}_{diff} and Py^{*}_{free} species. For 2.5-G3, little excimer is formed and the pyrene monomer fluorescence decay exhibits minimal curvature. While Py-PGA with pyrene contents below 1% were needed to determine the fluorescence lifetime τ_M via sum of exponential fitting of the decay, Py-PGA samples with insufficient excimer formation could not be fitted with the FBM equations since there was not enough curvature in the monomer decays.

The monomer emission decays display the same features observed for molecular pyrene distributed in surfactant micelles.[74,75] This supports the use of the FBM to fit the fluorescence decays acquired with the pyrene-labelled PGA constructs, as the blobs represent compartments where pyrene excimer formation occurs in analogy to the SDS micelles.

The excimer emission decays exhibit a rise time as expected for the diffusive formation of excimer in organic solvents. The rise time can be inferred from the negative A_{E-}/A_{E+} ratios obtained from the fit of the excimer fluorescence decays with a sum of exponentials (Tables 4.1 and 4.2). As the pyrene content of the labelled constructs increases excimer formation occurs more rapidly, resulting in a shorter rise time (see inset of Figure 4.7).

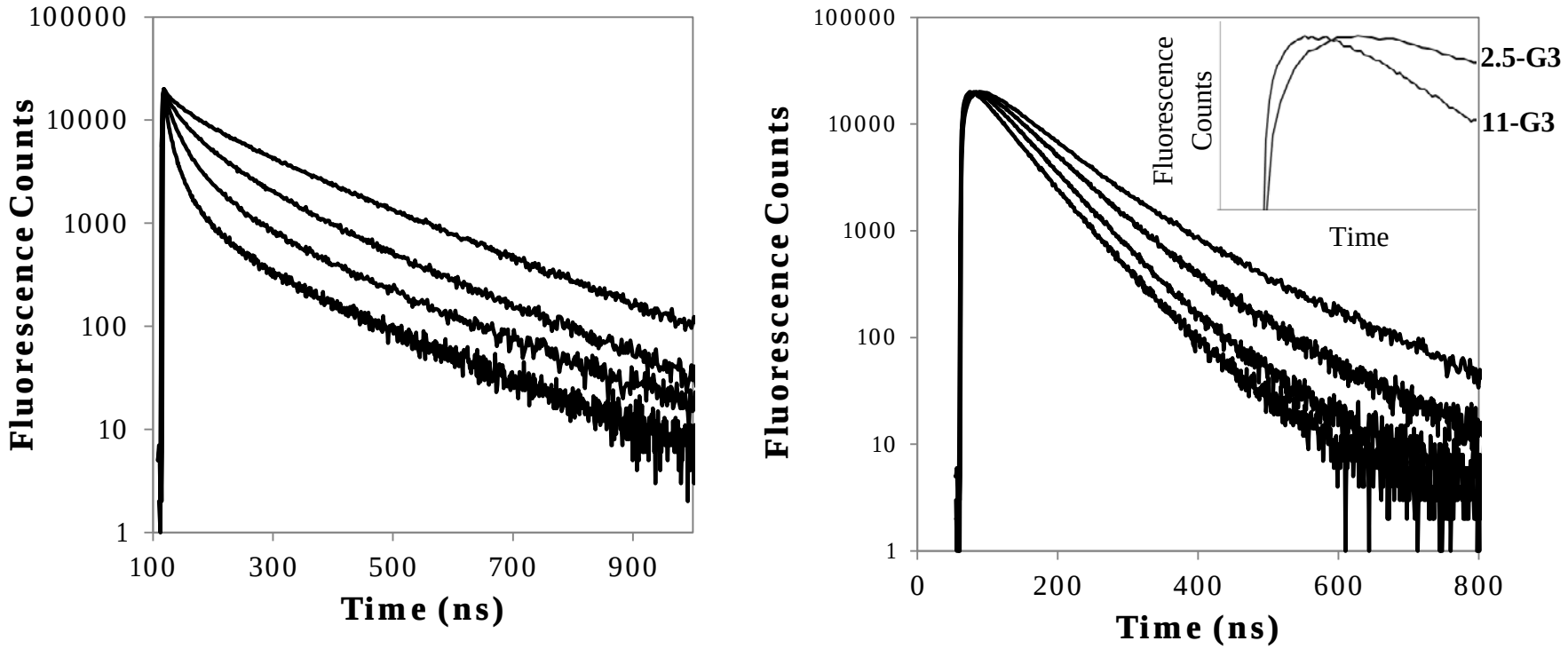

Figure 4.7: Time-resolved fluorescence decays for the pyrene monomer (left, λ_{em}= 375 nm) and excimer (right, λ_{em}= 510 nm) for Py-G3 arborescent PGA in DMF with pyrene contents of 2.5, 5.4, 9.4, and 11 mol% (top to bottom); λ_{ex}= 344 nm, [*Py*] = 2.5 $\times 10^{-6}$ M. Inset: Rise time for the samples with pyrene contents of 2.5 and 11 mol %.

The quantity $(\eta/\tau_M) \times [(\tau_M / <\tau>_N) - 1]$ was plotted as a function of pyrene content in Figure 4.8. For molecular pyrene, Figure 4.8 would be equivalent to a Stern-Volmer plot and $(\eta/\tau_M) \times [(\tau_M / <\tau>_N) - 1]$ is a measure of the rate constant of excimer formation corrected for the solvent viscosity and pyrene lifetime. This parameter is much larger for DMSO than for DMF, suggesting that excimer formation is much more efficient in DMSO than in DMF, presumably due to enhanced flexibility of the side-chains in DMSO. Furthermore, $(\eta/\tau_M) \times [(\tau_M / <\tau>_N) - 1]$ for a given pyrene content increases with the generation number of the arborescent construct, in agreement with the increased density and $[Py]_{local}$ of these polymers. This trend is consistent for all the PGA constructs, however it is more obvious when comparing the Py-linear and Py-G3 PGA samples.

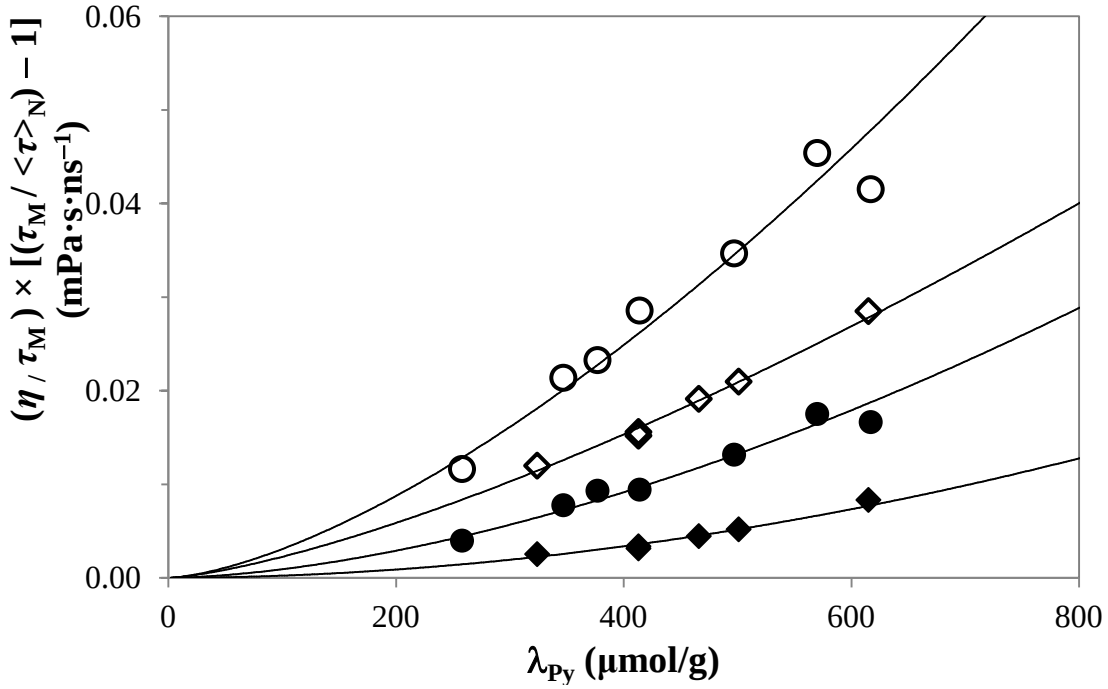

Figure 4.8: Plot of $(\eta/\tau_M) \times [(\tau_M / <\tau>_N) - 1]$ as a function of pyrene content for Py-Lin PGA (diamonds) and Py-G3 PGA (circles) in DMF (filled) and in DMSO (hollow).

4.4.4. Fluorescence Blob Model Results

Quantitative description of the internal dynamics experienced by the pyrene-labelled PGA constructs was obtained by fitting the time-resolved fluorescence decays for the monomer and excimer species obtained for all the Py-PGA constructs with the Fluorescence Blob Model (FBM). The k_2 parameter for the Py-PGA samples was optimized in the analysis, and was plotted as a function of corrected pyrene content in Figure 4.9. Samples with high pyrene contents had k_2 values larger and more variable than Py-PGA with lower levels of pyrene labelling, suggesting that the high levels of excimer formation influenced the optimization of the parameters for those samples, and provided further justification for the exclusion of samples with λ_{Py} greater than 800 μmol/g from the analysis. The variations observed in the value of k_2 are consistent with reports from earlier studies on polymers randomly labelled with pyrene and analyzed by the FBM.[68,76] The parameter took average values of 0.17±0.05 ns^{-1} and 0.12±0.03 ns^{-1} for Py-PGA in DMF and in DMSO respectively, indicating that the rate of rapid excimer formation is lower in DMSO. Rapid excimer formation for pyrene randomly attached on poly(L-glutamic acid) depends on the same two factors that affect excimer formation in the 1-pyrenemethylacetamide (PyMeAA) solutions, namely differences in the solvent viscosity and the probability of excimer formation. The differences between $<k_2>$ for Py-PGA in DMF and in DMSO should be similar to the differences between k_1 for PyMeAA in the same two solvents, since both pyrenes have similar chemical structures. The product $<k_2>\times\eta$ equals 0.24 and 0.13 $mPa{\cdot}s{\cdot}ns^{-1}$ in DMSO and in DMF, respectively. Thus, $<k_2>\times\eta$ is 80% larger in DMSO than in DMF, which is comparable with the 67% difference observed for $k_1\times\eta$ of PyMeAA in Figure 3.6. The minor discrepancy observed could be an indication that the probability (*p*-values) of

excimer formation is different for pyrene bound to a polymer, or else that the poly(L-glutamic acid) side-group dynamics are different for the α-helical and random coil conformations.

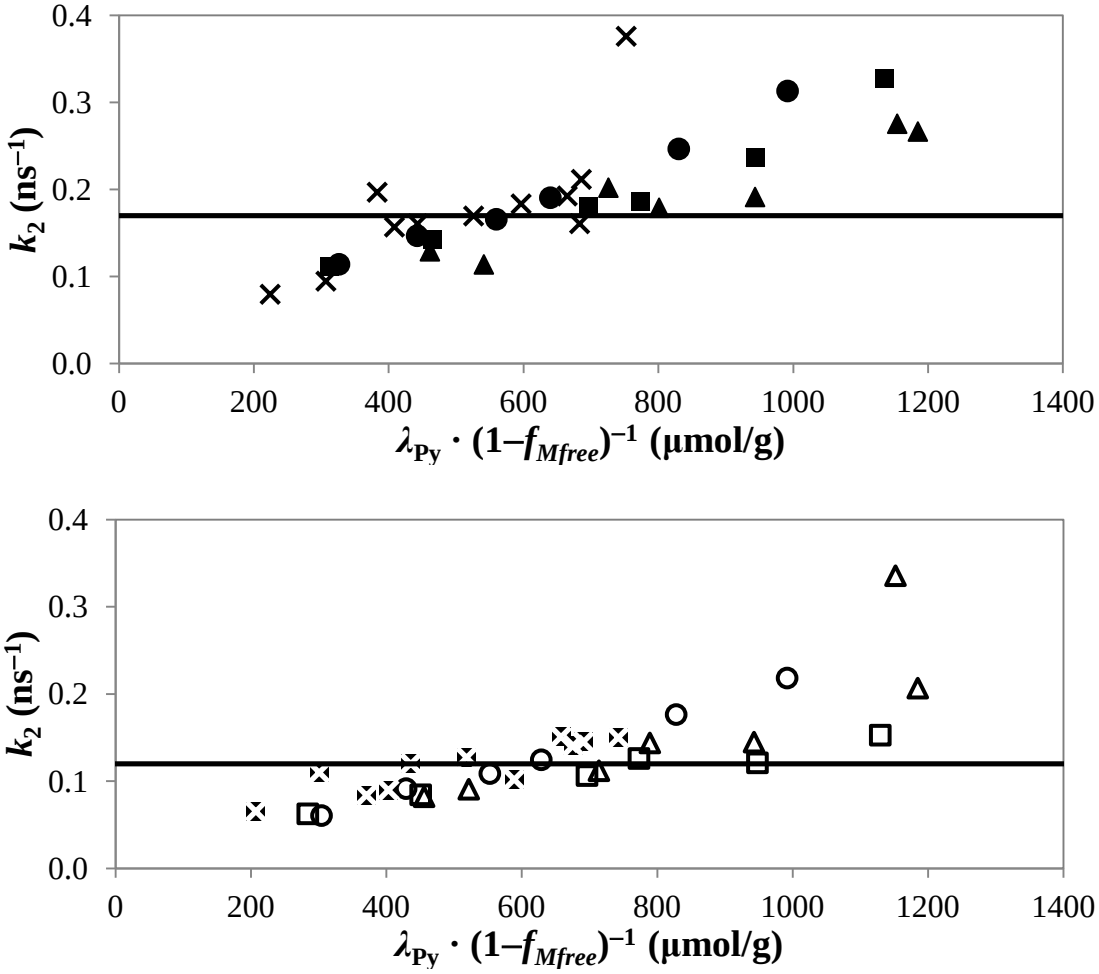

Figure 4.9: Plots of k_2 versus corrected pyrene content for Py-G0 (■,□), Py-G1 (▲,△), Py-G2 (●,○), and Py-G3 (✕, ☒) arborescent PGA constructs in DMF (top) and in DMSO (bottom).

The time-resolved fluorescence decays for the monomer and excimer species of all the Py-PGA constructs were fitted a second time with the Fluorescence Blob Model equations by fixing the k_2 value to $\langle k_2 \rangle$ in the analysis. The resulting parameters are listed in Tables E1-E30 in the

Appendix. It is noteworthy that k_{blob} retrieved from the analysis takes average values of 0.010±0.002 and 0.014±0.002 ns^{-1} in DMSO and in DMF, respectively, which is an order of magnitude smaller than k_2, in agreement with Scheme 4.2 since the dynamics of the polymer backbone are expected to be much slower than the rapid rearrangement of the pyrene labels in the side-groups.

The parameter N_{blob} was also determined for the pyrene-labelled PGA constructs and is plotted as a function of the corrected pyrene content in Figure 4.10. N_{blob} equals 14±2 for the linear PGA chains in DMF and in DMSO, a slightly smaller value than the number-average degree of polymerization of 16 (Table 2.3), which implies that the excited pyrene probes the entire PGA segment regardless of its conformation. The N_{blob} values for PGA increased for the branched constructs with increasing arborescent polymer generation numbers, implying that although pyrene excimer formation occurs intramolecularly in these systems, it involves more than one side-chain. It is noteworthy that larger N_{blob} values are obtained in DMSO, where PGA has been shown to adopt a random coil conformation. Comparatively, the helical conformation induced by DMF leads to more rigid PGA side-chains, which results in fewer interactions between the side-chains.

The product $k_{blob} \times N_{blob} \times \eta$, where k_{blob} and N_{blob} are obtained from the FBM analysis of the fluorescence decays and η is the solvent viscosity, has been shown to provide information on polymer coil density, backbone rigidity, and describe the internal dynamics of a macromolecule randomly labelled with pyrene.[18] The product $k_{blob} \times N_{blob} \times \eta$ was plotted as a function of the corrected pyrene content for each Py-PGA construct in Figure 4.11. In each solvent, a general trend is obtained where $k_{blob} \times N_{blob} \times \eta$ increases with increasing generation number, reflecting the larger $[Py]_{local}$ generated in the more compact PGA constructs.

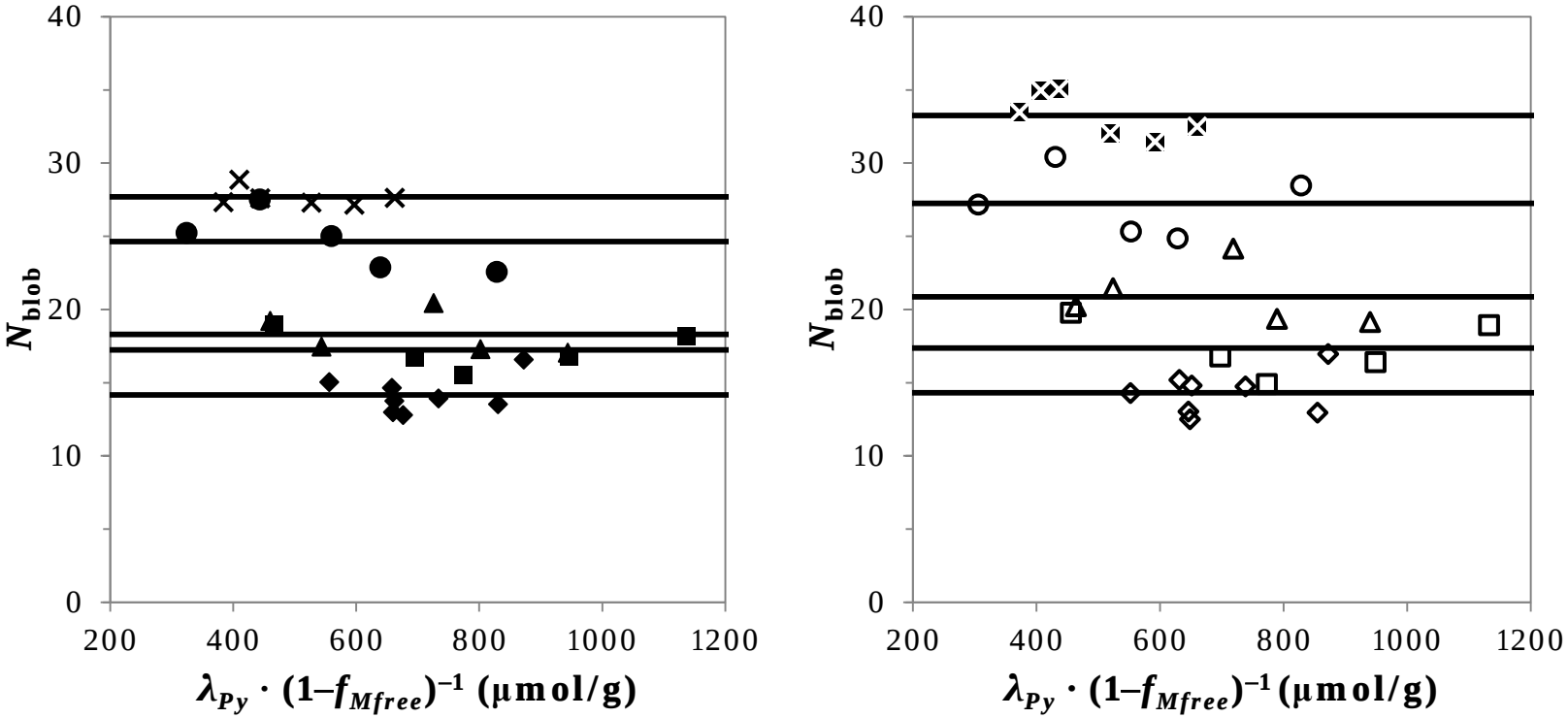

Figure 4.10: Plots of N_{blob} versus corrected pyrene content for Py-linear (◆,◇), Py-G0 (■,□), Py-G1 (▲,△), Py-G2 (●,○), and Py-G3 (✕, ☒) PGA arborescent constructs in DMF (filled symbols) and in DMSO (hollow symbols).

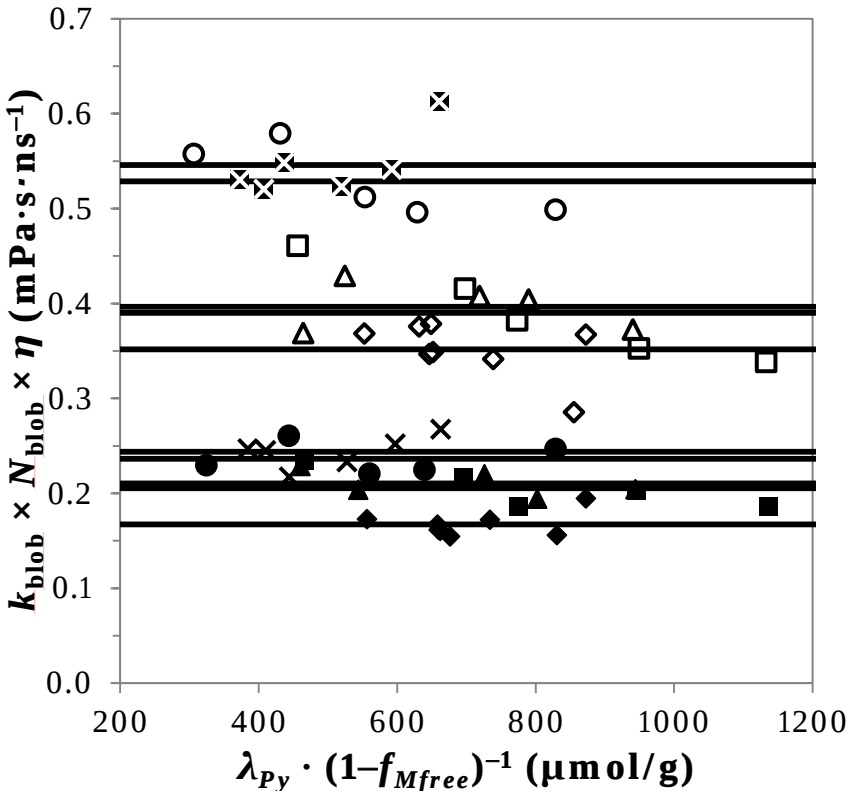

Figure 4.11: Plots of $k_{blob} \times N_{blob} \times \eta$ versus corrected pyrene content showing for Py-linear (◆,◇), Py-G0 (■,□), Py-G1 (▲,△), Py-G2 (●,○), and Py-G3 (✕, ☒) PGA arborescent constructs in DMF (filled symbols) and in DMSO (hollow symbols).

Values for N_{blob} and $k_{blob} \times N_{blob} \times \eta$ were plotted in Figure 4.12 as a function of the average number of linear side-chains in the outermost grafted layer (Table 2.3). The values and errors were estimated from the average and standard deviation values for the data presented in Figures 4.10 and 4.11. The trends show that N_{blob} increases with the number of side-chains to reach values larger than the degree of polymerization of a single side-chain, implying that several side-chains are involved in pyrene excimer formation. The increases in $k_{blob} \times N_{blob} \times \eta$ for increasing generation numbers reflect larger $[Py]_{local}$ values, that are proportional to the density of side-chains in the PGA constructs.

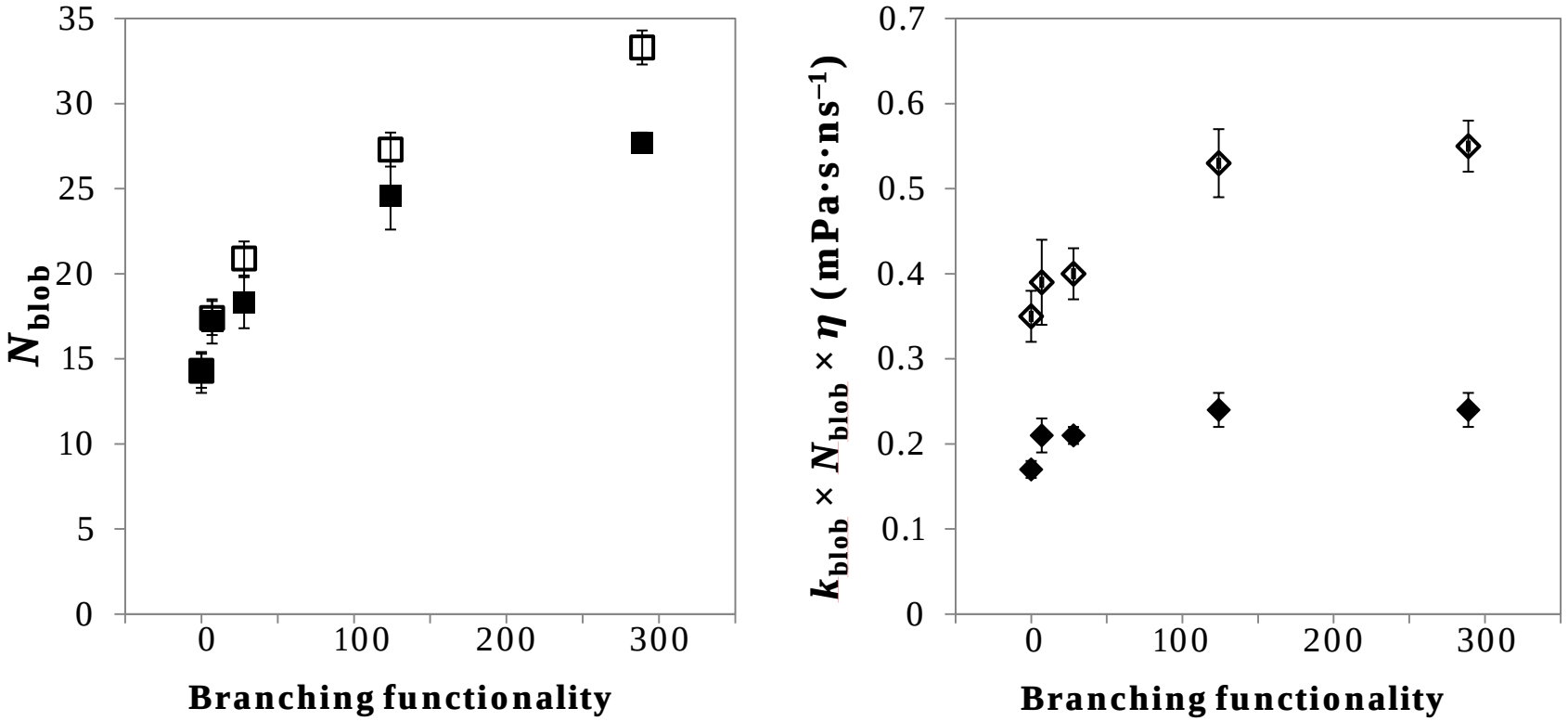

Figure 4.12: Plot of N_{blob} (left) and $k_{blob} \times N_{blob} \times \eta$ (right) versus the number of peripheral branches for linear and arborescent PGA constructs in DMF (filled symbols) and DMSO (hollow symbols).

To discuss differences in chain dynamics induced by the solvent, the ratios $(k_{blob} \times N_{blob} \times \eta)^{DMSO} / (k_{blob} \times N_{blob} \times \eta)^{DMF}$ and $N_{blob}^{DMSO} / N_{blob}^{DMF}$, where the indices "DMF" and "DMSO" refer the solvent in which the parameters were determined, are plotted in Figure 4.13 as a function of the average number of linear side-chains in the outermost grafted layer. Their values and errors were estimated from the data presented in Figure 4.12, with propagation of the uncertainties. The solvent-induced differences observed as a function of the arborescent PGA generation number in Figure 4.12 are consistent for all generations, yielding $k_{blob} \times N_{blob} \times \eta$ values in DMSO that are on average 2.1±0.2 times larger than in DMF. This unambiguously indicates that the dynamics of the side-chains are faster in DMSO than in DMF. Ingratta *et al.* reported for polystyrene randomly labelled with pyrene that $k_{blob} \times N_{blob}$ increased for decreasing solvent viscosities.[76] Based on their results, $k_{blob} \times N_{blob} \times \eta$ should be 1.6±0.2 times larger in DMSO than in DMF, a factor somewhat smaller than that found in Figure 4.13. The larger factor found for the PGA constructs is therefore attributed to the ability of PGA to undergo a coil-to-helix transition when the solvent is changed from DMSO to DMF. In comparison polystyrene, being a more flexible polymer, retains its random coil conformation regardless of the solvent type used. The larger than expected $k_{blob} \times N_{blob} \times \eta$ values obtained in DMSO indicate that the PGA side-chains experience a higher mobility, which leads to much faster pyrene excimer formation when the side-chains adopt a random coil conformation.

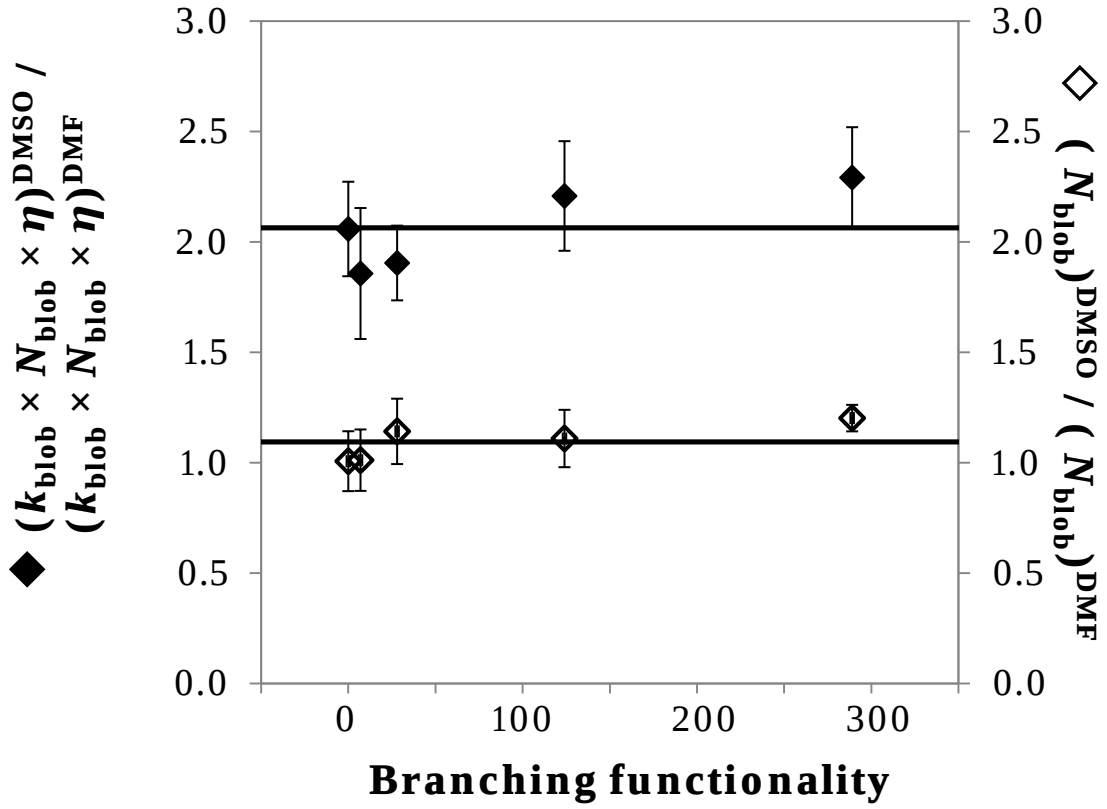

Figure 4.13: Plot of the ratios $(k_{blob} \times N_{blob} \times \eta)^{DMSO} / (k_{blob} \times N_{blob} \times \eta)^{DMF}$ (◆) and $N_{blob}^{DMSO} / N_{blob}^{DMF}$ (◇) versus the number of peripheral branches for the linear and arborescent PGA constructs.

In Figure 4.13 the ratio $N_{blob}^{DMSO} / N_{blob}^{DMF}$ takes an average value of 1.1±0.1 for all the constructs investigated. If N_{blob} depended solely on the chain dynamics of PGA, it would be larger in DMSO than in DMF. This was not observed. Excimer formation is also proportional to $[Py]_{local}$ however, which depends on the polymer density. The hydrodynamic diameter differences observed for G1 and G2 arborescent PGA molecules (Table 2.2) indicate that the interior of the PGA molecules is denser in DMF than in DMSO. Consequently, it appears that the faster dynamics of the branched PGA constructs in DMSO are negated by their lower

hydrodynamic density. The G3 arborescent PGA molecules, that have equivalent hydrodynamic diameters in both solvents, exhibit an N_{blob} increase of 20% in DMSO as compared to DMF, clearly resulting from differences in polymer rigidity due to the different conformations rather than variations in hydrodynamic density. Furthermore, k_{blob} is the product of the bimolecular rate constant for excimer formation, k_{diff}, times the inverse of the *blob* volume, V_{blob}. As a consequence, the product $k_{blob} \times N_{blob}$ is the product of k_{diff} and the local density of the macromolecule, N_{blob}/V_{blob}. The fact that k_{diff} is more than twice as large in DMSO as in DMF, despite the higher density (N_{blob}/V_{blob}) of the PGA construct in DMF, is again a clear demonstration that the PGA constructs exhibit much faster internal dynamics in DMSO than in DMF.

4.5. Conclusions

Linear, comb-branched, and arborescent PGA molecules were labelled with varying amounts of pyrene, their fluorescence spectra and decays were acquired in DMF and in DMSO, and analyzed by several methods. The level of excimer formation was quantified by monitoring the I_E/I_M ratio, which increased with increasing pyrene content. The fluorescence emissions decays were fitted with a sum of exponentials to determine the number-average fluorescence lifetime, and provide a qualitative description of the efficiency of excimer formation, or the Fluorescence Blob Model to retrieve quantitative parameters describing the dynamics and distribution of pyrene in the polymer. As the pyrene content increased for a given PGA construct, $\eta \times \tau_M^{-1} \times I_E/I_M$ and $(\eta/\tau_M) \times [(\tau_M / <\tau>_N) - 1]$ increased due to the higher levels of $[Py]_{local}$. For a given pyrene content, N_{blob}, $k_{blob} \times N_{blob} \times \eta$, $\eta \times \tau_M^{-1} \times I_E/I_M$, and $(\eta/\tau_M) \times [(\tau_M/<\tau>_N) - 1]$ increased for

increasing generation numbers, due to the increased density of the PGA side-chains. All of these values were larger when measured for samples in DMSO, suggesting that excimer formation is more efficient than in DMF, presumably due to enhanced flexibility and faster dynamics of the coiled side-chains. The intramolecular chain dynamics of these pyrene-labelled macromolecules were determined to occur on a much slower timescale than the side-groups, as indicated by differences between k_{blob} and k_2. Differences between the ratios $(k_{\mathrm{blob}} \times N_{\mathrm{blob}} \times \eta)^{\mathrm{DMSO}} / (k_{\mathrm{blob}} \times N_{\mathrm{blob}} \times \eta)^{\mathrm{DMF}}$ and $N_{blob}^{DMSO} / N_{blob}^{DMF}$ indicated that the different conformations produced differences in side-chain rigidity affecting the dynamics of the polymer. More generally, these results imply that there is a relationship between the internal dynamics of amino acid side-groups, the intramolecular interactions of neighbouring amino acid segments which constitute a protein, and the structure of the protein.

5. Conclusions and Suggestions for Future Work

5.1. Conclusions

^{1}H NMR spectroscopy analysis was used to determine the conformation of linear and arborescent poly(L-glutamic acid) (PGA) samples. The results showed that the side-chains of these PGA constructs adopted α-helical and random coil conformations in *N*,*N*-dimethylformamide (DMF) and in dimethyl sulfoxide (DMSO) respectively. Dynamic light scattering measurements were used to determine the hydrodynamic diameter (D_h) of these macromolecules. In each solvent, D_h was found to increase for increasing generation numbers. For a given generation number, D_h was larger in DMSO than in DMF in most cases, as expected from the conformation of the side-chains of the arborescent PGA molecules determined by NMR analysis. The only exception to this rule was the G3 sample, for which the overcrowded interior of the molecules apparently led to a conformation change for some of the PGA side-chains from α-helix to random coil.

Information on the internal dynamics of these constructs in solution was obtained after labelling the macromolecules with 1-pyrenemethylamine and analyzing their fluorescence emission spectra and decays. After accounting for viscosity and lifetime differences, comparison of the I_E/I_M ratios obtained in DMF and in DMSO demonstrated that the helical conformation of the PGA side-chains led to slower chain dynamics, and that arborescent PGAs were most efficient at forming excimer because of their higher hydrodynamic density. Fluorescence Blob Model analysis of the fluorescence decays acquired for the different pyrene-labelled PGA constructs provided quantitative information on side-chain dynamics. The N_{blob} values determined for PGA increased from 14±2 for the smallest linear chains to as high as 26±2 and 33±2 in DMF and in DMSO, respectively, for the largest Py-G3 arborescent PGA construct.

This result implies that although pyrene excimer formation occurs intramolecularly inside the arborescent PGA molecules, it involves the interactions between different PGA side-chains. Furthermore, side-chain movements were significantly faster when the side-chains of the arborescent PGA constructs adopted a random coil conformation in DMSO, as deduced from the product $k_{blob} \times N_{blob} \times \eta$.

Overall, these results imply that the formation of structural motives inside a polypeptide slows down its internal dynamics. Given that protein folding relies on the internal dynamics of a polypeptide, it is likely that for proteins in an unfolded state, faster dynamics and enhanced intramolecular interactions may have an effect on its folding pathway. The hydrodynamic density for PGA arborescent polymers was also concluded to influence the intramolecular interactions and the polymer conformation. These conclusions may be extended to proteins, and provide an explanation for observed differences between the folding of small proteins such as chymotrypsin inhibitor 2, and larger proteins such as hen lysozyme.[3–5]

5.2. Future Work

To obtain a more complete picture of the extent of side-chain interactions within arborescent polymer molecules, it would be necessary to synthesize PGA-based polymers that only have a fraction (e.g. between 5% and 25%) of the side-chains labelled with pyrene and randomly distributed throughout the macromolecule. By decreasing the number of side-chains labelled with pyrene, observation of the fluorescence response would indicate how the individual side-chains behave in a given arborescent construct, and may allow the identification of a specific threshold for side-chain interaction. Furthermore, it may be interesting to synthesize arborescent molecules having specific PGA side-chain layers labelled with pyrene, particularly for the G3

arborescent PGA structure, which was shown to have side-chains predominantly in an α-helical conformation but with some adopting a more random coil conformation. Depending on whether the pyrene-labelled side-chains are located only in the interior of the arborescent macromolecule or are incorporated only in the last grafting cycle, this may give an indication of how the conformation and side-chain mobility varies due to the hydrodynamic density or the grafting density of each polymer layer.

Secondly, it was observed that the N_{blob} values for the linear PGA sample were equivalent to the total number of units in the polymer chain, implying that the entire chain was being probed by an excited pyrene label. It is possible that a larger volume could be probed if the polymer chain were longer, as it has already been found.[22,23] It would therefore be worthwhile to study a series of PGA samples having not only different branching functionalities, but also different side-chain molecular weights. The current study focused on macromolecules where only the branching functionality was varied. The study of arborescent PGA having side-chains with a higher molecular weight might therefore provide a more comprehensive description of the dynamics of arborescent polymers.

Finally, to determine the impact that different amino acids have on the folding dynamics of polypeptides and globular proteins, additional polypeptides could be studied to determine how their sequences affect the internal dynamics of the resulting arborescent polypeptides. Furthermore, chain dynamics investigations of arborescent polypeptides should be ideally conducted in aqueous solutions. This would require the development of water-soluble fluorescent probes, as the pyrene labels used in this study are known for their hydrophobicity.

References

(1) Radford, S. E.; Dobson, C. M. From computer simulations to human disease: emerging themes in protein folding. *Cell* **1999**, *97*, 291–298.

(2) Thomas, P. J.; Qu, B. H.; Pedersen, P. L. Defective protein folding as a basis of human disease. *Trends Biochem. Sci*. **1995**, *20*, 456–459.

(3) Jackson, S. E.; Fersht, A. R. Folding of chymotrypsin inhibitor 2. 1. Evidence for a two-state transition. *Biochemistry* **1991**, *30*, 10428–10435.

(4) Jackson, S. E.; Fersht, A. R. Folding of chymotrypsin inhibitor 2. 2. Influence of proline isomerization on the folding kinetics and thermodynamic characterization of the transition state of folding. *Biochemistry* **1991**, *30*, 10436–10443.

(5) Radford, S. E.; Dobson, C. M.; Evans, P. A. The folding of hen lysozyme involves partially structured intermediates and multiple pathways. *Nature* **1992**, *358*, 302–307.

(6) Shaw, D. E.; Maragakis, P.; Lindorff-Larsen, K.; Piana, S.; Dror, R. O.; Eastwood, M. P.; Bank, J. A.; Jumper, J. M.; Salmon, J. K.; Shan, Y.; Wriggers, W. Atomic-level characterization of the structural dynamics of proteins. *Science* **2010**, *330*, 341–346.

(7) Sheppard, D.; Sprangers, R.; Tugarinov, V. Experimental approaches for NMR studies of side-chain dynamics in high-molecular-weight proteins. *Prog. Nucl. Mag. Res. Sp.* **2010**, *56*, 1–45.

(8) Sibille, N.; Favier, A.; Azuaga, A. I.; Ganshaw, G.; Bott, R.; Bonvin, A. M. J. J.; Boelens, R.; van Nuland, N. A. J. Comparative NMR study on the impact of point mutations on protein stability of Pseudomonas mendocina lipase. *Protein Sci.* **2006**, *15*, 1915–1927.

(9) Canet, D.; Doering, K.; Dobson, C. M.; Dupont, Y. High-sensitivity fluorescence anisotropy detection of protein-folding events: application to alpha-lactalbumin. *Biophys. J*. **2001**, *80*, 1996–2003.

(10) Verheyden, G.; Matrai, J.; Volckaert, G.; Engelborghs, Y. A fluorescence stopped-flow kinetic study of the conformational activation of α-chymotrypsin and several mutants. *Protein Sci*. **2004**, *13*, 2533–2540.

(11) Bucci, E.; Steiner, R. F. Anisotropy decay of fluorescence as an experimental approach to protein dynamics. *Biophys. Chem.* **1988**, *30*, 199–224.

(12) Rothwarf, D. M.; Scheraga, H. A. Role of non-native aromatic and hydrophobic interactions in the folding of hen egg white lysozyme. *Biochemistry* **1996**, *35*, 13797–13807.

(13) Mark, A. E.; Van Gunsteren, W. F. Simulation of the thermal denaturation of hen egg white lysozyme: trapping the molten globule state. *Biochemistry* **1992**, *31*, 7745–7748.

(14) Radford, S. E.; Buck, M.; Topping, K. D.; Dobson, C. M.; Evans, P. A. Hydrogen exchange in native and denatured states of hen egg-white lysozyme. *Proteins* **2004**, *14*, 237–248.

(15) Gauthier, M.; Munam, A. Cross-linked latex particles grafted with polyisoprene as model rubber-compatible fillers. *Polymer* **2009**, *50*, 6032–6042.

(16) Njikang, G. N.; Gauthier, M.; Li, J. Sustained release properties of arborescent polystyrene-graft-poly(2-vinylpyridine) copolymers. *Polymer* **2008**, *49*, 5475–5481.

(17) Maeda, K.; Kamiya, N.; Yashima, E. Poly(phenylacetylene)s bearing a peptide pendant: helical conformational changes of the polymer backbone stimulated by the pendant conformational change. *Chemistry* **2004**, *10*, 4000–4010.

(18) Duhamel, J. New insights in the study of pyrene excimer fluorescence to characterize macromolecules and their supramolecular assemblies in solution. *Langmuir* **2012**, *28*, 6527–6538.

(19) Cuniberti, C.; Perico, A. Intramolecular excimer formation in polymers: Pyrene labelled polyvinylacetate. *Eur. Polym. J.* **1980**, *16*, 887–893.

(20) Zachariasse, K.; Kühnle, W. Intramolecular excimers with α,ω-diarylalkanes. *Z. Phys. Chem. Neue F* **1976**, *101*, 267–276.

(21) Winnik, F. M. Photophysics of preassociated pyrenes in aqueous polymer solutions and in other organized media. *Chem. Rev.* **1993**, *93*, 587–614.

(22) Duhamel, J.; Kanagalingam, S.; O'Brien, T. J.; Ingratta, M. W. Side-chain dynamics of an α-helical polypeptide monitored by fluorescence. *J. Am. Chem. Soc.* **2003**, *125*, 12810–12822.

(23) Ingratta, M.; Duhamel, J. Effect of side-chain length on the side-chain dynamics of α-helical poly(l-glutamic acid) as probed by a fluorescence blob model. *J. Phys. Chem. B* **2008**, *112*, 9209–9218.

(24) Pauling, L.; Corey, R. B. Atomic coordinates and structure factors for two helical configurations of polypeptide chains. *Proc. Natl. Acad. Sci.* **1951**, *37*, 235 –240.

(25) Doty, P.; Bradbury, J. H.; Holtzer, A. M. Polypeptides. IV. The molecular weight, configuration and association of poly-γ-benzyl-L-glutamate in various solvents. *J. Am. Chem. Soc.* **1956**, *78*, 947–954.

(26) Mitchell, J. C.; Woodward, A. E.; Doty, P. Polypeptides. XVI. The polydispersity and configuration of low molecular weight poly-γ-benzyl-L-glutamates. *J. Am. Chem. Soc.* **1957**, *79*, 3955–3960.

(27) Kitevski-LeBlanc, J. L.; Prosser, R. S. Current applications of ^{19}F NMR to studies of protein structure and dynamics. *Prog. Nucl. Mag. Res. Sp.* **2012**, *62*, 1–33.

(28) Morin, S. A practical guide to protein dynamics from ^{15}N spin relaxation in solution. *Prog. Nucl. Mag. Res. Sp.* **2011**, *59*, 245–262.

(29) Deming, T. J. Synthetic polypeptides for biomedical applications. *Prog. Polym. Sci.* **2007**, *32*, 858–875.

(30) Baigude, H.; Katsuraya, K.; Okuyama, K.; Tokunaga, S.; Uryu, T. Synthesis of sphere-type monodispersed oligosaccharide−polypeptide dendrimers. *Macromolecules* **2003**, *36*, 7100–7106.

(31) Klok, H.-A.; Rodríguez-Hernández, J. Dendritic−graft polypeptides. *Macromolecules* **2002**, *35*, 8718–8723.

(32) Aliferis, T.; Iatrou, H.; Hadjichristidis, N.; Messman, J.; Mays, J. Synthesis of 3- and 4-arm star-block copolypeptides using multifunctional amino initiators and high vacuum techniques. *Macromol. Symp.* **2006**, *240*, 12–17.

(33) Duhamel, J. Internal dynamics of dendritic molecules probed by pyrene excimer formation. *Polymers* **2012**, *4*, 211–239.

(34) Lescanec, R. L.; Muthukumar, M. Configurational characteristics and scaling behavior of starburst molecules: a computational study. *Macromolecules* **1990**, *23*, 2280–2288.

(35) Ballauff, M.; Likos, C. N. Dendrimers in solution: Insight from theory and simulation. *Angew. Chem. Inter. Ed.* **2004**, *43*, 2998–3020.

(36) de Gennes, P. G.; Hervet, H. Statistics of «starburst» polymers. *J. Phys. Lett.* **1983**, *44*, 351–360.

(37) Striolo, A.; Prausnitz, J. .; Bertucco, A.; Kee, R. .; Gauthier, M. Dilute-solution properties of arborescent polystyrenes: Further evidence for perturbed-hard-sphere behavior. *Polymer* **2001**, *42*, 2579–2584.

(38) Yun, S. I.; Lai, K.-C.; Briber, R. M.; Teertstra, S. J.; Gauthier, M.; Bauer, B. J. Conformation of arborescent polymers in solution by small-angle neutron scattering: Segment density and core−shell morphology. *Macromolecules* **2007**, *41*, 175–183.

(39) Gauthier, M.; Tichagwa, L.; Downey, J. S.; Gao, S. Arborescent graft copolymers: Highly branched macromolecules with a core-shell morphology. *Macromolecules* **1996**, *29*, 519–527.

(40) Leuchs, H. On the glycine carbonic acid. *Ber.* **1906**, *39*, 857–61.

(41) Whitton, G. Personal communication. **2010**.

(42) Bovey, F. A. NMR observations of polypeptide conformations. *J. Polym. Sci.: Macromol Rev* **1974**, *9*, 1–81.

(43) Markley, J. L.; Meadows, D. H.; Jardetzky, O. Nuclear magnetic resonance studies of helix-coil transitions in polyamino acids. *J. Mol. Biol.* **1967**, *27*, 25–40.

(44) Ferretti, J. A. 100 Mc./sec. nuclear magnetic resonance study of the helix–coil transformation in polypeptides. *Chem. Comm.* **1967**, 1030–1032.

(45) Doty, P.; Wada, A.; Yang, J. T.; Blout, E. R. Polypeptides. VIII. Molecular configurations of poly-L-glutamic acid in water-dioxane solution. *J. Polym. Sci.* **1957**, *23*, 851–861.

(46) Nagasawa, M.; Holtzer, A. The helix-coil transition in solutions of polyglutamic acid. *J. Am. Chem. Soc.* **1964**, *86*, 538–543.

(47) Appel, P.; Yang, J. T. Helix-coil transition of poly-L-glutamic acid and poly-L-lysine in D2O. *Biochemistry* **1965**, *4*, 1244–1249.

(48) Lader, H. J.; Komoroski, R. A.; Mandelkern, L. A nuclear magnetic resonance study of the helix-coil transition of poly(L-glutamic acid). *Biopolymers* **1977**, *16*, 895–905.

(49) Lader, H. J.; Mandelkern, L. Origin of multipeak behavior in the NMR spectra of poly(L-glutamic acid). *Biopolymers* **1979**, *18*, 2607–2623.

(50) Grigoryev, A. I.; Volkova, L. A.; Ptitsyn, O. B. Identification of the secondary structure of polypeptide chains in solution by X-ray diffusion scattering. *FEBS Lett.* **1971**, *14*, 189–191.

(51) Leung, A. *Novel pH-responsive hybrid peptide block copolymers for intracellular delivery applications*. Thesis (MASc), University of Waterloo: Waterloo, Ontario, 2011.

(52) Jakeš, J. Testing of the constrained regularization method of inverting Laplace transform on simulated very wide quasielastic light scattering autocorrelation functions. *Czech. J. Phys.* **1988**, *38*, 1305–1316.

(53) Schillen, K.; Brown, W.; Johnsen, R. M. Micellar sphere-to-rod transition in an aqueous triblock copolymer system. A dynamic light scattering study of translational and rotational diffusion. *Macromolecules* **1994**, *27*, 4825–4832.

(54) Tscharnuter, W. Photon correlation spectroscopy in particle sizing. *Encyclopedia of Analytical Chemistry* **2000**, 5469–5485.

(55) Dai, S.; Tam, K. C.; Jenkins, R. D. Microstructure of dilute hydrophobically modified alkali soluble emulsion in aqueous salt solution. *Macromolecules* **1999**, *33*, 404–411.

(56) Brehm, G. A.; Bloomfield, V. A. Analysis of polydispersity in polymer solutions by inelastic laser light scattering. *Macromolecules* **1975**, *8*, 663–665.

(57) Scheraga, H. A.; Silverman, D. N. Nuclear magnetic resonance studies of side-chain interactions in polyamino acids with aromatic groups. Comparison to conformational energy calculations. *Biochemistry* **1971**, *10*, 1340–1347.

(58) Berlman, I. B. *Handbook of fluorescence spectra of aromatic molecules*; 2nd ed.; Academic Pr, 1971.

(59) Duhamel, J. *Molecular interfacial phenomena of polymers and biopolymers*; Chen, P., Ed.; Woodhead: New York, 2005.

(60) Anghel, D. F.; Alderson, V.; Winnik, F. M.; Mizusaki, M.; Morishima, Y. Fluorescent dyes as model “hydrophobic modifiers” of polyelectrolytes: a study of poly(acrylic acid)s labelled with pyrenyl and naphthyl groups. *Polymer* **1998**, *39*, 3035–3044.

(61) Zachariasse, K. A.; Vaz, W. L. C.; Sotomayor, C.; Kühnle, W. Investigation of human erythrocyte ghost membranes with intramolecular excimer probes. *Biochim. Biophys. Acta - Biomembranes* **1982**, *688*, 323–332.

(62) Lakowicz, J. *Principles of fluorescence spectroscopy*; Plenum Press: New York, 1983.

(63) Yekta, A.; Duhamel, J.; Winnik, M. A. Diffusion reaction in restricted spaces of spherical symmetry: Surface quenching of luminescence. *J. Chem. Phys.* **1992**, *97*, 1554–1561.

(64) Birks, J. *Photophysics of Aromatic Molecules*; Wiley-Interscience, 1970.

(65) Chen, S.; Duhamel, J.; Winnik, M. A. Probing end-to-end cyclization beyond Willemski and Fixman. *J. Phys. Chem. B* **2011**, *115*, 3289–3302.

(66) Cheung, S.-T.; Winnik, M. A.; Redpath, A. E. C. Cyclization dynamics of polymers, 5. The effects of solvent on end-to-end cyclization of poly(ethylene oxide) probed by intramolecular pyrene excimer formation. *Makromol. Chem.* **1982**, *183*, 1815–1824.

(67) Ingratta, M.; Duhamel, J. Effect of viscosity on long-range polymer chain dynamics in solution studied with a fluorescence blob model. *Macromolecules* **2009**, *42*, 1244–1251.

(68) Yip, J.; Duhamel, J.; Qiu, X. P.; Winnik, F. M. Long-range polymer chain dynamics of pyrene-labeled poly(*N*-isopropylacrylamide)s studied by fluorescence. *Macromolecules* **2011**, *44*, 5363–5372.

(69) Keyes-Baig, C.; Duhamel, J.; Wettig, S. Characterization of the behavior of a pyrene substituted gemini surfactant in water by fluorescence. *Langmuir* **2011**, *27*, 3361–3371.

(70) Winnik, M. A. End-to-end cyclization of polymer chains. *Acc. Chem. Res.* **1985**, *18*, 73–79.

(71) Mathew, A. K.; Siu, H.; Duhamel, J. A blob model to study chain folding by fluorescence. *Macromolecules* **1999**, *32*, 7100–7108.

(72) Duhamel, J.; Yekta, A.; Winnik, M. A.; Jao, T. C.; Mishra, M. K.; Rubin, I. D. A blob model to study polymer chain dynamics in solution. *J. Phys. Chem.* **1993**, *97*, 13708–13712.

(73) Siu, H.; Duhamel, J. Molar absorption coefficient of pyrene aggregates in water. *J. Phys. Chem. B* **2008**, *112*, 15301–15312.

(74) Aikawa, M.; Yekta, A.; Turro, N. J. Photoluminescence probes of micelle systems. Cyclic azoalkanes as quenchers of 1,5-dimethylnaphthalene fluorescence. *Chem. Phys. Lett.* **1979**, *68*, 285–290.

(75) Yekta, A.; Aikawa, M.; Turro, N. J. Photoluminescence methods for evaluation of solubilization parameters and dynamics of micellar aggregates. Limiting cases which allow estimation of partition coefficients, aggregation numbers, entrance and exit rates. *Chem. Phys. Lett.* **1979**, *63*, 543–548.

(76) Ingratta, M.; Mathew, M.; Duhamel, J. How switching the substituent of a pyrene derivative from a methyl to a butyl affects the fluorescence response of polystyrene randomly labeled with pyrene. *Can. J. Chem.* **2010**, *88*, 217–227.

Appendix A: Nuclear Magnetic Resonance Spectroscopy Results

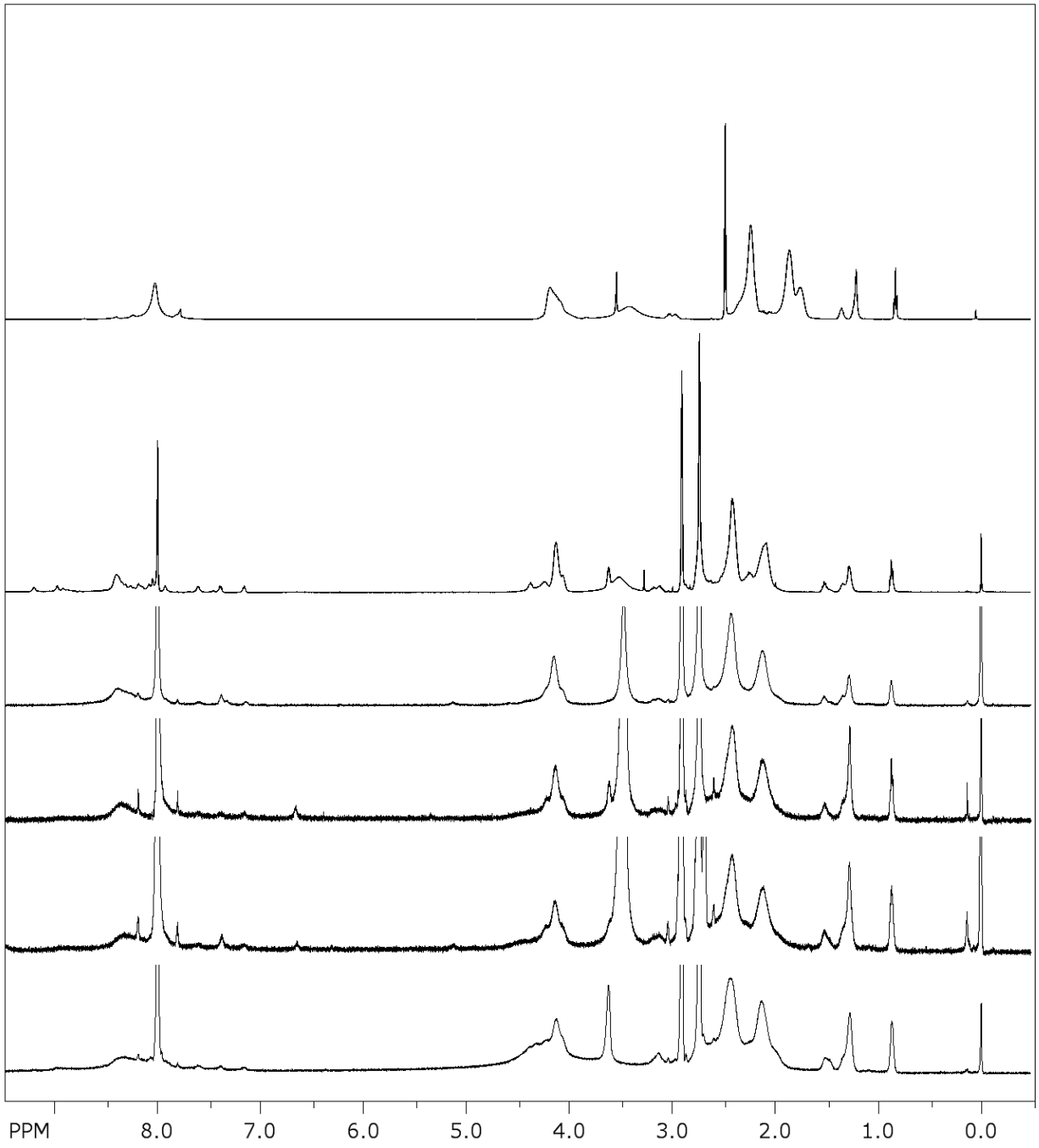

Figure A1: ^{1}H NMR (500 MHz) spectra for linear PGA in DMSO-d6 and for linear, G0, G1, G2, G3 PGA samples in DMF-d7 (top to bottom).

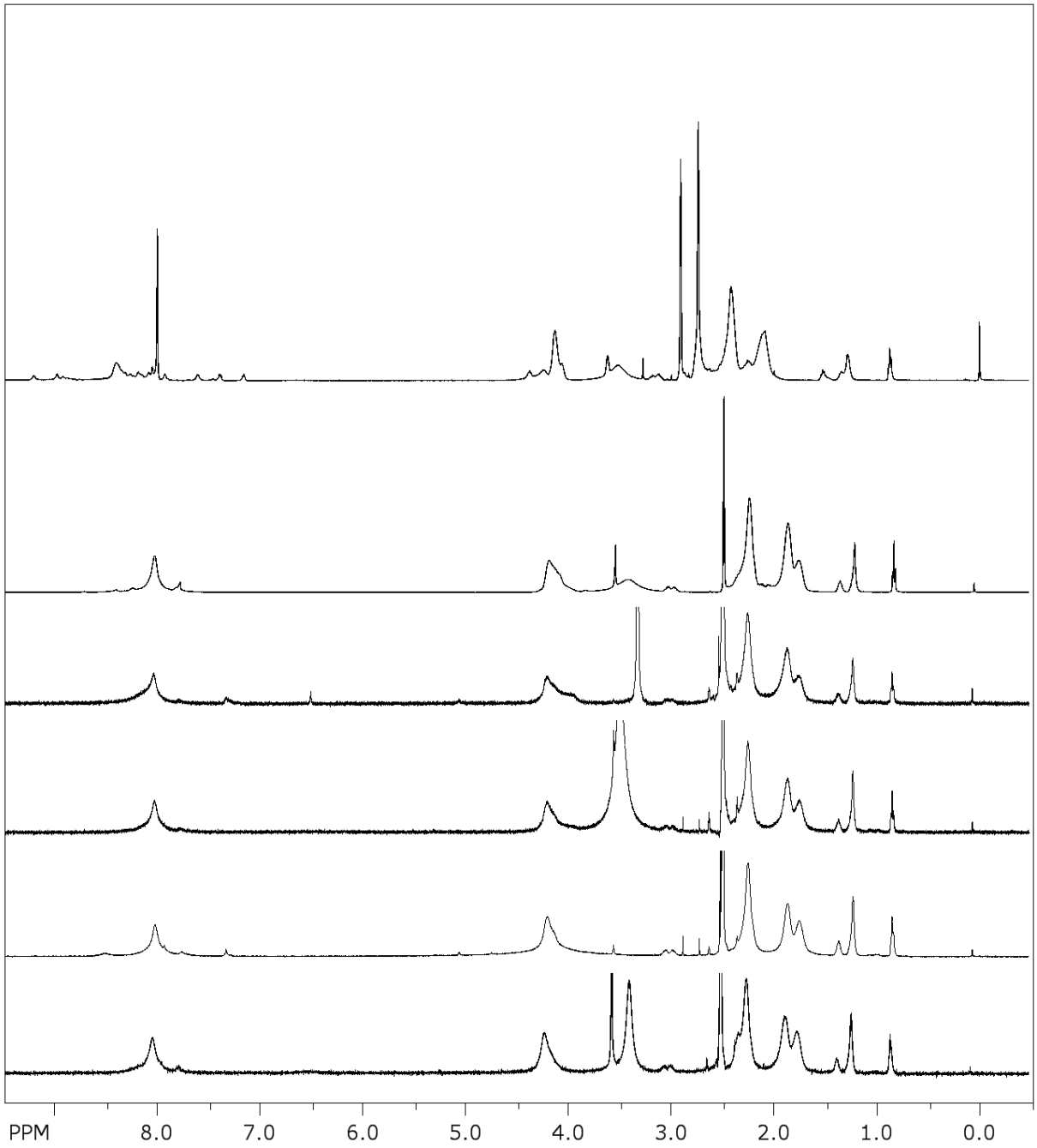

Figure A2: ^{1}H NMR (500 MHz) spectra for linear PGA in DMF-d7 and for linear, G0, G1, G2, G3 PGA samples in DMSO-d6 (top to bottom).

Appendix B: Dynamic Light Scattering Results

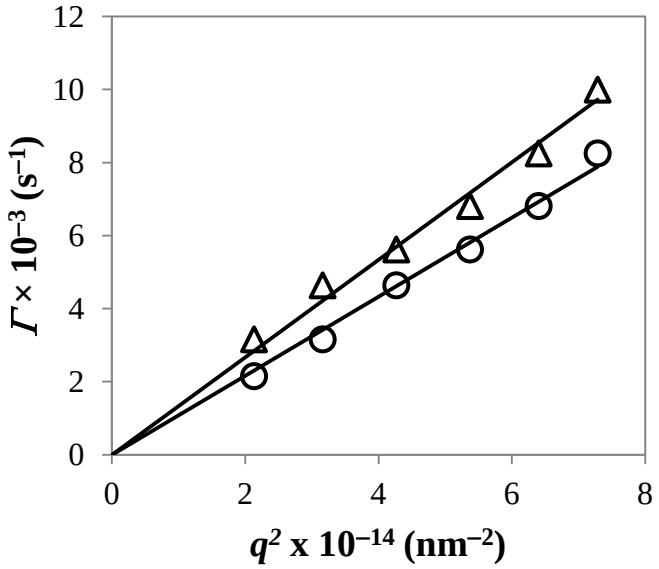

Figure B1: The q^2 dependence of the relaxation rate of scattered light intensity for the diffusion coefficient of G2 (○) and G1 (△) PGA in DMSO.

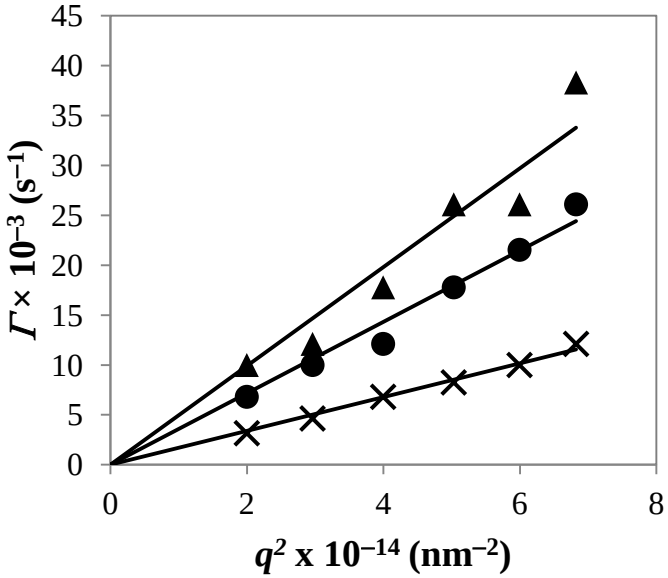

Figure B2: The q^2 dependence of the relaxation rate of scattered light intensity for the diffusion coefficient of G1 (▲), G2 (●), and G3 (×) PGA in DMF.

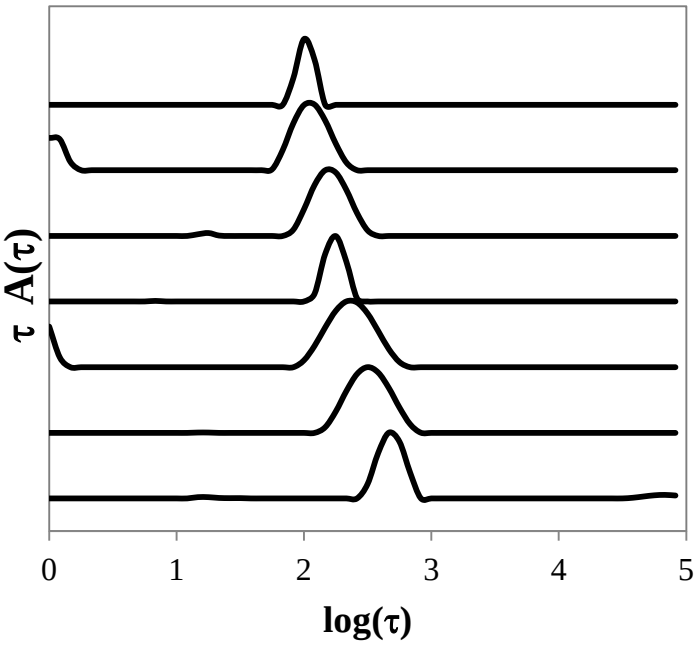

Figure B3: Distribution functions for the time decay rate of scattered light intensity by G2 PGA in DMSO measured at 150°, 135°, 120°, 105°, 90°, 75°, and 60° (top to bottom).

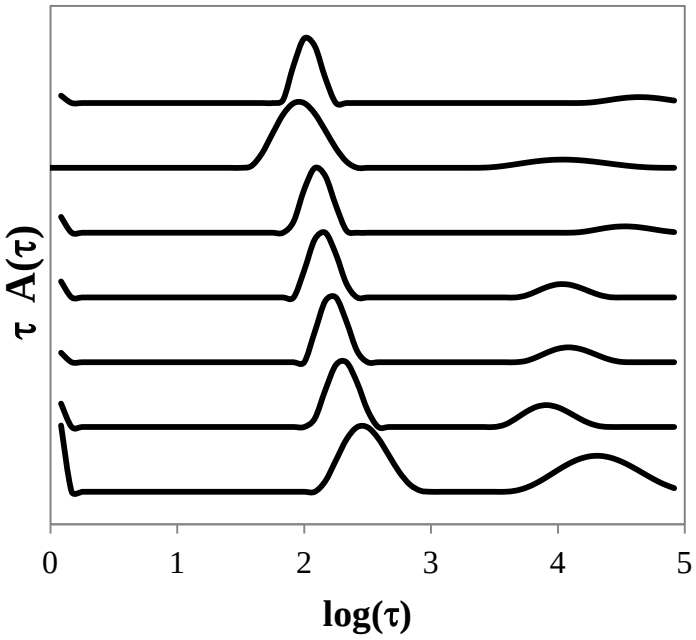

Figure B4: Distribution functions for the time decay rate of scattered light intensity by G1 PGA in DMSO measured at 150°, 135°, 120°, 105°, 90°, 75°, and 60° (top to bottom).

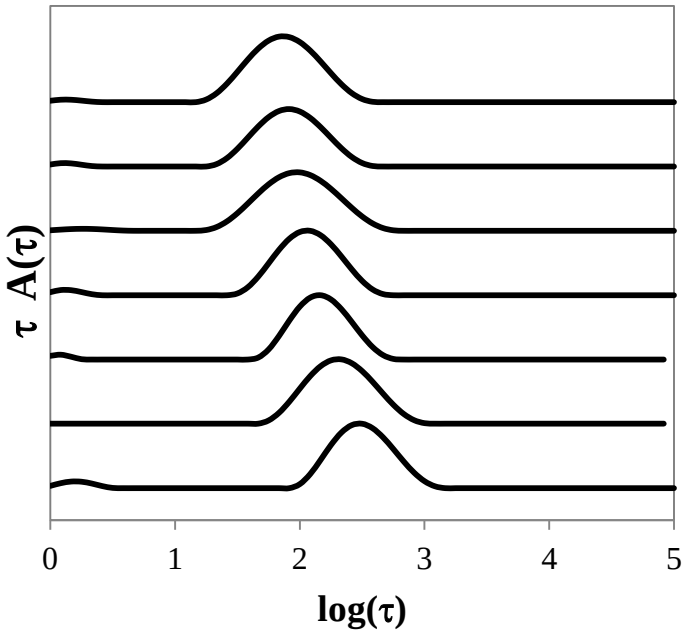

Figure B5: Distribution functions for the time decay rate of scattered light intensity by G3 PGA in DMF measured at 150°, 135°, 120°, 105°, 90°, 75°, and 60° (top to bottom).

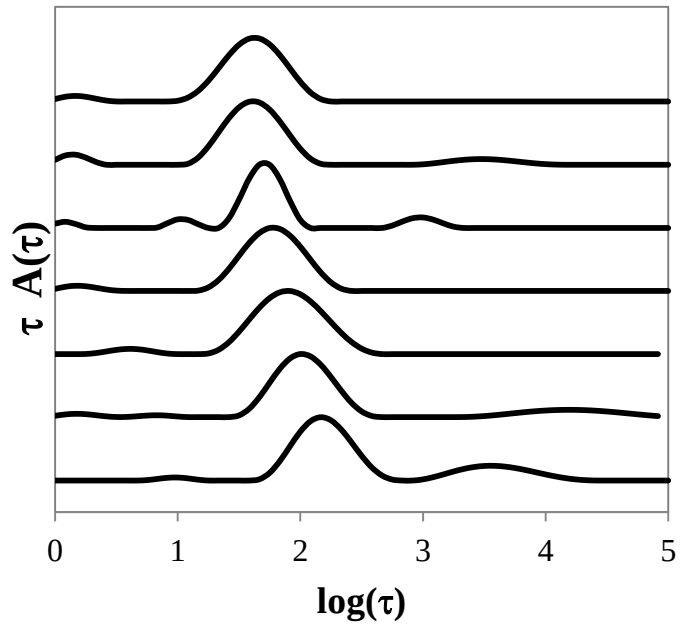

Figure B6: Distribution functions for the time decay rate of scattered light intensity by G2 PGA in DMF measured at 150°, 135°, 120°, 105°, 90°, 75°, and 60° (top to bottom).

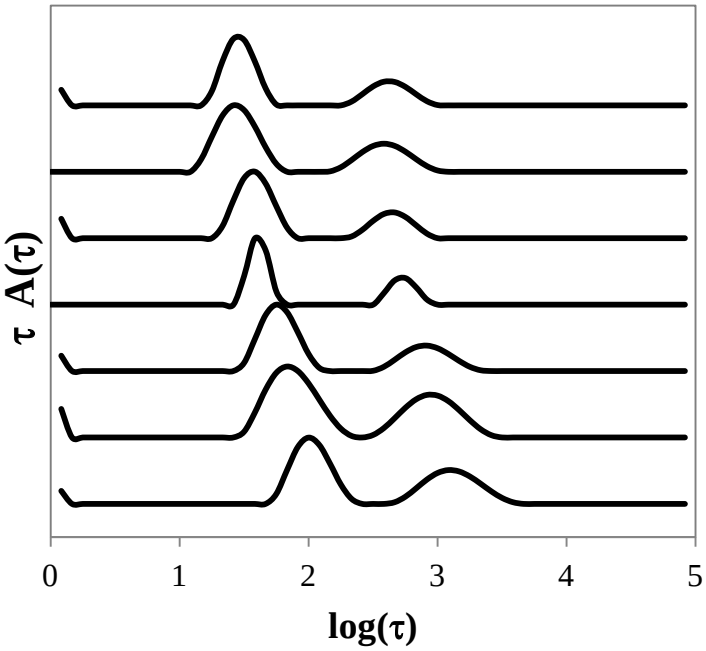

Figure B7: Distribution functions for the time decay rate of scattered light intensity by G1 PGA in DMF measured at 150°, 135°, 120°, 105°, 90°, 75°, and 60° (top to bottom).

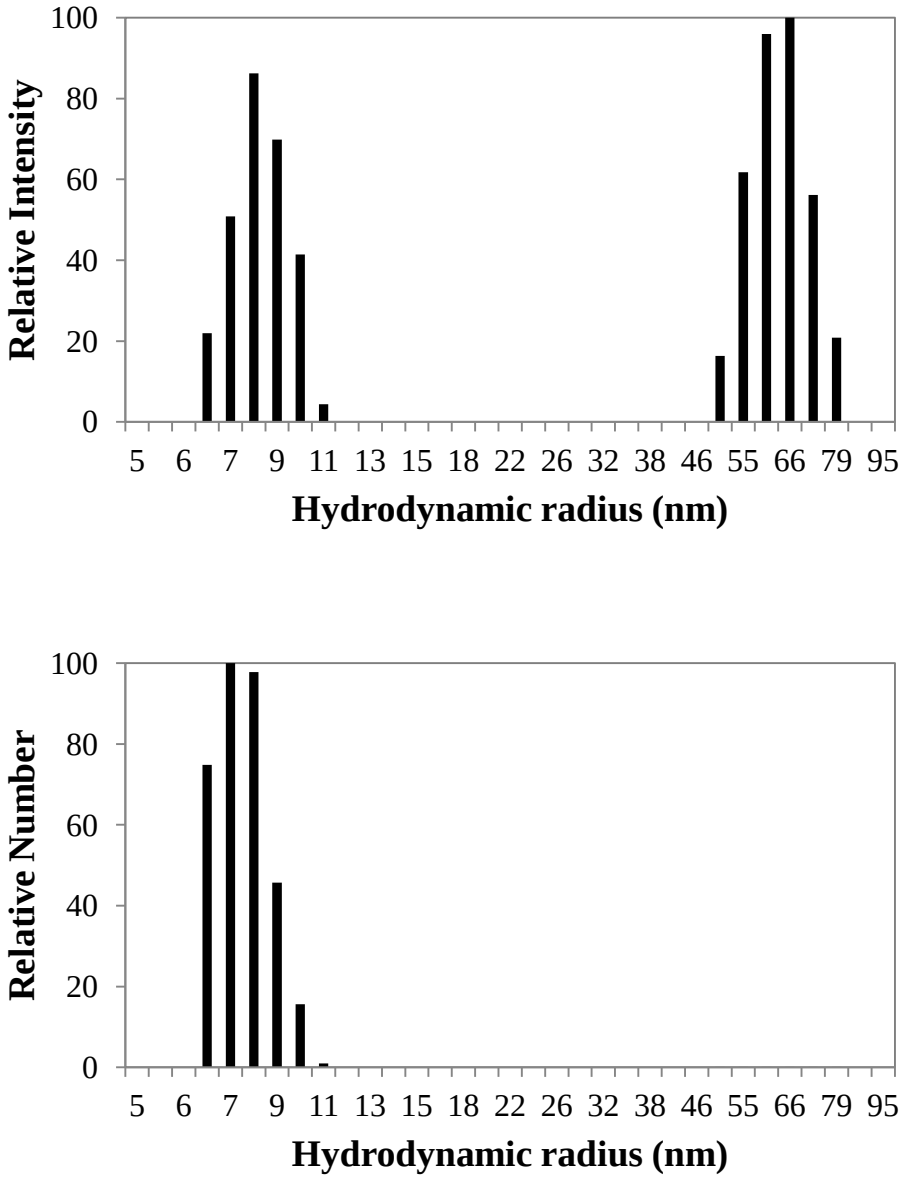

Figure B8: Hydrodynamic radius distributions for G1 PGA in DMF obtained by non-negative linear least squares analysis of the correlation functions measured at 60^{o} with signal weightings by intensity (top) and by the number of particles (bottom).

Appendix C: Birks' Scheme Parameters

Table C1: Parameters retrieved from Birks' scheme analysis of the monomer and excimer decays acquired at various concentrations of PyMeAA in DMF.

Conc. (mM)	χ^2	τ_1 (ns)	τ_2 (ns)	a_{M1}	a_{M2}	a_{E1}	a_{E2}	$k_1\times$[Py] (10^7 $s^{-1}\cdot M$)	k_{-1} (10^7 s^{-1})	τ_E (ns)
13.1	1.13	37	51	0.65	0.35	-6.08	6.10	1.97	0.07	46
11.0	1.09	39	52	0.44	0.56	-6.71	-6.72	1.72	0.06	45
9.04	1.05	40	59	0.26	0.74	-5.33	5.35	1.41	0.08	45
7.02	1.14	41	69	0.17	0.83	-3.96	3.98	1.12	0.12	47
4.94	1.14	42	84	0.10	0.90	-2.86	2.88	0.81	0.16	48

Table C2: Parameters retrieved from Birks' scheme analysis of the monomer and excimer decays acquired at various concentrations of PyMeAA in DMSO.

Conc. (mM)	χ^2	τ_1 (ns)	τ_2 (ns)	a_{M1}	a_{M2}	a_{E1}	a_{E2}	$k_1\times$[Py] (10^7 $s^{-1}\cdot M$)	k_{-1} (10^7 s^{-1})	τ_E (ns)
12.9	1.17	37	59	0.22	0.78	-4.68	4.73	1.33	0.12	43
10.9	1.23	40	69	0.17	0.83	-2.42	2.45	1.03	0.15	46
8.62	1.05	40	78	0.10	0.90	-0.97	0.99	0.83	0.17	45
6.95	1.10	41	89	0.08	0.92	-2.60	2.65	0.64	0.20	47
4.94	1.15	40	100	0.06	0.94	-0.72	0.74	0.51	0.26	47

Appendix D: Gel Permeation Chromatography Traces

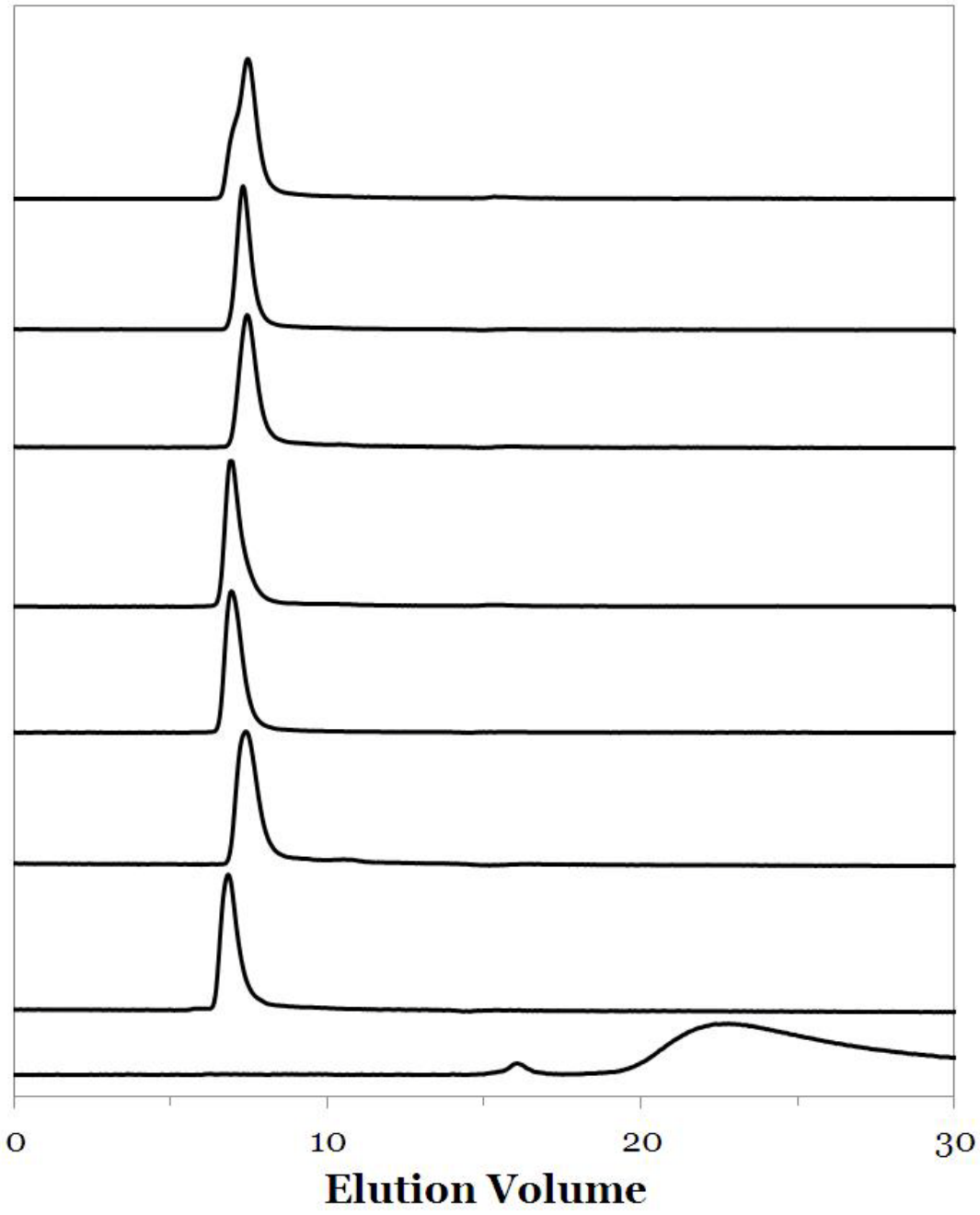

Figure D1: GPC traces monitored with a fluorescence detector (λ_{ex}= 344 nm, λ_{em}= 375 nm) for Py-Linear PGA with pyrene contents of 10, 8.1, 7.5, 6.6, 6.6, 5.0, 2.4 mol % and 1-pyrenemethylamine (top to bottom).

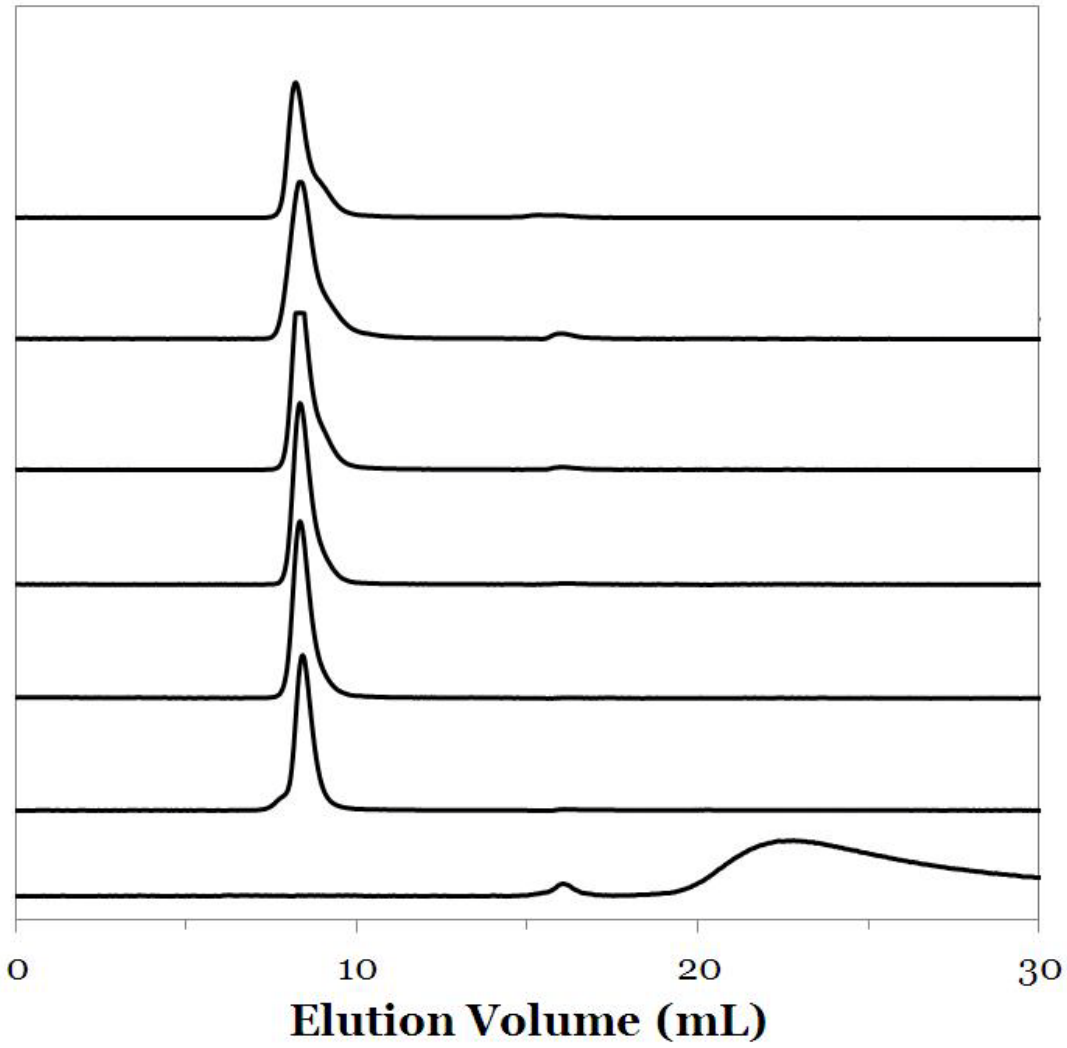

Figure D2: GPC traces monitored with a fluorescence detector (λ_{ex}= 344 nm, λ_{em}= 375 nm) for Py-G0 PGA with pyrene contents of 22, 17, 13, 11, 6.6, 4.1 mol % and 1-pyrenemethylamine (top to bottom).

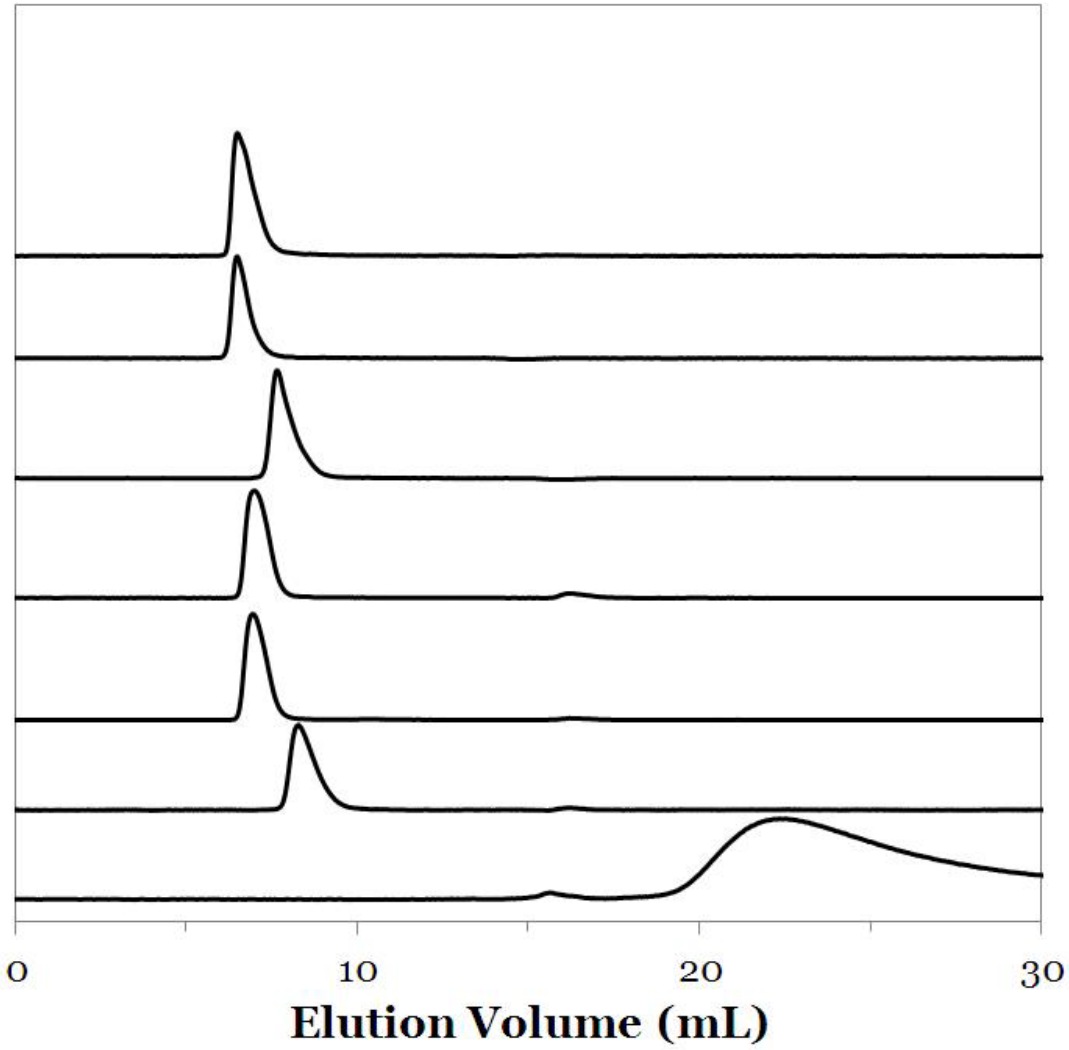

Figure D3: GPC traces monitored with a fluorescence detector (λ_{ex}= 344 nm, λ_{em}= 375 nm) for Py-G1 PGA with pyrene contents of 17, 13, 12, 7.2, 5.9, 1.3 mol % and 1-pyrenemethylamine (top to bottom).

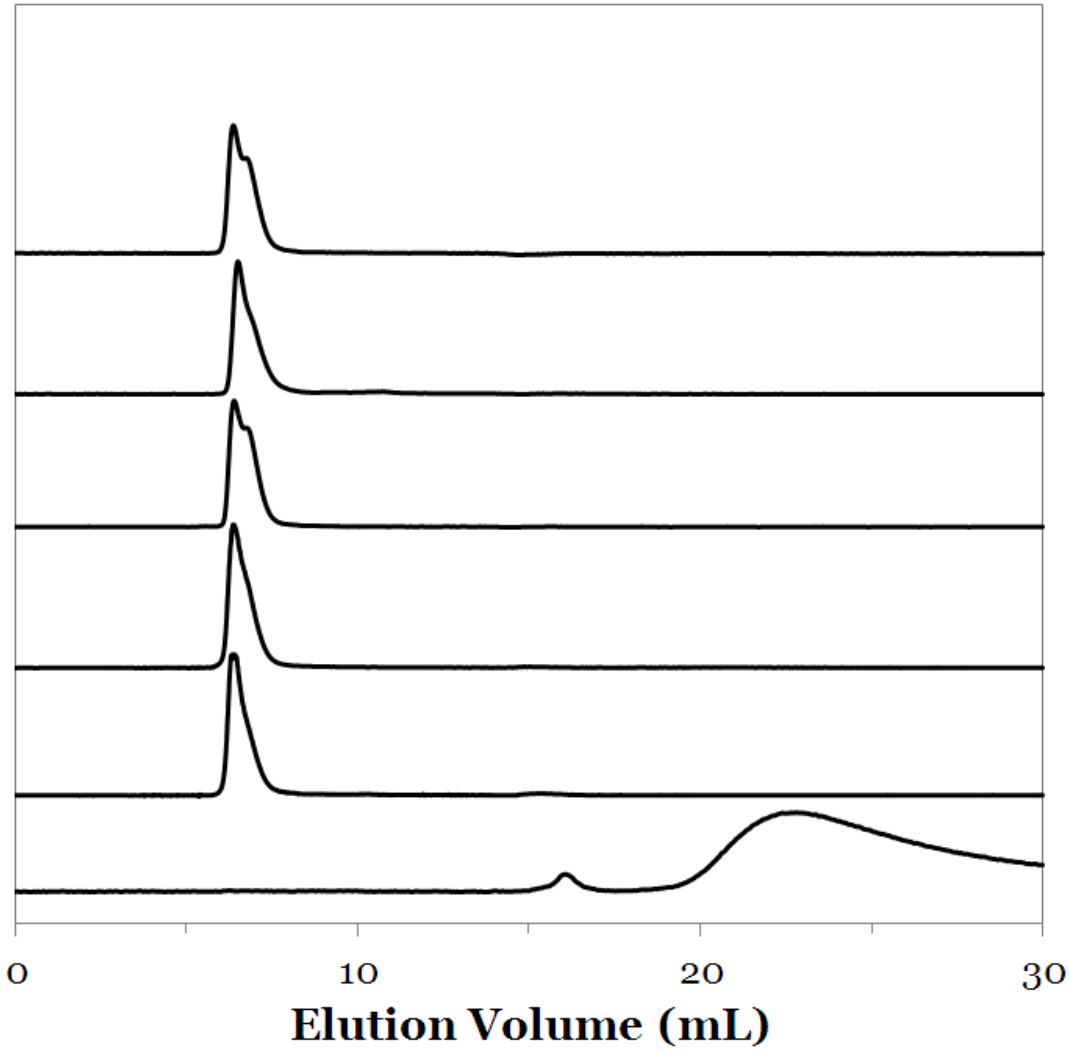

Figure D4: GPC traces monitored with a fluorescence detector (λ_{ex}= 344 nm, λ_{em}= 375 nm) for Py-G2 PGA with pyrene contents of 10, 8.7, 6.6, 4.3, 1.1 mol % and 1-pyrenemethylamine (top to bottom).

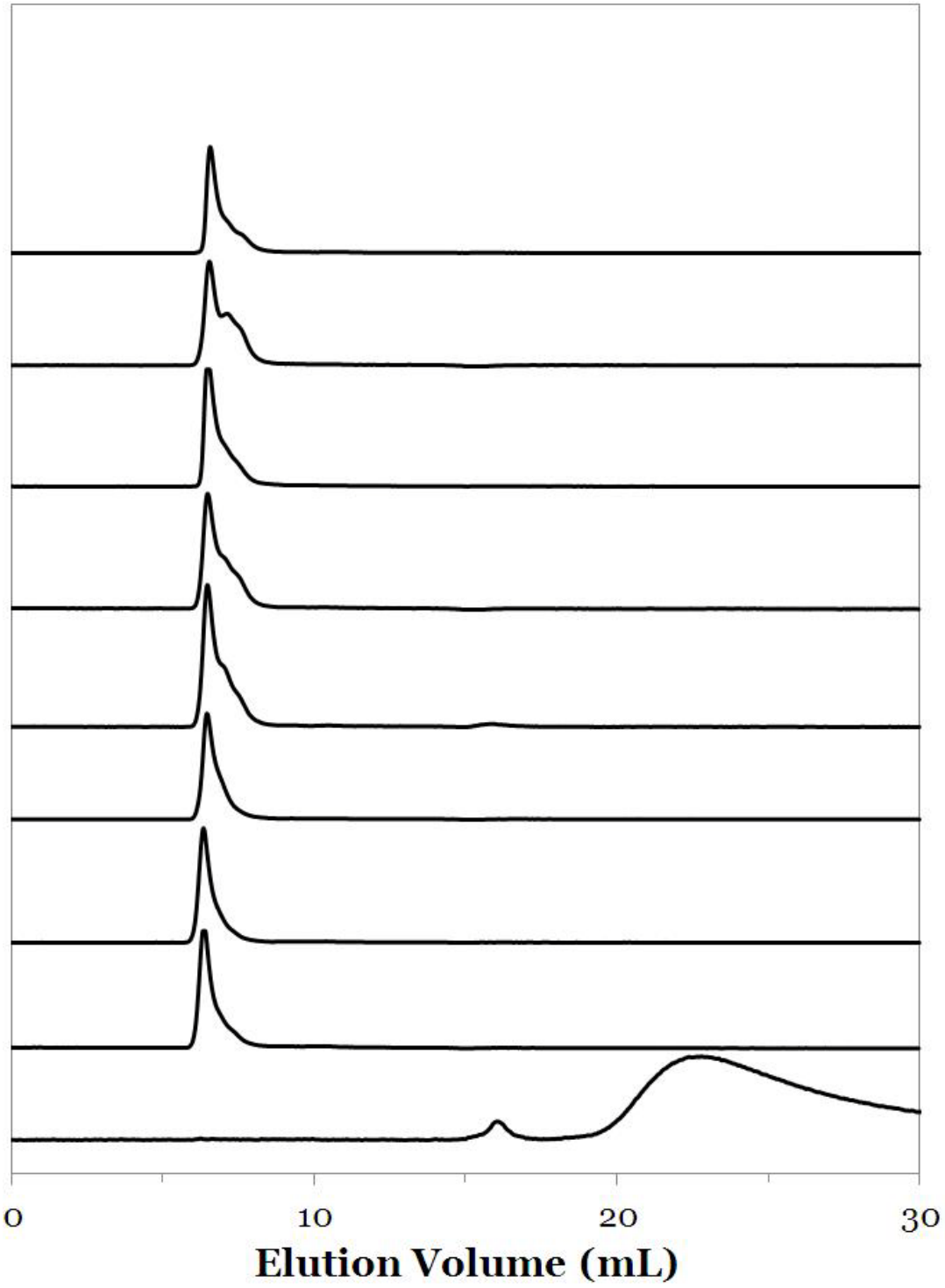

Figure D5: GPC traces monitored with a fluorescence detector (λ_{ex}= 344 nm, λ_{em}= 375 nm) for Py-G3 PGA with pyrene contents of 11, 9.4, 8.1, 6.6, 6, 5.4, 4, 2.5 mol % and 1-pyrenemethylamine (top to bottom).

Appendix E: Fluorescence Blob Model Parameters

Table E1: Parameters retrieved from FBM analysis of the monomer decays for Py-Linear PGA in DMF.

Sample	$k_e[blob]$ (10^6 s^{-1})	k_{blob} (10^7 s^{-1})	$<n>$	f_{Mdiff}	k_2 (ns^{-1})	f_{Mk_2}	τ_M (ns)	f_{Mfree}	χ^2
5.0-Lin	3.5	1.5	1.3	0.40	0.17	0.19	210	0.42	1.13
6.6-Lin	3.8	1.6	1.4	0.41	0.17	0.22	210	0.37	1.16
6.6-Lin	3.0	1.5	1.4	0.41	0.17	0.20	210	0.39	1.08
7.5-Lin	2.5	1.4	1.6	0.43	0.17	0.28	210	0.29	1.20
8.1-Lin	3.7	1.5	1.5	0.46	0.17	0.30	210	0.24	1.18
10-Lin	5.0	1.6	1.7	0.44	0.17	0.40	210	0.16	1.30
14-Lin	3.7	1.5	2.0	0.49	0.17	0.44	210	0.06	1.16
15-Lin	3.8	1.5	2.6	0.39	0.17	0.59	210	0.02	1.27

Table E2: Parameters retrieved from FBM analysis of the excimer decays for Py-Linear PGA in DMF.

Sample	f_{Ediff}^{D}	f_{Ediff}^{E0}	τ_{E0} (ns)	f_{EE0}	τ_D (ns)	f_{ED}	k_2 (ns^{-1})	f_{Ek_2}	χ^2
5.0-Lin	0.14	0.49	42	0.06	70	0.00	0.17	0.30	1.13
6.6-Lin	0.09	0.50	41	0.00	70	0.09	0.17	0.32	1.16
6.6-Lin	0.18	0.44	40	0.04	70	0.03	0.17	0.31	1.08
7.5-Lin	0.12	0.44	40	0.00	70	0.07	0.17	0.36	1.20
8.1-Lin	0.07	0.50	44	0.01	70	0.06	0.17	0.36	1.18
10-Lin	0.03	0.44	44	0.04	70	0.06	0.17	0.43	1.30
14-Lin	0.07	0.41	44	0.03	70	0.06	0.17	0.43	1.16
15-Lin	0.02	0.32	44	0.04	70	0.12	0.17	0.51	1.27

Table E3: Fractions of the different pyrene species retrieved from FBM analysis of Py-Linear PGA in DMF.

Sample	f_{diff}^{E0}	f_{diff}^{D}	f_{E0}	f_D	f_{free}	f_{k_2}
5.0-Lin	0.29	0.09	0.04	0.00	0.40	0.18
6.6-Lin	0.32	0.06	0.00	0.06	0.35	0.21
6.6-Lin	0.28	0.11	0.03	0.02	0.37	0.19
7.5-Lin	0.32	0.09	0.00	0.05	0.28	0.26
8.1-Lin	0.38	0.05	0.01	0.05	0.23	0.28
10-Lin	0.38	0.02	0.03	0.05	0.15	0.37
14-Lin	0.38	0.07	0.02	0.06	0.06	0.41
15-Lin	0.31	0.02	0.04	0.11	0.02	0.50

Table E4: Parameters retrieved from FBM analysis of the monomer decays for Py-Linear PGA in DMSO.

Sample	$k_e[blob]$ (10^6 s^{-1})	k_{blob} (10^7 s^{-1})	$<n>$	f_{Mdiff}	k_2 (ns^{-1})	f_{Mk_2}	τ_M (ns)	f_{Mfree}	χ^2
5.0-Lin	3.9	1.3	1.2	0.45	0.12	0.14	170	0.41	1.02
6.6-Lin	3.1	1.2	1.5	0.46	0.12	0.19	170	0.35	1.09
6.6-Lin	3.9	1.5	1.3	0.46	0.12	0.18	170	0.36	1.05
7.5-Lin	4.7	1.2	1.6	0.50	0.12	0.21	170	0.28	1.11
8.1-Lin	4.0	1.3	1.4	0.53	0.12	0.25	170	0.22	1.15
10-Lin	4.1	1.2	1.8	0.49	0.12	0.34	170	0.17	1.04
14-Lin	3.3	1.1	1.9	0.53	0.12	0.38	170	0.09	1.17
15-Lin	3.5	1.1	2.6	0.43	0.12	0.55	170	0.02	1.25

Table E5: Parameters retrieved from FBM analysis of the excimer decays for Py-Linear PGA in DMSO.

Sample	f_{Ediff}^{D}	f_{Ediff}^{E0}	τ_{E0} (ns)	f_{EE0}	τ_{D} (ns)	f_{ED}	k_2 (ns^{-1})	f_{Ek_2}	χ^2
5.0-Lin	0.06	0.64	44	0.00	70	0.08	0.12	0.21	1.02
6.6-Lin	0.11	0.54	43	0.02	70	0.06	0.12	0.27	1.09
6.6-Lin	0.13	0.52	47	0.08	70	0.03	0.12	0.25	1.05
7.5-Lin	0.06	0.60	44	0.05	70	0.01	0.12	0.28	1.11
8.1-Lin	0.00	0.62	46	0.02	70	0.07	0.12	0.29	1.15
10-Lin	0.00	0.54	43	0.03	70	0.06	0.12	0.38	1.04
14-Lin	0.03	0.50	41	0.00	70	0.09	0.12	0.38	1.17
15-Lin	0.00	0.38	40	0.05	70	0.08	0.12	0.49	1.25

Table E6: Fractions of the different pyrene species retrieved from FBM analysis of Py-Linear PGA in DMSO.

Sample	f_{diff}^{E0}	f_{diff}^{D}	f_{E0}	f_{D}	f_{free}	f_{k_2}
5.0-Lin	0.39	0.04	0.00	0.05	0.39	0.13
6.6-Lin	0.36	0.07	0.02	0.04	0.33	0.18
6.6-Lin	0.34	0.09	0.05	0.02	0.34	0.16
7.5-Lin	0.44	0.04	0.04	0.01	0.27	0.20
8.1-Lin	0.49	0.00	0.01	0.06	0.21	0.23
10-Lin	0.46	0.00	0.02	0.05	0.16	0.32
14-Lin	0.46	0.02	0.00	0.09	0.08	0.34
15-Lin	0.38	0.00	0.05	0.07	0.02	0.48

Table E7: Parameters retrieved from FBM analysis of the monomer decays for Py-G0 PGA in DMF.

Sample	$k_e[blob]$ (10^6 s^{-1})	k_{blob} (10^7 s^{-1})	<n>	f_{Mdiff}	k_2 (ns^{-1})	f_{Mk_2}	τ_M (ns)	f_{Mfree}	χ^2
4.1-G0	2.4	1.2	1.1	0.56	0.17	0.15	210	0.29	1.09
6.6-G0	3.5	1.6	1.4	0.55	0.17	0.34	210	0.11	1.25
11-G0	3.4	1.6	2.0	0.48	0.17	0.46	210	0.06	1.16
13-G0	3.7	1.5	2.1	0.49	0.17	0.47	210	0.04	1.15
17-G0	3.0	1.5	2.9	0.37	0.17	0.60	210	0.02	1.30
22-G0	2.4	1.3	3.9	0.24	0.17	0.75	210	0.01	1.18

Table E8: Parameters retrieved from FBM analysis of the excimer decays for Py-G0 PGA in DMF.

Sample	f_{Ediff}^{D}	f_{Ediff}^{E0}	τ_{E0} (ns)	f_{EE0}	τ_D (ns)	f_{ED}	k_2 (ns^{-1})	f_{Ek_2}	χ^2
4.1-G0	0.19	0.59	31	0.01	70	0.01	0.17	0.20	1.09
6.6-G0	0.09	0.48	42	0.01	70	0.07	0.17	0.35	1.25
11-G0	0.05	0.39	43	0.02	70	0.10	0.17	0.43	1.16
13-G0	0.06	0.39	43	0.06	70	0.06	0.17	0.43	1.15
17-G0	0.01	0.29	42	0.00	70	0.21	0.17	0.49	1.30
22-G0	0.01	0.17	43	0.03	70	0.23	0.17	0.57	1.18

Table E9: Fractions of the different pyrene species retrieved from FBM analysis of Py-G0 PGA in DMF.

Sample	f_{diff}^{E0}	f_{diff}^{D}	f_{E0}	f_D	f_{free}	f_{k_2}
4.1-G0	0.42	0.13	0.01	0.01	0.29	0.15
6.6-G0	0.43	0.08	0.01	0.06	0.11	0.32
11-G0	0.37	0.05	0.02	0.09	0.05	0.41
13-G0	0.38	0.06	0.06	0.05	0.03	0.42
17-G0	0.29	0.01	0.00	0.20	0.02	0.48
22-G0	0.17	0.01	0.03	0.23	0.01	0.56

Table E10: Parameters retrieved from FBM analysis of the monomer decays for Py-G0 PGA in DMSO.

Sample	$k_e[blob]$ (10^6 s^{-1})	k_{blob} (10^7 s^{-1})	$<n>$	f_{Mdiff}	k_2 (ns^{-1})	f_{Mk_2}	τ_M (ns)	f_{Mfree}	χ^2
4.1-G0	3.4	1.0	1.0	0.67	0.12	0.13	170	0.21	1.17
6.6-G0	3.9	1.2	1.4	0.66	0.12	0.25	170	0.09	1.20
11-G0	4.4	1.2	2.0	0.58	0.12	0.36	170	0.06	1.05
13-G0	5.1	1.3	2.0	0.58	0.12	0.39	170	0.03	1.10
17-G0	2.4	1.1	2.8	0.48	0.12	0.49	170	0.03	1.18
22-G0	1.0	0.9	4.1	0.26	0.12	0.73	170	0.00	1.26

Table E11: Parameters retrieved from FBM analysis of the excimer decays for Py-G0 PGA in DMSO.

Sample	f_{Ediff}^{D}	f_{Ediff}^{E0}	τ_{E0} (ns)	f_{EE0}	τ_D (ns)	f_{ED}	k_2 (ns^{-1})	f_{Ek_2}	χ^2
4.1-G0	0.15	0.57	43	0.01	70	0.09	0.12	0.18	1.17
6.6-G0	0.05	0.63	43	0.00	70	0.06	0.12	0.26	1.20
11-G0	0.02	0.55	44	0.05	70	0.03	0.12	0.35	1.05
13-G0	0.00	0.54	45	0.03	70	0.06	0.12	0.36	1.10
17-G0	0.00	0.45	43	0.01	70	0.09	0.12	0.45	1.18
22-G0	0.00	0.19	43	0.09	70	0.16	0.12	0.56	1.26

Table E12: Fractions of the different pyrene species retrieved from FBM analysis of Py-G0 PGA in DMSO.

Sample	f_{diff}^{E0}	f_{diff}^{D}	f_{E0}	f_D	f_{free}	f_{k_2}
4.1-G0	0.48	0.13	0.01	0.08	0.19	0.12
6.6-G0	0.57	0.05	0.00	0.06	0.09	0.23
11-G0	0.51	0.02	0.05	0.03	0.06	0.33
13-G0	0.52	0.00	0.03	0.06	0.03	0.35
17-G0	0.44	0.00	0.01	0.09	0.02	0.44
22-G0	0.19	0.00	0.09	0.16	0.00	0.55

Table E13: Parameters retrieved from FBM analysis of the monomer decays for Py-G1 PGA in DMF.

Sample	$k_e[blob]$ (10^6 s^{-1})	k_{blob} (10^7 s^{-1})	$<n>$	f_{Mdiff}	k_2 (ns^{-1})	f_{Mk_2}	τ_M (ns)	f_{Mfree}	χ^2
5.9-G1	3.4	1.5	1.4	0.58	0.17	0.26	210	0.16	1.01
7.2-G1	2.9	1.5	1.5	0.60	0.17	0.28	210	0.13	1.03
12-G1	2.7	1.4	2.5	0.51	0.17	0.46	210	0.04	1.16
13-G1	3.5	1.4	2.4	0.46	0.17	0.51	210	0.04	1.27
17-G1	2.2	1.5	2.9	0.34	0.17	0.65	210	0.01	1.08

Table E14: Parameters retrieved from FBM analysis of the excimer decays for Py-G1 PGA in DMF.

Sample	f_{Ediff}^{D}	f_{Ediff}^{E0}	τ_{E0} (ns)	f_{EE0}	τ_D (ns)	f_{ED}	k_2 (ns^{-1})	f_{Ek_2}	χ^2
5.9-G1	0.21	0.41	41	0.05	70	0.05	0.17	0.28	1.01
7.2-G1	0.19	0.39	38	0.02	70	0.12	0.17	0.27	1.03
12-G1	0.10	0.34	44	0.15	70	0.00	0.17	0.40	1.16
13-G1	0.06	0.35	41	0.03	70	0.11	0.17	0.45	1.27
17-G1	0.03	0.24	41	0.09	70	0.14	0.17	0.50	1.08

Table E15: Fractions of the different pyrene species retrieved from FBM analysis of Py-G1 PGA in DMF.

Sample	f_{diff}^{E0}	f_{diff}^{D}	f_{E0}	f_D	f_{free}	f_{k_2}
5.9-G1	0.36	0.18	0.04	0.05	0.14	0.24
7.2-G1	0.35	0.17	0.02	0.11	0.11	0.24
12-G1	0.33	0.10	0.14	0.00	0.03	0.39
13-G1	0.34	0.06	0.03	0.11	0.03	0.44
17-G1	0.23	0.03	0.09	0.14	0.01	0.49

Table E16: Parameters retrieved from FBM analysis of the monomer decays for Py-G1 PGA in DMSO.

Sample	$k_e[blob]$ (10^6 s^{-1})	k_{blob} (10^7 s^{-1})	$<n>$	f_{Mdiff}	k_2 (ns^{-1})	f_{Mk_2}	τ_M (ns)	f_{Mfree}	χ^2
5.9-G1	3.3	0.9	1.5	0.65	0.12	0.19	170	0.16	1.13
7.2-G1	3.3	1.0	1.8	0.65	0.12	0.26	170	0.10	1.12
12-G1	1.6	0.8	3.0	0.49	0.12	0.48	170	0.03	1.13
13-G1	2.7	1.0	2.7	0.49	0.12	0.49	170	0.02	1.17
17-G1	0.9	1.0	3.3	0.37	0.12	0.62	170	0.01	1.17

Table E17: Parameters retrieved from FBM analysis of the excimer decays for Py-G1 PGA in DMSO.

Sample	f_{Ediff}^{D}	f_{Ediff}^{E0}	τ_{E0} (ns)	f_{EE0}	τ_D (ns)	f_{ED}	k_2 (ns^{-1})	f_{Ek_2}	χ^2
5.9-G1	0.12	0.59	39	0.00	70	0.09	0.12	0.20	1.13
7.2-G1	0.09	0.56	44	0.05	70	0.04	0.12	0.26	1.12
12-G1	0.01	0.40	42	0.01	70	0.16	0.12	0.41	1.13
13-G1	0.00	0.43	41	0.03	70	0.11	0.12	0.43	1.17
17-G1	0.03	0.27	41	0.09	70	0.11	0.12	0.50	1.17

Table E18: Fractions of the different pyrene species retrieved from FBM analysis of Py-G1 PGA in DMSO.

Sample	f_{diff}^{E0}	f_{diff}^{D}	f_{E0}	f_D	f_{free}	f_{k_2}
5.9-G1	0.50	0.10	0.00	0.07	0.15	0.17
7.2-G1	0.51	0.08	0.04	0.04	0.09	0.24
12-G1	0.40	0.01	0.01	0.16	0.02	0.40
13-G1	0.42	0.00	0.03	0.11	0.02	0.43
17-G1	0.27	0.03	0.09	0.11	0.01	0.50

Table E19: Parameters retrieved from FBM analysis of the monomer decays for Py-G2 PGA in DMF.

Sample	$k_e[blob]$ (10^6 s^{-1})	k_{blob} (10^7 s^{-1})	<n>	f_{Mdiff}	k_2 (ns^{-1})	f_{Mk_2}	τ_M (ns)	f_{Mfree}	χ^2
4.3-G2	3.3	1.2	1.3	0.66	0.17	0.20	210	0.15	1.07
6.6-G2	2.8	1.2	1.9	0.59	0.17	0.34	210	0.07	1.11
8.7-G2	2.5	1.1	2.3	0.56	0.17	0.39	210	0.05	1.09
10-G2	2.8	1.2	2.4	0.54	0.17	0.41	210	0.04	1.15
14-G2	1.1	1.4	3.3	0.27	0.17	0.72	210	0.01	1.13

Table E20: Parameters retrieved from FBM analysis of the excimer decays for Py-G2 PGA in DMF.

Sample	f_{Ediff}^{D}	f_{Ediff}^{E0}	τ_{E0} (ns)	f_{EE0}	τ_D (ns)	f_{ED}	k_2 (ns^{-1})	f_{Ek_2}	χ^2
4.3-G2	0.22	0.50	36	0.05	70	0.01	0.17	0.22	1.07
6.6-G2	0.14	0.44	40	0.02	70	0.07	0.17	0.33	1.11
8.7-G2	0.11	0.42	41	0.04	70	0.06	0.17	0.37	1.09
10-G2	0.11	0.39	41	0.03	70	0.09	0.17	0.38	1.15
14-G2	0.05	0.16	43	0.17	70	0.04	0.17	0.57	1.13

Table E21: Fractions of the different pyrene species retrieved from FBM analysis of Py-G2 PGA in DMF.

Sample	f_{diff}^{E0}	f_{diff}^{D}	f_{E0}	f_D	f_{free}	f_{k_2}
4.3-G2	0.43	0.19	0.04	0.01	0.14	0.19
6.6-G2	0.41	0.13	0.02	0.07	0.06	0.31
8.7-G2	0.40	0.11	0.04	0.06	0.04	0.35
10-G2	0.38	0.10	0.03	0.09	0.04	0.36
14-G2	0.16	0.05	0.17	0.04	0.01	0.56

Table E22: Parameters retrieved from FBM analysis of the monomer decays for Py-G2 PGA in DMSO.

Sample	$k_e[blob]$ (10^6 s^{-1})	k_{blob} (10^7 s^{-1})	$<n>$	f_{Mdiff}	k_2 (ns^{-1})	f_{Mk_2}	τ_M (ns)	f_{Mfree}	χ^2
4.3-G2	4.7	1.0	1.3	0.72	0.12	0.18	170	0.09	1.10
6.6-G2	3.0	1.0	2.1	0.64	0.12	0.32	170	0.04	1.10
8.7-G2	3.7	1.0	2.3	0.59	0.12	0.37	170	0.04	1.03
10-G2	2.3	1.0	2.6	0.53	0.12	0.44	170	0.03	1.12
14-G2	0.4	0.9	4.1	0.31	0.12	0.68	170	0.01	1.15

Table E23: Parameters retrieved from FBM analysis of the excimer decays for Py-G2 PGA in DMSO.

Sample	f_{Ediff}^{D}	f_{Ediff}^{E0}	τ_{E0} (ns)	f_{EE0}	τ_D (ns)	f_{ED}	k_2 (ns^{-1})	f_{Ek_2}	χ^2
4.3-G2	0.14	0.60	43	0.00	70	0.07	0.12	0.19	1.10
6.6-G2	0.07	0.55	42	0.03	70	0.06	0.12	0.31	1.10
8.7-G2	0.05	0.49	43	0.06	70	0.05	0.12	0.34	1.03
10-G2	0.02	0.45	43	0.05	70	0.08	0.12	0.39	1.12
14-G2	0.03	0.22	42	0.16	70	0.04	0.12	0.55	1.15

Table E24: Fractions of the different pyrene species retrieved from FBM analysis of Py-G2 PGA in DMSO.

Sample	f_{diff}^{E0}	f_{diff}^{D}	f_{E0}	f_D	f_{free}	f_{k_2}
4.3-G2	0.54	0.13	0.00	0.07	0.09	0.17
6.6-G2	0.52	0.06	0.03	0.05	0.04	0.29
8.7-G2	0.48	0.05	0.06	0.05	0.03	0.33
10-G2	0.44	0.02	0.05	0.08	0.02	0.39
14-G2	0.22	0.03	0.16	0.04	0.01	0.55

Table E25: Parameters retrieved from FBM analysis of the monomer decays for Py-G3 PGA in DMF.

Sample	$k_e[blob]$ (10^6 s^{-1})	k_{blob} (10^7 s^{-1})	<n>	f_{Mdiff}	k_2 (ns^{-1})	f_{Mk_2}	τ_M (ns)	f_{Mfree}	χ^2
2.5-G3	2.9	1.2	1.0	0.62	0.17	0.12	210	0.26	1.06
4.0-G3	2.8	1.1	1.0	0.71	0.17	0.14	210	0.15	1.09
5.4-G3	4.0	1.1	1.6	0.64	0.17	0.26	210	0.10	1.26
6.0-G3	3.4	1.1	1.9	0.65	0.17	0.27	210	0.08	1.13
6.6-G3	3.7	1.0	2.0	0.65	0.17	0.28	210	0.07	1.13
8.1-G3	3.4	1.1	2.3	0.58	0.17	0.37	210	0.06	1.08
9.4-G3	2.8	1.2	2.7	0.52	0.17	0.44	210	0.05	0.99
11-G3	2.0	1.2	3.1	0.43	0.17	0.56	210	0.02	1.10

Table E26: Parameters retrieved from FBM analysis of the excimer decays for Py-G3 PGA in DMF.

Sample	f_{Ediff}^{D}	f_{Ediff}^{E0}	τ_{E0} (ns)	f_{EE0}	τ_D (ns)	f_{ED}	k_2 (ns^{-1})	f_{Ek_2}	χ^2
2.5-G3	0.27	0.54	30	0.03	70	0.01	0.17	0.15	1.06
4.0-G3	0.27	0.53	32	0.03	70	0.01	0.17	0.16	1.09
5.4-G3	0.14	0.52	39	0.01	70	0.05	0.17	0.27	1.26
6.0-G3	0.20	0.45	40	0.05	70	0.02	0.17	0.27	1.13
6.6-G3	0.14	0.50	39	0.01	70	0.07	0.17	0.28	1.13
8.1-G3	0.11	0.45	40	0.05	70	0.04	0.17	0.35	1.08
9.4-G3	0.08	0.40	42	0.04	70	0.08	0.17	0.41	0.99
11-G3	0.03	0.33	42	0.00	70	0.16	0.17	0.47	1.10

Table E27: Fractions of the different pyrene species retrieved from FBM analysis of Py-G3 PGA in DMF.

Sample	f_{diff}^{E0}	f_{diff}^{D}	f_{E0}	f_D	f_{free}	f_{k_2}
2.5-G3	0.40	0.20	0.02	0.01	0.26	0.11
4.0-G3	0.45	0.23	0.02	0.01	0.15	0.14
5.4-G3	0.48	0.13	0.01	0.05	0.09	0.25
6.0-G3	0.42	0.19	0.04	0.02	0.08	0.25
6.6-G3	0.47	0.13	0.01	0.07	0.06	0.26
8.1-G3	0.42	0.10	0.05	0.04	0.05	0.33
9.4-G3	0.38	0.08	0.04	0.07	0.04	0.39
11-G3	0.38	0.09	0.05	0.05	0.04	0.38

Table E28: Parameters retrieved from FBM analysis of the monomer decays for Py-G3 PGA in DMSO.

Sample	$k_e[blob]$ (10^6 s^{-1})	k_{blob} (10^7 s^{-1})	<n>	f_{Mdiff}	k_2 (ns^{-1})	f_{Mk_2}	τ_M (ns)	f_{Mfree}	χ^2
2.5-G3	4.0	0.8	1.0	0.71	0.12	0.10	170	0.18	1.19
4.0-G3	4.0	0.7	1.5	0.74	0.12	0.12	170	0.15	1.20
5.4-G3	4.3	0.8	2.0	0.72	0.12	0.21	170	0.07	1.15
6.0-G3	4.4	0.7	2.2	0.70	0.12	0.23	170	0.07	1.16
6.6-G3	3.9	0.8	2.4	0.67	0.12	0.28	170	0.05	1.06
8.1-G3	3.6	0.8	2.7	0.63	0.12	0.33	170	0.04	0.99
9.4-G3	2.4	0.9	3.1	0.54	0.12	0.43	170	0.04	1.09
11-G3	0.9	0.9	3.6	0.37	0.12	0.61	170	0.01	1.07

Table E29: Parameters retrieved from FBM analysis of the excimer decays for Py-G3 PGA in DMSO.

Sample	f_{Ediff}^{D}	f_{Ediff}^{E0}	τ_{E0} (ns)	f_{EE0}	τ_{D} (ns)	f_{ED}	k_2 (ns^{-1})	f_{Ek_2}	χ^2
2.5-G3	0.20	0.63	41	0.00	70	0.05	0.12	0.12	1.19
4.0-G3	0.18	0.63	38	0.00	70	0.05	0.12	0.13	1.20
5.4-G3	0.07	0.66	42	0.00	70	0.06	0.12	0.21	1.15
6.0-G3	0.05	0.66	43	0.01	70	0.04	0.12	0.23	1.16
6.6-G3	0.05	0.61	41	0.00	70	0.06	0.12	0.28	1.06
8.1-G3	0.03	0.57	41	0.01	70	0.06	0.12	0.32	0.99
9.4-G3	0.04	0.46	43	0.07	70	0.03	0.12	0.40	1.09
11-G3	0.02	0.30	41	0.13	70	0.02	0.12	0.53	1.07

Table E30: Fractions of the different pyrene species retrieved from FBM analysis of Py-G3 PGA in DMSO.

Sample	f_{diff}^{E0}	f_{diff}^{D}	f_{E0}	f_{D}	f_{free}	f_{k_2}
2.5-G3	0.52	0.17	0.00	0.04	0.18	0.10
4.0-G3	0.54	0.16	0.00	0.05	0.14	0.11
5.4-G3	0.61	0.07	0.00	0.05	0.07	0.20
6.0-G3	0.61	0.05	0.01	0.04	0.07	0.22
6.6-G3	0.58	0.05	0.00	0.06	0.05	0.26
8.1-G3	0.55	0.03	0.01	0.06	0.04	0.31
9.4-G3	0.44	0.04	0.07	0.03	0.03	0.39
11-G3	0.50	0.02	0.01	0.08	0.03	0.36

Appendix F: Sum of Exponentials Analysis Parameters

Table F1: Parameters retrieved by fitting the monomer decays for Py-Linear PGA samples in DMF to a sum of exponentials equation.

Sample	τ_1 (ns)	A_1	τ_2 (ns)	A_2	τ_3 (ns)	A_3	χ^2
2.4-Lin	11	0.2	58	0.2	209	0.6	1.09
5.0-Lin	15	0.2	69	0.2	201	0.5	1.01
6.6-Lin	12	0.3	54	0.2	194	0.5	1.01
6.6-Lin	13	0.3	62	0.2	202	0.5	1.14
7.5-Lin	11	0.3	56	0.3	198	0.4	1.07
8.1-Lin	12	0.4	55	0.3	191	0.4	1.11
10-Lin	11	0.5	51	0.3	191	0.2	1.07
14-Lin	12	-0.5	47	0.3	168	0.1	1.18
15-Lin	9	0.7	37	0.3	151	0.1	1.18

Table F2: Parameters retrieved by fitting the excimer decays for Py-Linear PGA samples in DMF to a sum of exponentials equation.

Sample	τ_1 (ns)	A_1	τ_2 (ns)	A_2	τ_3 (ns)	A_3	τ_4 (ns)	A_4	χ^2
2.4-Lin	9	-2.2	20	-2.8	62	5.6	152	0.4	1.05
5.0-Lin	5	-2.3	17	-6.6	61	9.0	132	0.8	0.97
6.6-Lin	1	-2.8	17	-7.0	58	9.8	120	1.0	1.13
6.6-Lin	6	-3.1	20	-5.6	59	8.8	127	0.9	1.08
7.5-Lin	4	-3.0	15	-8.1	60	11.3	131	0.7	1.09
8.1-Lin	4	-3.1	16	-7.6	60	11.1	129	0.7	1.15
10-Lin	3	-3.1	13	-7.9	56	11.4	112	0.6	1.17
14-Lin	3	-3.2	14	-9.1	58	12.8	117	0.6	1.04
15-Lin	3	-2.9	12	-6.3	51	9.3	81	0.8	1.11

Table F3: Parameters retrieved by fitting the monomer decays for Py-Linear PGA samples in DMSO to a sum of exponentials equation.

Sample	τ_1 (ns)	A_1	τ_2 (ns)	A_2	τ_3 (ns)	A_3	χ^2
2.4-Lin	17	0.2	74	0.2	172	0.6	1.00
5.0-Lin	16	0.2	62	0.3	163	0.5	1.02
6.6-Lin	15	0.3	57	0.3	163	0.4	1.06
6.6-Lin	12	0.3	56	0.3	163	0.4	0.95
7.5-Lin	13	0.3	58	0.4	162	0.3	1.16
8.1-Lin	13	0.3	53	0.3	155	0.3	1.14
10-Lin	13	0.4	49	0.4	153	0.3	1.00
14-Lin	10	0.4	43	0.4	145	0.2	1.07
15-Lin	10	0.5	34	0.4	114	0.1	1.21

Table F4: Parameters retrieved by fitting the excimer decays for Py-Linear PGA samples in DMSO to a sum of exponentials equation.

Sample	τ_1 (ns)	A_1	τ_2 (ns)	A_2	τ_3 (ns)	A_3	τ_4 (ns)	A_4	χ^2
2.4-Lin	13	-2.0	32	-6.1	53	7.9	105	1.2	1.18
5.0-Lin	12	-2.7	36	-15.3	46	17.4	101	1.7	1.04
6.6-Lin	8	-1.5	22	-6.8	58	8.5	111	0.8	1.08
6.6-Lin	12	-2.2	28	-5.0	56	7.1	105	1.1	1.07
7.5-Lin	8	-2.7	23	-10.1	55	12.1	99	1.8	1.11
8.1-Lin	8	-2.2	25	-6.3	54	8.6	104	0.9	1.14
10-Lin	6	-2.5	19	-8.3	54	11.2	103	0.6	1.03
14-Lin	8	-3.6	22	-6.4	51	9.5	87	1.5	1.08
15-Lin	7	-3.2	23	-8.8	33	7.4	58	5.6	1.16

Table F5: Parameters retrieved by fitting the monomer decays for Py-G0 PGA samples in DMF to a sum of exponentials equation.

Sample	τ_1 (ns)	A_1	τ_2 (ns)	A_2	τ_3 (ns)	A_3	χ^2
4.1-G0	18	0.3	79	0.3	198	0.4	1.05
6.6-G0	10	0.6	42	0.3	154	0.1	1.18
11-G0	12	0.6	50	0.3	175	0.1	1.25
13-G0	13	0.5	60	0.3	178	0.2	1.19
17-G0	8	0.7	31	0.3	154	0.1	1.33
22-G0	7	0.8	27	0.2	148	0.0	1.17

Table F6: Parameters retrieved by fitting the excimer decays for Py-G0 PGA samples in DMF to a sum of exponentials equation.

Sample	τ_1 (ns)	A_1	τ_2 (ns)	A_2	τ_3 (ns)	A_3	τ_4 (ns)	A_4	χ^2
4.1-G0	6	-3.9	19	-8.6	62	11.9	141	1.7	1.01
6.6-G0	4	-2.3	15	-6.3	60	9.1	136	0.5	1.25
11-G0	5	-2.7	17	-4.0	53	7.0	96	0.7	1.10
13-G0	4	-2.5	14	-6.0	54	9.0	102	0.6	1.14
17-G0	3	-2.4	12	-4.6	48	6.6	74	1.4	1.20
22-G0	3	-2.3	11	-2.9	47	5.2	74	1.0	1.17

Table F7: Parameters retrieved by fitting the monomer decays for Py-G0 PGA samples in DMSO to a sum of exponentials equation.

Sample	τ_1 (ns)	A_1	τ_2 (ns)	A_2	τ_3 (ns)	A_3	χ^2
4.1-G0	5	0.2	51	0.3	145	0.5	1.21
6.6-G0	15	0.3	56	0.4	140	0.2	1.07
11-G0	15	0.5	50	0.4	142	0.1	1.10
13-G0	14	0.5	47	0.4	124	0.1	1.08
17-G0	10	0.5	34	0.4	124	0.1	1.11
22-G0	7	0.6	22	0.4	85	0.0	1.21

Table F8: Parameters retrieved by fitting the excimer decays for Py-G0 PGA samples in DMSO to a sum of exponentials equation.

Sample	τ_1 (ns)	A_1	τ_2 (ns)	A_2	τ_3 (ns)	A_3	τ_4 (ns)	A_4	χ^2
4.1-G0	7	-1.4	23	-7.4	65	8.2	124	1.6	1.04
6.6-G0	8	-2.0	22	-8.1	60	10.3	117	0.8	1.25
11-G0	7	-2.2	20	-8.1	53	10.6	95	0.7	1.03
13-G0	8	-2.8	24	-9.4	43	9.0	69	4.2	1.05
17-G0	5	-1.9	16	-8.9	52	11.4	90	0.3	1.14
22-G0	3	-1.6	11	-5.4	49	7.7	87	0.3	1.08

Table F9: Parameters retrieved by fitting the monomer decays for Py-G1 PGA samples in DMF to a sum of exponentials equation.

Sample	τ_1 (ns)	A_1	τ_2 (ns)	A_2	τ_3 (ns)	A_3	χ^2
1.3-G1	15	0.2	72	0.3	202	0.5	1.02
5.9-G1	14	0.4	59	0.4	185	0.3	0.90
7.2-G1	13	0.4	55	0.3	180	0.3	1.08
12-G1	13	0.6	46	0.3	173	0.1	1.22
13-G1	11	0.6	41	0.3	157	0.1	1.13
17-G1	9	0.7	33	0.2	154	0.0	1.27
21-G1	7	0.7	32	0.2	166	0.1	1.25
22-G1	7	0.8	32	0.2	165	0.1	1.24

Table F10: Parameters retrieved by fitting the excimer decays for Py-G1 PGA samples in DMF to a sum of exponentials equation.

Sample	τ_1 (ns)	A_1	τ_2 (ns)	A_2	τ_3 (ns)	A_3	τ_4 (ns)	A_4	χ^2
1.3-G1	9	-1.5	26	-3.7	68	5.3	148	0.9	1.08
5.9-G1	5	-1.6	19	-4.7	62	6.5	122	0.8	1.00
7.2-G1	8	-1.6	23	-2.7	56	4.5	108	0.8	1.00
12-G1	5	-2.0	17	-3.9	54	6.5	97	0.5	1.12
13-G1	4	-2.1	14	-4.6	51	6.6	83	1.1	0.93
17-G1	3	-2.3	11	-3.9	48	6.2	76	1.1	1.00
21-G1	3	-2.4	11	-2.8	44	4.0	69	2.2	1.10
22-G1	5	-2.3	25	-2.8	36	4.4	68	1.7	1.17

Table F11: Parameters retrieved by fitting the monomer decays for Py-G1 PGA samples in DMSO to a sum of exponentials equation.

Sample	τ_1 (ns)	A_1	τ_2 (ns)	A_2	τ_3 (ns)	A_3	χ^2
1.3-G1	8	0.2	61	0.3	158	0.5	1.03
5.9-G1	16	0.3	58	0.5	146	0.3	0.99
7.2-G1	13	0.3	51	0.5	140	0.2	1.06
12-G1	10	0.5	38	0.4	128	0.1	1.13
13-G1	10	0.5	34	0.4	115	0.1	1.21
17-G1	8	0.5	28	0.4	115	0.1	1.26
21-G1	8	0.7	31	0.3	131	0.1	1.21
22-G1	9	0.7	32	0.2	138	0.1	1.25

Table F12: Parameters retrieved by fitting the excimer decays for Py-G1 PGA samples in DMSO to a sum of exponentials equation.

Sample	τ_1 (ns)	A_1	τ_2 (ns)	A_2	τ_3 (ns)	A_3	τ_4 (ns)	A_4	χ^2
1.3-G1	19	-0.6	33	-2.6	59	3.3	118	1.0	1.11
5.9-G1	10	-2.1	30	-9.0	56	10.0	98	2.1	1.00
7.2-G1	7	-1.4	24	-7.2	56	8.2	94	1.4	1.04
12-G1	6	-1.2	18	-3.7	52	5.5	88	0.4	1.22
13-G1	4	-1.7	15	-6.8	51	9.2	92	0.3	1.18
17-G1	5	-1.8	20	-3.4	29	4.0	54	2.1	1.17
21-G1	2	-1.6	11	-4.5	47	6.3	75	0.9	1.17
22-G1	3	-1.8	11	-3.8	46	5.5	68	1.1	1.10

Table F13: Parameters retrieved by fitting the monomer decays for Py-G2 PGA samples in DMF to a sum of exponentials equation.

Sample	τ_1 (ns)	A_1	τ_2 (ns)	A_2	τ_3 (ns)	A_3	χ^2
1.1-G2	15	0.2	79	0.2	201	0.6	1.15
4.3-G2	19	0.3	78	0.4	187	0.3	1.09
6.6-G2	12	0.4	49	0.4	165	0.2	1.17
8.7-G2	12	0.5	49	0.4	171	0.1	1.09
10-G2	11	0.5	44	0.4	166	0.1	1.09
14-G2	8	0.7	29	0.2	149	0.0	1.24
18-G2	6	0.8	26	0.2	140	0.0	1.26

Table F14: Parameters retrieved by fitting the excimer decays for Py-G2 PGA samples in DMF to a sum of exponentials equation.

Sample	τ_1 (ns)	A_1	τ_2 (ns)	A_2	τ_3 (ns)	A_3	τ_4 (ns)	A_4	χ^2
1.1-G2	12	-1.7	26	-2.2	70	4.0	162	0.9	1.03
4.3-G2	8	-2.4	25	-4.1	63	6.4	130	1.0	1.11
6.6-G2	5	-2.2	18	-5.5	59	8.0	114	0.7	1.09
8.7-G2	4	-2.3	17	-5.5	59	8.4	116	0.4	1.06
10-G2	4	-2.0	16	-5.3	57	7.8	105	0.5	1.18
14-G2	4	-2.4	13	-2.4	46	4.5	72	1.2	1.08
18-G2	2	-1.9	8	-2.7	49	5.0	85	0.5	1.04

Table F15: Parameters retrieved by fitting the monomer decays for Py-G2 PGA samples in DMSO to a sum of exponentials equation.

Sample	τ_1 (ns)	A_1	τ_2 (ns)	A_2	τ_3 (ns)	A_3	χ^2
1.1-G2	7	0.1	67	0.3	154	0.6	0.98
4.3-G2	14	0.2	60	0.5	138	0.3	1.09
6.6-G2	15	0.4	51	0.5	133	0.1	1.09
8.7-G2	14	0.4	45	0.4	129	0.1	1.05
10-G2	14	0.5	43	0.4	132	0.1	1.06
14-G2	8	0.6	27	0.3	118	0.0	1.10
18-G2	6	0.7	21	0.3	104	0.0	1.25

Table F16: Parameters retrieved by fitting the excimer decays for Py-G2 PGA samples in DMSO to a sum of exponentials equation.

Sample	τ_1 (ns)	A_1	τ_2 (ns)	A_2	τ_3 (ns)	A_3	τ_4 (ns)	A_4	χ^2
1.1-G2	20	-0.5	28	-3.3	78	3.3	136	1.5	0.97
4.3-G2	33	-6.4	12	-2.2	103	2.0	57	7.7	1.04
6.6-G2	8	-2.1	22	-6.8	58	9.4	111	0.5	1.08
8.7-G2	8	-2.2	24	-6.2	49	7.7	80	1.7	1.03
10-G2	8	-2.1	21	-4.6	51	7.3	90	0.5	1.19
14-G2	4	-1.7	13	-4.9	49	7.3	86	0.3	1.16
18-G2	6	-2.2	21	-1.7	36	3.5	61	1.3	1.12

Table F17: Parameters retrieved by fitting the monomer decays for Py-G3 PGA samples in DMF to a sum of exponentials equation.

Sample	τ_1 (ns)	A_1	τ_2 (ns)	A_2	τ_3 (ns)	A_3	χ^2
2.5-G3	15	0.2	74	0.3	191	0.5	1.11
4.0-G3	17	0.2	73	0.4	181	0.4	1.00
5.4-G3	17	0.4	66	0.4	180	0.2	1.13
6.0-G3	12	0.4	54	0.5	169	0.2	1.12
6.6-G3	16	0.4	58	0.5	168	0.2	1.07
8.1-G3	13	0.5	49	0.4	169	0.1	1.06
9.4-G3	11	0.5	41	0.4	166	0.1	1.17
11-G3	9	0.6	34	0.3	148	0.0	1.08
11-G3	11	0.5	43	0.4	172	0.1	1.08
12-G3	9	0.7	34	0.2	158	0.1	1.29
13-G3	8	0.8	31	0.2	172	0.1	1.04

Table F18: Parameters retrieved by fitting the excimer decays for Py-G3 PGA samples in DMF to a sum of exponentials equation.

Sample	τ_1 (ns)	A_1	τ_2 (ns)	A_2	τ_3 (ns)	A_3	τ_4 (ns)	A_4	χ^2
2.5-G3	12	-4.5	44	-15.8	53	19.5	136	1.8	0.96
4.0-G3	11	-3.7	42	-14.9	52	17.7	131	1.9	1.02
5.4-G3	5	-2.6	19	-7.5	62	9.9	117	1.2	1.14
6.0-G3	4	-2.1	19	-7.3	65	9.4	118	1.0	1.07
6.6-G3	4	-2.3	19	-7.1	64	9.6	119	0.8	1.03
8.1-G3	4	-2.4	17	-6.9	58	9.8	110	0.6	1.03
9.4-G3	4	-2.3	16	-5.6	56	8.5	104	0.4	0.91
11-G3	5	-2.7	19	-4.0	41	5.0	68	2.6	1.19
11-G3	4	-2.4	16	-6.8	53	8.9	88	1.3	1.08
12-G3	2	-1.8	10	-4.3	50	6.4	83	0.7	1.11
13-G3	5	-2.6	20	-3.1	36	4.5	66	2.3	1.12

Table F19: Parameters retrieved by fitting the monomer decays for Py-G3 PGA samples in DMSO to a sum of exponentials equation.

Sample	τ_1 (ns)	A_1	τ_2 (ns)	A_2	τ_3 (ns)	A_3	χ^2
2.5-G3	15	0.1	72	0.4	150	0.4	1.19
4.0-G3	15	0.2	66	0.5	144	0.4	1.25
5.4-G3	16	0.3	56	0.5	135	0.2	1.13
6.0-G3	16	0.3	54	0.6	138	0.2	1.13
6.6-G3	15	0.3	49	0.5	132	0.1	1.02
8.1-G3	15	0.4	46	0.5	134	0.1	1.05
9.4-G3	11	0.4	38	0.5	131	0.1	1.19
11-G3	9	0.6	30	0.4	121	0.0	1.07
11-G3	14	0.5	45	0.4	140	0.1	1.11
12-G3	9	0.6	30	0.3	130	0.1	1.22
13-G3	8	0.7	28	0.3	137	0.0	1.30

Table F20: Parameters retrieved by fitting the excimer decays for Py-G3 PGA samples in DMSO to a sum of exponentials equation.

Sample	τ_1 (ns)	A_1	τ_2 (ns)	A_2	τ_3 (ns)	A_3	τ_4 (ns)	A_4	χ^2
2.5-G3	16	-3.4	46	-21.7	55	23.7	117	2.5	1.16
4.0-G3	16	-3.2	43	-15.0	55	16.3	106	2.8	1.08
5.4-G3	7	-1.7	25	-11.1	61	12.0	99	1.7	1.10
6.0-G3	9	-2.6	27	-11.7	59	14.0	99	1.3	1.18
6.6-G3	6	-2.0	23	-11.8	55	12.7	86	2.1	1.06
8.1-G3	7	-2.5	23	-11.1	49	11.8	76	2.8	1.00
9.4-G3	7	-2.3	20	-7.4	53	10.2	89	0.5	0.97
11-G3	5	-1.7	14	-5.3	48	7.8	83	0.2	0.97
11-G3	5	-1.6	19	-9.1	54	11.4	106	0.3	1.03
12-G3	4	-1.8	14	-4.6	46	6.1	65	1.3	1.17
13-G3	3	-1.1	11	-3.6	47	5.2	80	0.5	1.05